Alma Mater Studiorum · University of Bologna

School of Science
Department of Physics and Astronomy
Master Degree in Physics

The XENONnT Neutron Veto: commissioning of the Gadolinium-water purification system

Supervisor:
Dr. Marco Selvi

Co-supervisor:
Dr. Andrea Mancuso
Prof. Gabriella Sartorelli

Submitted by:
Federico Casadei

Academic Year 2021/2022

Abstract

Many observational evidences for the existence of Dark Matter have been discovered over the last century. Several techniques are employed to directly search for a Dark Matter signal; among them, the XENONnT experiment features a Xenon double-phase TPC with a target mass of 5.9 tons and an active Neutron Veto (NV) system. The NV is designed as a Gadolinium-doped water Cherenkov detector, used to capture and tag neutrons and reduce the background. The presence of Gadolinium results in a lower veto dead time and a higher neutron tagging efficiency. In this thesis, developments on two important aspects of the NV are presented. On one hand, the Reflectivity Monitor is a tool to measure the photon absorption time in the NV and monitor its optical properties over time. Data analysis has been implemented and supported by Monte Carlo simulations; the photon absorption time has been measured to be (57 ± 1) ns, constant over time. On the other hand, a dedicated purification plant, the Gadolinium-water purification system (GdWPS), is necessary to insert Gd in the Neutron Veto and at the same time purify water from other impurities; its working principle consists in separating Gd-rich from Gd-depleted solutions and purifying this latter minimizing Gadolinium losses. Important steps in its commissioning phase have been taken, operating with pure water. During this phase, the Reflectivity Monitor showed a slight decrease in photon absorption time, not directly ascribable to GdWPS operation. After that, 15 kg of Gd salt have been inserted in the GdWPS as a test: the insertion system worked properly. An efficient method to estimate Gd concentration has been found and validated by mass-spectrometry measurements and the separation efficiency has been measured as $99.6\ \% - 99.85\ \%$. A tolerable Gd loss of 600 g/day has been found. Transparency measurements showed that the GdWPS is able to keep photon absorption lengths of the order of tens of meters both in pure water and Gd-water samples.

Contents

Introduction

The first observations claiming the presence of dark bodies in the Universe date back to the 30's, when discrepancies between the luminous and gravitational mass of some stellar systems led to the hypothesis of the existence of a new type of matter, elusive and mysterious: the *Dark Matter*. Since then, a huge phenomenology supporting this hypothesis grew up until reaching, today, diffuse confidence and popularity among the scientific community. The most accepted model, supported by observations of different nature, states that Dark Matter accounts for 27% of the total mass-energy content of the Universe. Another 68% is constituted by Dark Energy while ordinary matter, the only component described by the Standard Model of particle physics, only brings a 5% contribution. Despite the numerous attempts, no direct Dark Matter signal has been found so far by any experiment. In Chapter 1 most of the experimental evidence for the existence of Dark Matter are reported, in addition to theoretical models describing possible candidates which could partially or entirely explain the observations. In this regard, Weakly Interacting Massive Particles (WIMPs) are particularly promising since they fit in a rather natural way in the phenomenology. The most common detection techniques in the pursuit of a Dark Matter signal are also described, with particular attention to direct detection searches.

XENONnT, the last upgrade of the XENON Dark Matter project, is one of the most promising detectors for this purpose and the topic of Chapter 2. The XENON project started in 2005 at the INFN Laboratori Nazionali del Gran Sasso (LNGS) in Italy, and has provided world-leading results in the direct search of WIMPs. XENONnT has been built in 2020 and features a double-phase Xenon Time Projection Chamber (TPC) surrounded by two active veto systems. Its most important features are described and particular importance is given to the *Neutron Veto*, a novel Gadolinium-doped water Cherenkov detector that strongly reduces the dangerous neutron background of the experiment. The important role of Gadolinium doping is as well reported, quantifying the improvements that it brings: a lower veto-induced dead time and at the same time a significantly stronger background rejection power.

For the correct operation of the XENONnT Neutron Veto, water has to maintain a high-quality level; a dedicated tool to check over time the performances in terms of optical properties has been designed: the *Reflectivity Monitor*, a laser-based calibration

system which measures the survival time of photons in the Neutron Veto. In Chapter 3, details are presented about the hardware setup, data acquisition, and data analysis, before reporting the first results. Everything is integrated with Monte Carlo simulations, better characterizing the contributions of water transparency and wall reflectivity to the optical properties, and validated with an analysis of Neutron Veto data. This latter is important to check that the results provided by the Reflectivity Monitor are valid not only within the calibration but with real Neutron Veto events as well.

In Chapter 4 is presented the *Gadolinium-water purification system (GdWPS)*, a specifically designed purification plant aiming at inserting Gadolinium in the Neutron Veto, maintaining a stable concentration and at the same time avoiding degradation of the optical performances. The technique adopted in the GdWPS to satisfy these requirements is based on the separation via nano-filtration in Gd-rich and Gd-depleted water: this latter can be de-ionized without significant Gadolinium loss. After a detailed illustration of the different components used for the purification and for the Gadolinium insertion and of the sensors placed across the plant, its first phase of operation with pure water is described. During this period, two instruments have been used to supervise the performances of the GdWPS. On one hand, with the Reflectivity Monitor we have checked the effects of the purification directly in the Neutron Veto; on the other, transparency measurements have been performed with a specific instrumentation allowing to quantify the purity of different water samples. The results obtained with these two devices are also reported in Chapter 4.

In Chapter 5, finally, the outcome of the first test insertions of Gadolinium in the GdWPS is described. After preliminary measurements on Gd-water samples, multiple insertions of Gd-salt have been made eventually reaching the nominal design concentration of 0.5% in mass. The results of different methods for estimating the Gadolinium concentration, including mass spectrometry, are shown; the ability of purifying water without affecting the Gadolinium concentration is quantified through the efficiency in separating the Gd-rich and Gd-depleted solutions. Transparency measurement results have been carried out also on Gd-water samples, prepared at the LNGS Chemistry Laboratory and collected directly from the plant: the results are reported in this last Chapter.

Chapter 1

Dark Matter

Among the matter-energy content of the Universe, the *ordinary matter*, described by the Standard Model of particle physics, only accounts for about 5% of the total. The remaining part is divided into *Dark Energy* (about 68%) and *Dark Matter* (about 27%) [1]. We are aware of the latter thanks to experimental evidence of different natures but all of which being related to gravitational interaction. Although several attempts have been made over the years, no Dark Matter signal has been detected yet.

1.1 Cosmology and the Dark Universe

Cosmology, one of the most ancient fields of science ever investigated, aims to explain the origin of the Universe and its evolution.

The most accepted picture nowadays is based on the *Big bang theory* and on the *inflation* model; they rely on Einstein's theory of General Relativity. The starting points are the *field equations* that read, in their original form:

$$R_{\mu\nu} - \frac{1}{2}Rg_{\mu\nu} := G_{\mu\nu} = -\frac{8\pi G_N}{c^4}T_{\mu\nu} \tag{1.1}$$

where:

- $g_{\mu\nu}$ is the metric tensor (diag(1,-1,-1,-1));
- $R_{\mu\nu}$ the Ricci tensor;
- $T_{\mu\nu}$ is the energy-momentum tensor, which encapsulates the mass-energy content of the Universe;
- R is given by the contraction $R^{\mu\nu}g_{\mu\nu}$;
- $G_{\mu\nu}$ is called *Einstein tensor* and represents the geometry of the Universe.

When Einstein first proposed his theories, the Universe expansion was not known and, in order to allow for a stationary solution of the field equations, an additional term was added. In fact, due to the attractive nature of the gravitational force, the Universe would be otherwise destined to collapse. A new source of energy, with the relevant feature of having negative pressure [2, 3], was introduced. In this way (1.1) becomes

$$R_{\mu\nu} - \frac{1}{2}Rg_{\mu\nu} = -\frac{8\pi G_N}{c^4}T_{\mu\nu} + \Lambda g_{\mu\nu} \tag{1.2}$$

with Λ known as *cosmological constant*. This term represents a source of energy (also known as 'vacuum energy') independent of the presence of matter but rather associated to space-time itself. After the 'ad-hoc' inclusion of this term in the field equations, the Universe turned out to be not stationary, but in expansion. However, different observations confirmed that the expansion is not slowed down by gravity; instead, it is in constant acceleration (as found by different measurements, most of them using type Ia Supernovae [4]). This leads us to thinking that the cosmological constant is a real, positive term contributing to the Universe energy: what today we call Dark Energy.

In order to find solutions to the (1.1) one should add other ingredients. First of all, the spatial *isotropy* and *homogeneity* are assumed; experimental evidence prove indeed that the non-uniformities vanish at large distances, in particular the ones involving the Cosmic Microwave Background (CMB) [5]. The solutions depend also on the geometry of space-time, which is not necessarily flat. The elementary invariant space-time distance is given, in general, by

$$ds^2 = c^2dt^2 - a(t)^2\left[\frac{dr^2}{1-kr^2} + r^2\left(d\theta^2 + sin^2\theta\, d\phi^2\right)\right] \tag{1.3}$$

in a spherical coordinates system (r, θ, ϕ) where the origin is arbitrary, due to spatial homogeneity. $a(t)$ is the *scale factor* accounting for the Universe stretch. The geometry depends on the factor k: it can take the values 0, -1, $+1$ for a flat (Euclidian), negatively curved (open), positively curved (closed) Universe, respectively[1].

With these assumptions, the Einstein field equations lead to the *Friedmann equation*:

$$\left(\frac{\dot{a}}{a}\right)^2 + \frac{k}{a^2} = \frac{8\pi G_N}{3}\rho_{tot}\,. \tag{1.4}$$

ρ_{tot} stands for the total average energy density of the Universe. The ratio $\dot{a(t)}/a(t)$ is defined as *Hubble parameter* $H(t)$; its value at the present time is known as *Hubble constant* H_0 and has been measured to be [6]:

$$H_0 = 70.50 \pm 2.37\,(\text{stat.}) \pm 3.38\,(\text{sys.})\ \text{km}\,\text{s}^{-1}\,\text{Mpc}^{-1} \tag{1.5}$$

[1]Every other value of k can be absorbed in a, and it does not have any effect.

where 1 pc ('parsec') $\simeq 3.26$ light-years. In these terms, the Friedmann equation can be written as

$$\frac{8\pi G_N}{3H^2}\rho_{tot} - \frac{k}{a^2H^2} = 1\,; \tag{1.6}$$

The left-hand side includes one term proportional to ρ_{tot}, where both matter and energy can contribute, and one term dependent on the space curvature through the parameter k. It is common to define the following terms:

$$\begin{aligned} \Omega_m &= \frac{8\pi G_N}{3H^2}\rho_{matter} && \text{matter contribution} \\ \Omega_\Lambda &= \frac{8\pi G_N}{3H^2}\rho_\Lambda && \text{Dark Energy contribution} \\ \Omega_k &= -\frac{k}{a^2H^2} && \text{curvature contribution} \end{aligned} \tag{1.7}$$

which finally lead to

$$\Omega_m + \Omega_\Lambda + \Omega_k = 1\,. \tag{1.8}$$

This equation represents the equilibrium among the different contributions which play a role in the evolution of the Universe. Matter, on one hand, provides a term proportional to its density, ρ_{matter}. The same does, on the other, the vacuum energy which embodies the corresponding of cosmological constant through its density ρ_Λ. The third term can give both a negative or positive contribution depending on the space curvature, and it can be null as well.

Indeed, from recent observations [7, 1], the Universe seems to be endowed with a flat geometry. This means that Ω_k should be set to zero. Matter and dark energy, together, provide an energy density which must equal $3H^2/8\pi G_N$, a quantity usually called *critical density*.

Strong constraints have been set on these cosmological parameters, as from the DES collaboration [8] and Planck collaboration [1], claiming that the vacuum energy accounts for $\simeq 68\%$ of the critical density ($\Omega_\Lambda = 0.6847 \pm 0.0073$, $\Omega_m = 0.315 \pm 0.007$). This result comes from the merger of observations of different natures, as shown in Figure 1.1.

From what has been said, Dark Energy seems to be the predominant contribution to the evolution of the Universe. Furthermore, the ordinary matter that we know and are able to describe with the Standard Model seems not to be enough to account for the rest of 32%, as will be shown in the next Section. Around 27% of the total matter-energy content is due to an unknown substance that escaped every detection attempt by now: what we call Dark Matter.

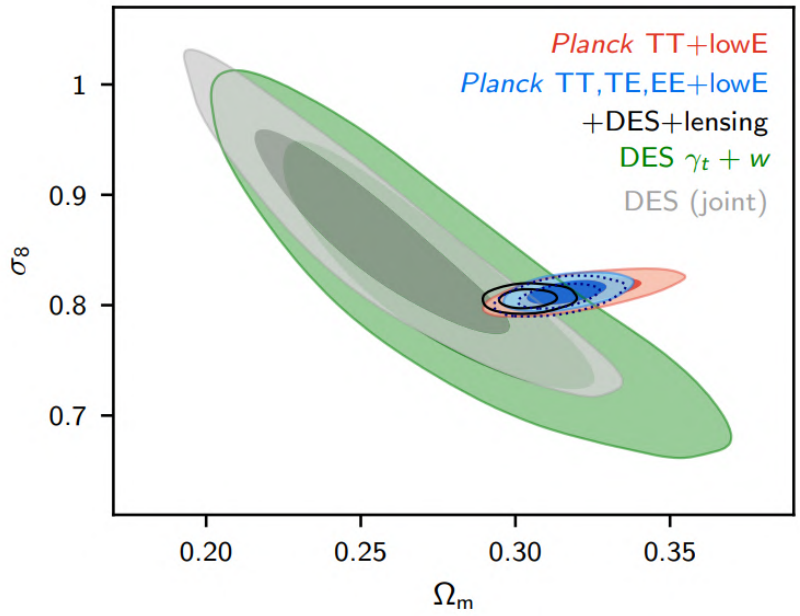

Figure 1.1: Constraints on Ω_m. Merged results (black) of Planck data (red and blue) and DES data (green and grey), with 1σ and 2σ contours. Image from [1].

1.2 Dark Matter evidence

The experimental evidence for the existence of Dark Matter is of different nature and applies on different scales in the Universe. *Galaxies* represent gravitational-bound systems of stars and interstellar medium with typical dimensions of tens of kpc. On a larger scale, galaxies organize in *galaxy clusters* with much larger dimensions, of the order of Mpc. In both cases and even at larger scales, Dark Matter is thought to give a strong contribution to the total mass content. All the observations are based on the evidence of more mass (required for gravitational equilibrium) than the one which emits light.

All these observations suggest the existence of a kind of matter which does not emit light of any wavelength and barely interacts with ordinary matter, or not at all, except for the gravitational force [9].

1.2.1 Galactic scale

Rotation curves in spiral galaxies

One of the observations in support of the existence of Dark Matter is related to the rotation speed of stars and gas in *spiral galaxies* (see Figure 1.2).

Spiral galaxies constitute about two-thirds of the total number of known galaxies.

Figure 1.2: Spiral galaxy NGC 1376, placed at 200 million light-years from the Earth. Picture from the Hubble Space Telescope [10].

They are made up of a flat *disk* with a central *bulge* where most of the mass is concentrated; around the bulge, the stars form spiral arms. They are in fast rotation around their center of mass, which is usually coincident with a Supermassive Black Hole (SMBH). Their rotation speed is often measured through the 21 cm line emission of the atomic hydrogen gas present in the whole galactic region and beyond. It comes from the hyperfine splitting of its ground state and provides a useful monoenergetic peak [11]; the speed of the gas is then obtained thanks to the Doppler effect, looking at the redshift of the emission.

Considering an object placed at a distance r from the center of the galaxy, in order to ensure equilibrium its rotation speed must assume a precise value, dependent on the centripetal force acting on it. Since this force has a gravitational nature, it depends in turn on the amount of matter present inside a sphere of radius r. Spiral galaxies are almost flat; however, the great majority of their mass is concentrated in the bulge, which can be considered spherical [12]. We can then assume

$$\begin{aligned} M(r) &\propto r^3 \qquad & r < r_b \\ M(r) &= const \qquad & r \geqslant r_b \end{aligned} \tag{1.9}$$

where r_b is the bulge radius and we have assumed a uniform bulge mass distribution.

Thus, by equating the centripetal force to the gravitational attraction we get

$$\begin{aligned} \frac{v(r)^2}{r} &= \frac{G_N M(r)}{r^2} \propto r \qquad r < r_b \\ \frac{v(r)^2}{r} &= \frac{G_N M(r)}{r^2} \propto \frac{1}{r^2} \quad r \geqslant r_b \end{aligned} \tag{1.10}$$

that means

$$\begin{aligned} v(r) &\propto r \qquad\quad r < r_b \\ v(r) &\propto 1/\sqrt{r} \quad r \geqslant r_b \,. \end{aligned} \tag{1.11}$$

We expect the rotation speed to increase linearly until the bulge edge is reached, then to decrease with a square-root law. However, observations showed that for most of the studied galaxies the rotation speed is almost constant even at large distances from the galactic center, far beyond the edge of the galactic disk[2]. This discrepancy can be solved if one assumes the presence of a Dark Matter *halo* in addition to the visible matter, in gravitational equilibrium with this latter.

One of the first galaxies where this observation was made is NGC 6503. Its rotation curve is reported in Figure 1.3.

The Dark Matter halo is usually described with a radial mass density distribution given by the *Navarro-Frenk-White (NFW) profile* [14]:

$$\rho(r) = \frac{\rho_h}{(r/r_h)\left[1 + r/r_h\right]^2} \tag{1.12}$$

with ρ_h and r_h representing respectively the characteristic density and radius of the halo.

Velocity dispersion in elliptical galaxies

Elliptical galaxies have several differences compared to spiral ones. They are characterized by a low rate of star creation, contrary to spiral galaxies where this process is frequent. In addition, their shape is not flat but ellipsoidal or spherical. Regarding their kinematics, the rotation of the stars around the central SMBH is disorganized; they can be viewed as a thermalized stellar gas as their stars move in random directions. This fact, in addition to the lack of interstellar gas, makes the observational technique used for spiral galaxies hard to apply. In order to obtain the average speed of the stars at a given distance from the center of the galaxy, the *velocity dispersion* σ is employed.

In fact, by studying the wavelength spectrum of a galaxy, it is possible to compute its distance from Earth using the redshift, assuming to know the Hubble constant. The velocity spread of the stars with respect to the galactic stream of reference gives instead an enlargement of the redshift. If one is able to measure this enlargement at different

[2]Here the rotation speed is still measurable due to the presence of gas.

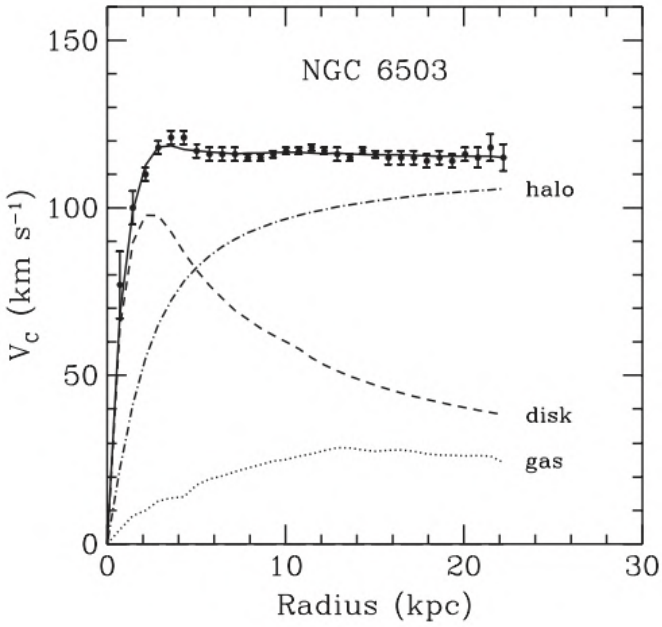

Figure 1.3: Rotation curve of NGC 6503 [13]. The points, representing data, show a flat behaviour after the first rise. The dash-dotted line is the contribution of the hypothetical Dark Matter halo, able to reproduce such a rotation curve.

positions along the galactic radius, it is possible to apply the same method used for spiral galaxies.

In this way, several observations as [15] found discrepancies between observed velocity profiles and predictions, suggesting the presence of a Dark Matter halo also in elliptical galaxies (see Figure 1.4).

Other works as [16] made accurate studies to model the shape of the stellar velocity distribution. Such studies led to the same conclusions, highlighting the presence of a Dark Matter component in elliptical galaxies.

1.2.2 Galaxy clusters scale

Gravitational equilibrium in galaxy clusters

Galaxy clusters are gravitationally-bound systems of galaxies; from a dynamical point of view they are analogous to elliptical galaxies, but on a larger scale.

What is usually used in this case is the *virial theorem*. It relates the average potential energy to the average kinetic energy of a stationary system. In its general form, it reads

$$\frac{1}{2}\frac{d^2 I}{dt^2} = 2\langle K\rangle + \langle U\rangle \tag{1.13}$$

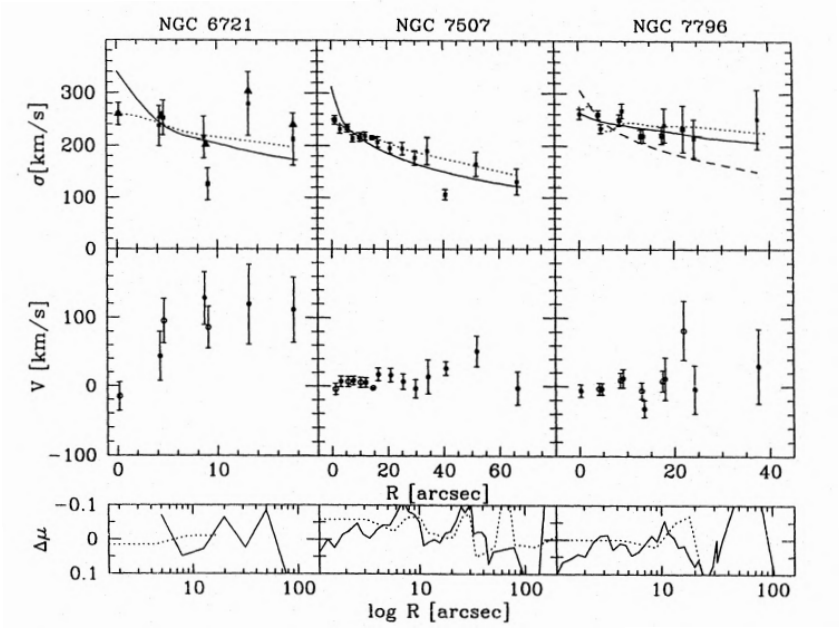

Figure 1.4: Velocity dispersion curves for three galaxies exposed in [15]. Top panels: velocity dispersion as a function of the radius; middle panels: radial velocity as a function of the radius; bottom panels: residuals of the fit. For NGC 6721 and NGC 7507 the solid lines represent the best-fit curve, assuming no Dark Matter presence. For NGC 7796 the solid line assumes instead the presence of Dark Matter, while the no-Dark Matter model (dashed line) shows a discrepancy. The presence of a Dark Matter halo looks necessary for NGC 7796.

where I is the moment of inertia in the center of mass frame and $\langle K \rangle$ and $\langle U \rangle$ are the average kinetic energy and potential energy, respectively. For a stationary galaxy, the left-hand term is null and one can write

$$2\langle K \rangle = -\langle U \rangle \,. \tag{1.14}$$

The average kinetic energy of a cluster can be simply written as:

$$\langle K \rangle = \sum_i \frac{M_i \langle v \rangle^2}{2} = \frac{1}{2} M \langle v \rangle^2 \tag{1.15}$$

where $\langle v \rangle$ is the average speed of the galaxies which the cluster consists of and M is its *total* mass. $\langle v \rangle^2$ is related to the velocity dispersion σ introduced in Section 1.2.1; in a three-dimensional space, the squared mean velocity is three times σ^2, being this latter only measured along the line of sight.

$\langle U \rangle$ needs instead a sum over each galaxy; assuming a uniform spherical distribution of galaxies it can be written as

$$\langle U \rangle = -\frac{3}{5}\frac{G_N M^2}{R} \tag{1.16}$$

where R denotes the radius of the considered cluster.

In this way, imposing (1.14), one gets an estimate of the cluster mass:

$$M = \frac{5R\sigma^2}{G_N}\,. \tag{1.17}$$

One of the first studies on this subject was made by F. Zwicky on the *Coma Cluster* [17]. In his work, Zwicky conservatively took a lower bound value for the mass of the Coma Cluster to be

$$M > \frac{3}{5}\frac{R\sigma^2}{G_N} \tag{1.18}$$

to account for the non-uniformities in the galaxy's distribution. The measured mean velocity was $\simeq 700\,\mathrm{km/s}$ and the radius $\simeq 2 \cdot 10^6$ light-years. Therefore the estimate for the total mass of the Coma Cluster was around $10^{47}\,\mathrm{g}$, corresponding to an average mass per galaxy[3] of $4.5 \cdot 10^{10}\,\mathrm{M}_\odot$[4]. Since the average luminosity of a galaxy is $\sim 7.5 \cdot 10^7$ times the solar one, we get a mass-to-light ratio of ~ 500.

Nevertheless, this excess of mass turned out to be overestimated. More recent and accurate measurements of all the involved quantities reduce the matter excess to ~ 10. Therefore, even if in a much smaller quantity, a mass excess is still evident in the Coma Cluster.

Other works use a different approach which leads to the same conclusion. A relevant fraction of the mass of a cluster is in the form of hot gas present between stars and galaxies, usually called Intracluster Medium (ICM). Assuming it to be approximately an ideal gas in hydrostatic equilibrium and in spherical geometry, its stability is governed by [18]:

$$\frac{dp_g}{dr} = \rho_g \frac{G_N M\,(r)}{r^2}\,, \tag{1.19}$$

where p_g and ρ_g are the gas pressure and density and $M\,(r)$ is the mass contained within a radius r. Using the state equation for ideal gases of temperature T_g and molecular weight μ[5]

$$p_g = \frac{\rho_g k_B T_g}{\mu}\,, \tag{1.20}$$

[3] Zwicky assumed 1000 galaxies in the cluster.

[4] $M_\odot = 1$ solar mass.

[5] It is usually assumed to be 0.6 times the proton mass.

it is possible to infer the mass content:

$$M(r) = -\frac{k_B T_g(r)}{G_N \mu} r \left[\frac{d \log \rho_g(r)}{d \log r} + \frac{d \log T_g(r)}{d \log r} \right] . \tag{1.21}$$

What is needed are the temperature and density profiles $T_g(r)$ and $\rho_g(r)$. The temperature is of the order of keV and can be measured by X-ray telescopes as ROSAT [19] and Chandra [20, 21]. Such observations provide several properties of the gas and the density profile is detectable with good accuracy as well [22]. With this method, Dark Matter halos have been detected in the great majority of galaxy clusters, with a mass distribution often in agreement with the NFW model.

Gravitational lensing

Another method that can be used to infer the mass of an astronomical object (and thus its Dark Matter content) is the *gravitational lensing* [23]. This effect is based on the fact, exposed in the General Relativity and proved by several observations, that light can be deflected in a measurable way if it passes close to a considerable amount of matter. This is due to the fact that matter distorts space-time and so the geodesic lines of any body (including radiation) can deviate from being a straight line.

According to General Relativity, the light emitted by some source that passes at a distance r from the line of sight of an object of mass M is deflected by an angle

$$\alpha = \frac{4 G_N M}{c^2 r} , \tag{1.22}$$

which corrects by a factor 2 the formula obtained by Newtonian gravitation theory. Applying this equation to the Sun (considering an object whose line of sight passes very close to it, so that $r = \mathrm{R}_\odot$) one gets

$$\alpha = \frac{4 G_N M_\odot}{c^2 R_\odot} \sim 1.74 \text{ arcsec} . \tag{1.23}$$

In 1919, during a solar eclipse, observing the deflection of the light produced by the Hyades Cluster which was passing behind the Sun this prediction was found to be in agreement with the observed deflection angle. It led to one of the first and most famous confirmations of Einstein's theory [24].

In modern astrophysics, gravitational lensing has been found to be a powerful tool to investigate the mass distribution of objects such as galaxies and clusters. In this way, it plays also a role in the study of Dark Matter halos in galaxies and clusters, as in [25]. Many studies employing gravitational lensing found indeed Dark Matter evidence [26].

Two regimes are usually distinguished. On one hand, *strong lensing* refers to the case of a relevant distortion in the shape of an object, providing the doubling of the image

or structures called Einstein rings; in this case, the light distortion can be studied in a direct way. On the other, *weak lensing* is present when the deflections cannot be measured individually but rather with statistical methods. A third case, called *microlensing* [27], is when the strong lensing distortion is not intense enough to resolve the two images. In this situation, if the motion of the light source is not stationary on a human scale (days, months or at most years), the mass reconstruction can be carried out by looking at the time variation of the luminosity of the source.

Bullet Cluster

Bullet Cluster is how the interacting cluster 1E0657-558 is commonly called. It is the remnant of the collision of two clusters which represents another evidence for the existence of Dark Matter [28] (see Figure 1.5).

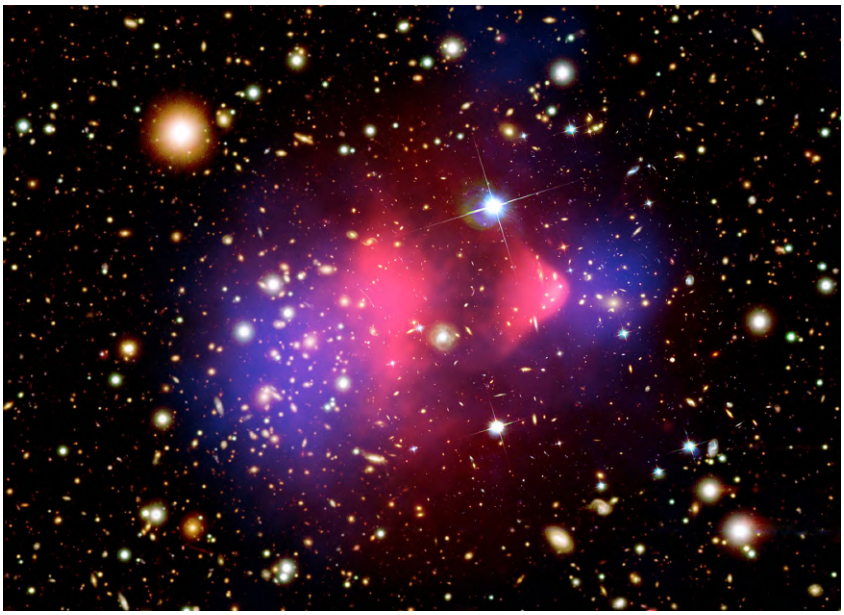

Figure 1.5: Picture of the Bullet Cluster [29]. In blue, the mass distribution coming from the weak lensing analysis. In pink, the X-ray emission from the hot gas of the two clusters. The displacement caused by the gas stripping is evident.

When two clusters collide[6], the stars as well as Dark Matter particles are expected to be basically collisionless. On the contrary, the hot gas present between the galaxies of one cluster feels the pressure of the gas present in the other cluster. While galaxies keep essentially their initial path, the gas is stripped away and displaced. In [28] the gas position is measured by observing its X-ray emission with the Chandra telescope,

[6]Or, better, the smaller one passes through the bigger one.

deriving the center of mass of the gaseous component. In addition, a weak lensing method is used to find the center of mass of the whole system. A clear displacement is found between the two, leaving the total center of mass almost unaffected by the collision. This demonstrates that the hot gas constitutes only a small fraction of the total mass. A Dark Matter halo in addition to the visible galaxies is thus necessary.

The fact that the Dark Matter halo is essentially collisionless comes from the fact that its interaction cross section is thought to be very small. Further investigations have been conducted in other works such as [30], which applies both the X-ray and weak lensing data to assign an upper limit to the Dark Matter interaction cross-section.

The approach with X-ray emission and gravitational lensing merged together is also able to put constraints and potentially rule out the MOND (modified Newtonian dynamics) paradigm [28]. This theory fundamentally tries to explain the observational discrepancies exposed until now through the modification of the Newtonian dynamics, only appreciable at large distances [31].

1.2.3 Cosmological scale

The observations exposed so far highlight the presence of Dark Matter at different scales, from galaxies to galaxy clusters. In order to derive the total amount in the Universe, however, observations on even bigger scales are needed. In this regard, the information brought by the CMB is really powerful.

It is known that the Universe is permeated by microwave radiation, generated in the very first moments of its life, right after the decoupling of radiation from matter. It is now thermalized at 2.726 K, as known from a precise black body fit on its spectrum. What can be used to derive constraints on the cosmological model are the temperature anisotropies, which are of the order of 10^{-5} [9]. They can be expanded in multipoles, through the spherical harmonics $Y_{lm}(\theta, \phi)$ [32]:

$$\frac{\delta T}{T}(\theta, \phi) = \sum_{l=2}^{l=+\infty} \sum_{m=-l}^{m=+l} a_{lm} Y_{lm}(\theta, \phi) \ , \tag{1.24}$$

where T denotes the temperature. Thus, the temperature fluctuations can be quantified by the variance of the amplitudes a_{lm}, which are usually assumed to be gaussian:

$$c_l := \langle |a_{lm}|^2 \rangle = \frac{1}{2l+1} \sum_{m=-l}^{m=+l} |a_{lm}|^2 \ . \tag{1.25}$$

Temperature anisotropies are related to density anisotropies at the decoupling time. The spectrum of c_l is usually used to infer estimates for the cosmological constants Ω_Λ and Ω_m and, among this latter, the contributions of baryons and Dark Matter.

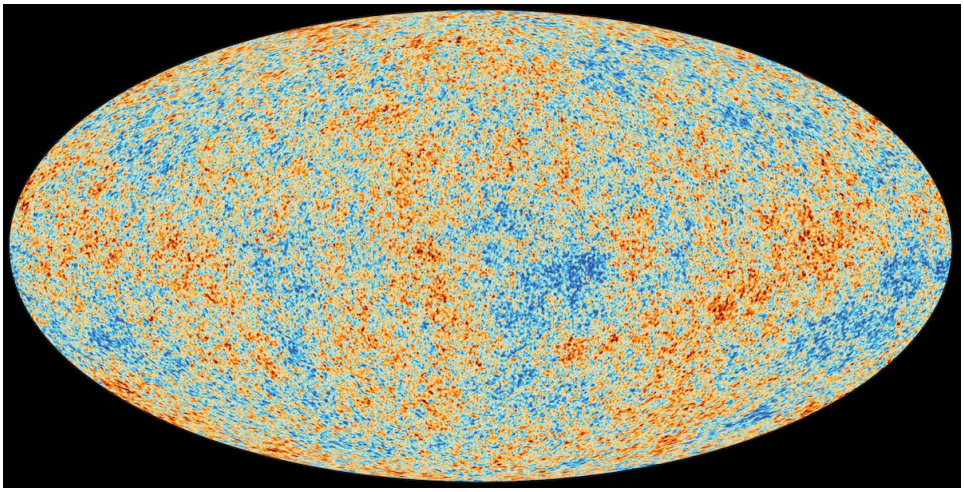

Figure 1.6: Planck data of the CMB, 2018 [34]. Different colours stand for different temperatures, highlighting the anisotropies.

The latest and most precise measurements of the CMB is represented by the Planck mission [33] (Figure 1.6).

With the Planck data it is possible to derive information on the cosmological parameters. They are usually expressed in terms of the Hubble parameter using $h := H_0/100\,\mathrm{km\ s^{-1}\,Mpc^{-1}}$. In [1] a spectral temperature analysis has been carried out, as shown in Figure 1.7.

First of all, Planck data are able to put constraints on the geometry of the Universe, claiming its flatness:

$$\Omega_k = 0.0007 \pm 0.0019\,. \tag{1.26}$$

Among the matter density Ω_m, which is measured to be $\Omega_m h^2 = 0.1430 \pm 0.0011$, the contributions are:

$$\begin{aligned} \Omega_b h^2 &= 0.02237 \pm 0.00015 \qquad \text{baryons} \\ \Omega_{DM} h^2 &= 0.1200 \pm 0.0012 \qquad \text{Dark Matter} \end{aligned} \tag{1.27}$$

which represent the best estimates of the Dark Matter contribution on cosmological scales up to now.

1.3 Dark Matter candidates

Over the years, a big number of models have been constructed, trying to reproduce the observed abundance and respect all the constraints. Some of them rely on *baryonic* candidates, such as white dwarfs, neutron stars, black holes or even lower-mass objects

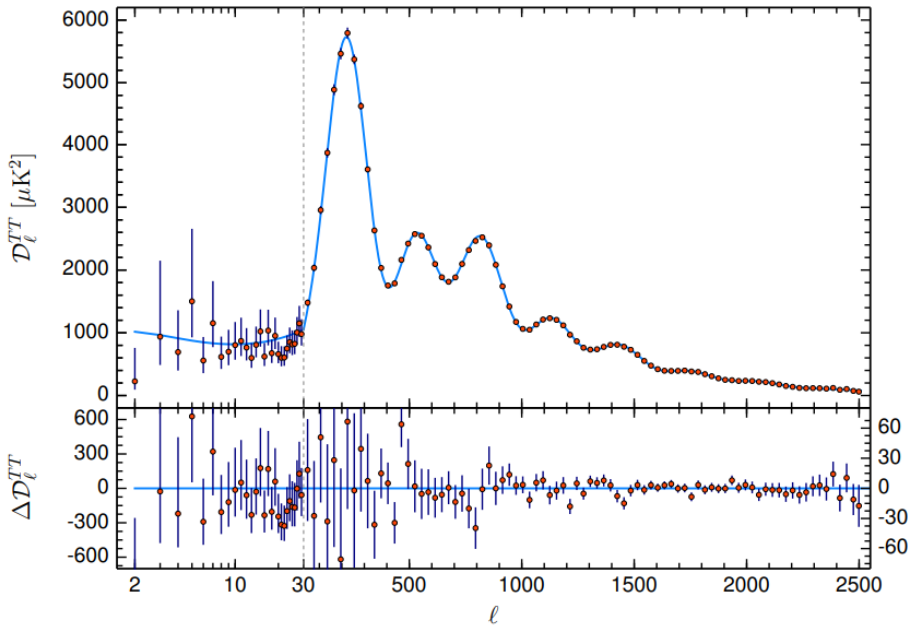

Figure 1.7: Temperature power spectrum of the Planck data analysis [1]. On the x axis, the multipole l; on the y axis, the temperature variance. From this spectrum, it is possible to infer important information on the cosmological parameters.

[35]. They could in some cases escape the astronomical observations; however, they are ruled out by robust theories such as *Big Bang Nucleosynthesis* [36].

Instead, on the *non-baryonic* side, plenty of models have been developed which require physics beyond the Standard Model. These particle candidates can be distinguished by their predicted mass and interaction cross-section, which are the main parameters in the models and in the consequent searches. As in Figure 1.8, they are sometimes represented in a mass-cross section space; the different theories are really spread: their hypothetical masses extend from 10^{-5} eV to 10^{15} GeV.

A good candidate to constitute Dark Matter in the Universe must satisfy some conditions:

- it must be *massive* enough to explain the observed lack of mass and the *relic abundances* (1.27);
- it must not interact electromagnetically (i.e. it must be *neutral*) or by strong interaction: otherwise, some signal would have been discovered so far; it must interact gravitationally and, at most, via weak interaction;
- it must be *stable* or at least long-living since it was present right after the Big Bang (this is proved by the CMB observations) and it is still present now.

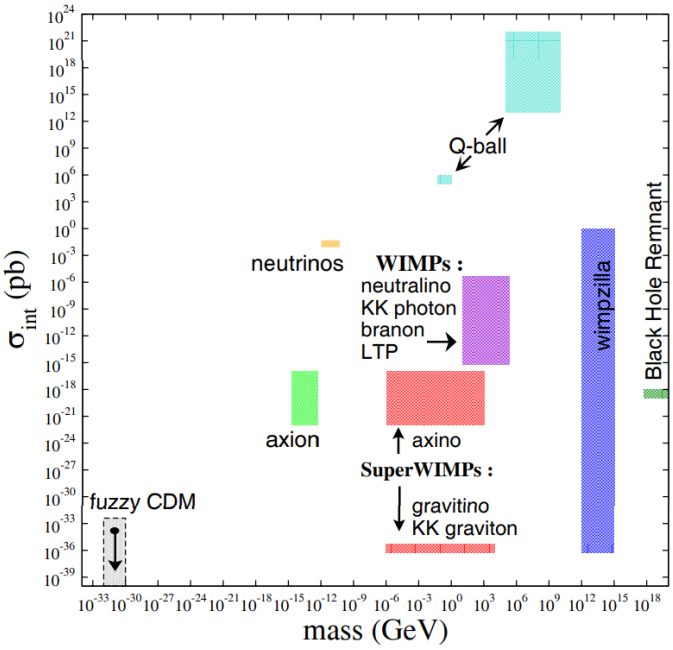

Figure 1.8: Examples of Dark matter candidates: each of them occupies a region in the mass-cross section space. Picture from [37].

An additional feature divides the model into three categories: *hot*, *warm*, and *cold* Dark Matter. 'Hot' stands for fast-moving, while 'cold' for non-relativistic. The big amount of models covers all three cases, even if the majority of them rely on the cold Dark Matter (CDM) paradigm. This latter is preferred because it can better explain the formations of gravitationally-bound structures in the primordial Universe, which, according to the theory, would have been formed through gravitational amplification of small density perturbations [38].

1.3.1 Particle candidates

Relic neutrinos

If one sticks with Standard Model particles, the only candidate that can satisfy the requests is the neutrino. It is neutral, stable, and weakly-interacting as required, and it seems to have a non-zero mass, as proved by its flavour oscillation discovered and then confirmed by several experiments [39, 40, 41]. However, there are constraints that assign it a very small mass [42]:

$$\sum_{i=1}^{3} m_i < 0.12\,\text{eV} \tag{1.28}$$

(where the sum covers the three mass eigenstates) making them a relativistic particle, a fact that goes against many models about Big Bang and structure formation, as explained above. In addition to this, that mass does not seem to be enough to account for the relic abundance of Dark Matter (1.27). In fact, it would be given by $\Omega_\nu h^2 = \sum_{i=1}^{3} m_i/93\,\mathrm{eV}$ and the limit (1.28) provides

$$\Omega_\nu h^2 < 0.0013\,. \tag{1.29}$$

For these reasons, Standard Model neutrino is usually kept out of the discussion.

Sterile neutrinos

As exposed in the last section, the reason why Standard Model neutrinos are rather unlikely to constitute the whole Dark Matter content of the Universe is essentially their small mass. A natural extension of the Standard Model, in this way, can be the existence of a different kind of neutrino, called *sterile neutrino*, with greater mass and fewer interactions [43].

Many theories have been developed in this field; most of them are based on the fact that the Standard Model interacting neutrino is known to have only a left-handed component. The existence of a right-handed counterpart, with a bigger mass, would provide a good Dark Matter candidate and at the same time represent a rather natural extension of the Standard Model. In one of the most accredited theories known as *Neutrino Minimal Standard Model (νMSM)*, three right-handed neutrino species are present; one of them, with mass $\sim$ keV, constitutes Dark Matter and the other two, with mass $\sim$ MeV, are able to explain the neutrino flavour oscillation, its low mass and also the Baryon Asymmetry of the Universe (BAU).

In these models for sterile neutrino N, the dominant predicted decay channel is $N \to \nu_\alpha \nu_\beta \overline{\nu_\beta}$, where α and β are any neutrino flavour. The relative decay width is given by [43]

$$\Lambda_{N\to 3\nu} = \frac{G_F^2 M^5}{96\pi^3} \sum_\alpha |\theta_\alpha|^2 \sim \frac{1}{1.5\cdot 10^{14}\mathrm{s}} \left(\frac{M}{10\,\mathrm{keV}}\right)^5 \sum_\alpha |\theta_\alpha|^2 \tag{1.30}$$

where G_F is the Fermi constant, M the sterile neutrino mass and θ_α is the mixing angle between N and a left-handed neutrino ($\alpha = e, \mu, \tau$). By requiring that this decay probability is small enough to provide a sterile neutrino lifetime greater than the age of the Universe ($\tau_N > t_{Universe} \sim 4.4\cdot 10^{17}\,\mathrm{s}$), a constraint on θ_α is derived:

$$\sum_\alpha |\theta_\alpha|^2 < 3.3\cdot 10^{-4} \left(\frac{10\,\mathrm{keV}}{M}\right)^5 . \tag{1.31}$$

Since νMSM aims to explain the left-handed neutrino mass differences through the sterile neutrinos, they should be given by $\delta m_\nu \sim M\theta^2$. Therefore, since the constraint (1.31), just one sterile neutrino species is not enough to explain the observed mass differences

[44], found by oscillation experiments ($\delta m_{sol} = 0.0086\,\text{eV}$). Moreover, two sterile neutrino species would imply the lowest-mass left-handed neutrino is massless. This is why in most of the models three sterile neutrinos are considered.

Axions

In the context of Quantum Chromodynamics (QCD), one well-known open problem is represented by the *strong CP problem* [45]. In order to properly describe and justify the mass of the η' meson [46], an additional term must be added to the lagrangian [47]:

$$\mathcal{L}_\Theta = \Theta \frac{g_s^2}{32\pi^2} G^a_{\mu\nu} \tilde{G}^{a\mu\nu} \tag{1.32}$$

where g_s is the strong coupling and $G^a_{\mu\nu}$ is the gluon-field-strength tensor. This term predicts a violation of the CP symmetry for values of the parameter Θ different from $n\pi$, with $n \in \mathbb{Z}$. This violation is not observed by strong interactions; experiments on neutron electric dipole moment [48] provide in fact the upper bound $|\Theta| < 10^{-9}$. Inserting QCD in the Standard Model theory, another term must be added to Θ, defining

$$\bar{\Theta} = \Theta + \arg\det M\,, \tag{1.33}$$

where M is the quark mass matrix which is required by the electroweak CP violation. So, we should set

$$\left|\bar{\Theta}\right| < 10^{-9} \tag{1.34}$$

and the reason for this value to be close to zero constitutes the strong CP problem.

Axions are a possible solution to this problem, representing at the same time another Dark Matter candidate. They have been introduced by Peccei and Quinn [49] by creating a new $U(1)$ symmetry known as *PQ symmetry*. It is spontaneously broken at a scale f_a. Its related Nambu–Goldstone boson is called precisely axion a [50]. In this way another term is added to the lagrangian:

$$\mathcal{L}_{PQ} = \frac{a}{f_a/N} \frac{g_s^2}{32\pi^2} G^a_{\mu\nu} \tilde{G}^{a\mu\nu}\,. \tag{1.35}$$

N is another parameter that enters the PQ theory. In this way, $\bar{\Theta}$ can naturally vanish if $a = -\Theta f_a/N$.

The scale of the PQ symmetry is constrained to

$$f_a/N \gtrsim 6 \cdot 10^8\,\text{GeV}\,; \tag{1.36}$$

from the theory, it corresponds to axions with mass

$$m_a \lesssim 0.01\,\text{eV} \tag{1.37}$$

making them one of the lightest Dark Matter candidates.

The search for axions is mostly conducted in the field of *primordial axions* (produced during the Big Bang) [51] and *solar axions* (continuously produced by the Sun) [52, 53].

Supersymmetric particles

Among the various extensions of the Standard Model, Supersymmetry (SUSY) is one of the most developed and experimentally tested, even if no evidence of supersymmetric particles has been found so far. The basic principle is that each fermionic particle that composes the Standard Model comes with a bosonic counterpart, called *superpartner*. They are usually named by prepending an 's' in the particle name (we get so *squarks* and *sleptons*). The vector bosons of the Standard Model are instead completed by a supersymmetric fermion.

In this way, each couple of fermions and relative boson is viewed as different realizations of the same particle. This symmetry is generated by an operator $\widehat{Q}$ [54], defined so that

$$\begin{aligned} \widehat{Q}\,|\text{fermion}\rangle &= |\text{boson}\rangle \\ \widehat{Q}\,|\text{boson}\rangle &= |\text{fermion}\rangle\ ; \end{aligned} \tag{1.38}$$

thus, $\widehat{Q}$ is able to modify the spin of a particle by 1/2, but does not change electric nor colour charge. In the Standard Model, there is no connection between particles and superpartners: each quark and lepton is described by a spin-1/2 field. Adding the fact that no supersymmetric particle has been detected so far, a conservation law can be associated to the Standard Model particles: a new quantum number called *R-parity* is introduced. It is defined as

$$R = (-1)^{3(B-L)+2S} \tag{1.39}$$

where B is the baryon number, L the lepton number and S the spin. For 'ordinary' particles $R = 1$, while $R = -1$ for their superpartners. In this way, postulating the conservation of R, the production of supersymmetric particles from ordinary matter is prevented, in agreement with experimental evidence [12].

Nowadays, a SUSY evidence is what particle physics experiments at accelerators such as LHC at CERN [55] mainly aim to. Supersymmetric partners of Standard Model elements are good candidates for Dark Matter. Their masses are, according to SUSY theory, greater than leptons and quarks masses. In particular, the supersymmetric particle with a smaller mass, usually called *Lightest Supersymmetric Particle (LSP)*, is predicted to be stable and one of the most promising candidates.

Among the predicted superpartners, some of the most important for Dark Matter models are the following:

- *sneutrinos*: supersymmetric partners of neutrinos, with an expected mass of the order of TeV. Being right-handed, they would solve at the same time the neutrino chirality problem. In some models, they constitute the LSP and are able to reproduce the correct Dark Matter relic density [56];

- *gravitino*: graviton superpartner, with a mass of the order of eV. Interacting only gravitationally, a direct detection would be very difficult;
- *neutralinos*: these particles are the most believed to be the LSP, able to constitute Dark Matter as *Weakly Interacting Massive Particles (WIMPs)* (further details will be exposed in Section 1.3.2).

1.3.2 Weakly Interacting Massive Particles

One class of Dark Matter candidates which gained more and more attention in the last years is that of Weakly Interacting Massive Particles, usually known as WIMPs [57] (and usually symbolized by the letter χ). They satisfy all the requests made by the observations, being neutral, weakly (or sub-weakly) interacting, stable or very long living[7] and with a mass between $\mathcal{O}\,(\mathrm{GeV})$ and $\mathcal{O}\,(100\,\mathrm{TeV})$. This last feature makes them belong to the CDM theory, the most accepted one. They are thought to be the kind of particles that most likely constitute Dark Matter.

The importance of WIMPs, in terms of both theoretical and experimental efforts, is due to their ability to explain the observed relic abundances (1.27) in a rather natural way. Let's consider indeed the mechanism which is supposed to have caused such DM abundance. The most accepted model on this is the *freeze-out mechanism*. It assumes that WIMPs were created in the early Universe and that they were in thermal equilibrium with ordinary matter, as long as the temperature was high enough. While the latter was decreasing, it reached a point where this equilibrium broke. While at high temperatures and high-density conditions, the WIMP particles were able to maintain equilibrium through annihilations into ordinary particles, after the freeze-out time they started being so rare that annihilations were basically prevented. Therefore, the annihilation rate is an important parameter, given by $\Gamma_{ann} = n_\chi \langle \sigma_{ann} v \rangle$, where n_χ is the WIMP number density and $\langle \sigma_{ann} v \rangle$ the temperature-averaged product of annihilation cross section and relative velocity. The density evolution is governed by the Boltzmann equation [59]:

$$\frac{dn_\chi}{dt} = -3Hn_\chi - \langle \sigma_{ann} v \rangle \left(n_\chi^2 - n_{\chi,eq}^2 \right) . \tag{1.40}$$

The number density decreases over time thanks to two sources; the one proportional to the Hubble parameter H is due to the Universe expansion, while the other term is related to annihilations. At the freeze-out, the equilibrium density is reached and this term is null, 'freezing' the WIMP density to the relic abundance. The final abundance strongly depends on the annihilation rate, namely $\langle \sigma_{ann} v \rangle$. Hence, for different values of the annihilation cross section, different Dark Matter abundances can be predicted. In Figure 1.9 the evolution of WIMP abundance as a function of time is shown for different assumptions on the cross-section.

[7] A recent study set the lower limit on Dark Matter lifetime to 160 Gyr at 95% confidence level [58].

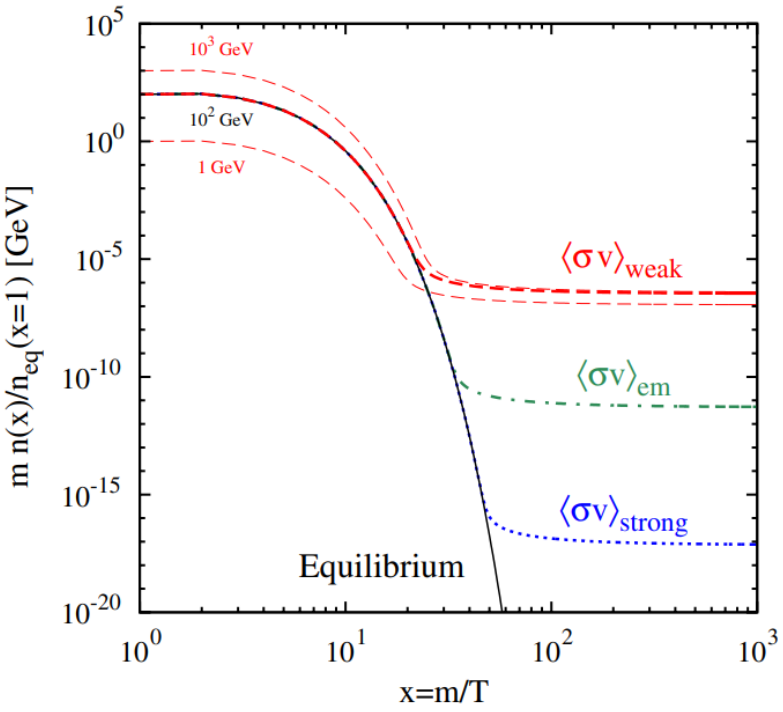

Figure 1.9: Evolution of the WIMP cosmic abundance [60]. On the x axis an adimensional parameter $x = m_\chi/T$ (where T is the temperature of the Universe) is used as a time parameterization. Weak, electromagnetic, and strong cross sections hypotheses are represented: they lead to abundances that differ by orders of magnitude. For the weak case, the mass dependence is also shown.

A simplified solution of (1.40) is reported in [57]. It assumes that the freeze-out happened approximately when the WIMP annihilation reached the Hubble parameter, $\Gamma_{ann} \sim H$. With this approach, the relic WIMP abundance is given by

$$\Omega_\chi h^2 \simeq \frac{T_0^3}{\rho_c}\frac{x_f}{\overline{M}_P}\frac{1}{\langle\sigma_{ann}v\rangle_f}h^2\,. \tag{1.41}$$

In this equation, T represents the Universe average temperature, ρ_c the *critical density* ($\rho_c := \frac{3H^2}{8\pi G_N}$), x the ratio m_χ/T and $\overline{M}_P$ the reduced Plank mass; the index f refers to a value taken at the freeze-out time, the index 0 at present time. Using the values $\rho_c \simeq 8\cdot 10^{-47}\,\mathrm{GeV}^4h^2$, $T_0 \simeq 2.35\cdot 10^{-13}\,\mathrm{GeV}$ and $x_f \sim 20-25$ [61] and imposing $\Omega_\chi = \Omega_{DM}$ we get:

$$\langle\sigma_{ann}v\rangle_f \sim 3\cdot 10^{-26}\,\mathrm{cm}^3\mathrm{s}^{-1}\,. \tag{1.42}$$

If one assumes an average speed of $\sim 0.1\,c$, the WIMP annihilation cross section turns out to be

$$\sigma_{ann} \sim 10^{-36}\,\mathrm{cm}^2 \tag{1.43}$$

which is at the scale of weak interactions. This remarkable feature of the WIMP theory is known as *WIMP miracle* and it is the reason why many experiments started searching for this kind of particle.

The neutralinos

Among the particles predicted by the Supersymmery theory, the neutralino has the greatest chance to constitute Dark Matter as WIMP. According to SUSY, four neutralinos exist as linear combinations of the *bino* $\tilde{B}$ (superpartner of the $U(1)$ gauge electroweak field), the *Z-ino* $\tilde{W}^3$ (superpartner of the Z^0 boson) and two neutral *higgsinos* $\tilde{H}_1$ and $\tilde{H}_2$ (superpartners of the neutral Higgs bosons). They are all neutral, Majorana and spin-1/2 particles [62], usually denoted as $\tilde{\chi_1}$, $\tilde{\chi_2}$, $\tilde{\chi_3}$ and $\tilde{\chi_4}$. The lightest one is predicted to be stable: this feature makes it the most promising Cold Dark Matter candidate. It can be expressed as

$$\chi := \tilde{\chi_1} = Z_{11}\tilde{B} + Z_{12}\tilde{W}^3 + Z_{13}\tilde{H}_1 + Z_{14}\tilde{H}_2 \tag{1.44}$$

where Z_{ij} are the elements of the matrix that diagonalizes the neutralino mass matrix [63].

The experiments looking for a Dark Matter signal rely on the coupling that this latter should have with Standard Model particles (more details on this will be given in Section 1.4). A coupling can lead to WIMP *annihilation* producing Standard Model particles or, typically, *elastic scattering* on nucleons. Those processes can be divided into *spin-independent (SI)* and *spin-dependent (SD)* interactions.

In the first case, the interaction is scalar; it is described by a lagrangian of the form

$$\mathcal{L}_{scalar} = a_q \overline{\chi}\chi\overline{q}q \tag{1.45}$$

where q is a generic quark and a_q is the interaction coupling between WIMPs and quarks. The total cross-section for the scattering is given by

$$\sigma_{SI} = \frac{4m_r^2}{\pi} f_{p,n}^2 \,, \tag{1.46}$$

where m_r is the nucleon reduced mass and $f_{p,n}$ is the coupling with protons and neutrons. For a nucleus (A, Z) the zero momentum transfer cross-section can be therefore expressed as

$$\sigma_{SI,nucleus} = \frac{4m_r^2}{\pi} \left[Z f_p^2 + (A - Z) f_n^2\right]^2 . \tag{1.47}$$

The SD interactions can be of two kinds. The interaction lagrangian for axial-vector interactions with coupling d_q is

$$\mathcal{L}_{AV} = d_q \overline{\chi}\gamma^\mu\gamma_5\chi\overline{q}\gamma^\mu\gamma_5 q \tag{1.48}$$

expressed with the Dirac matrices γ. The scattering cross-section in this case reads [64]

$$\frac{d\sigma}{d\left|\vec{v}\right|^2} = \frac{1}{2\pi v^2}\overline{\left|T\left(v^2\right)\right|^2} \tag{1.49}$$

where v is the relative velocity and $T\left(v^2\right)$ the interaction matrix element. It can be proven that this SD cross-section vanishes for nuclei with a total spin equal to 0. The other kind of SD interaction is the vector one:

$$\mathcal{L}_V = d_q \overline{\chi}\gamma_\mu \chi \overline{q}\gamma_\mu q\,. \tag{1.50}$$

The Feynman diagrams of bot SI and SD neutralino-quark interactions are represented in Figure 1.10.

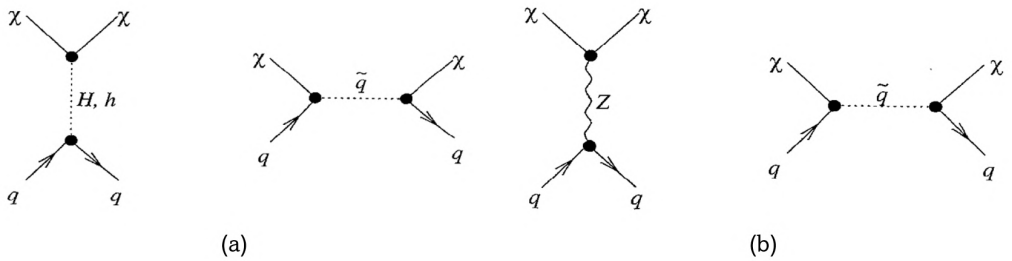

Figure 1.10: Feynman diagrams for neutralino-quark SI interaction (a) and for neutralino-quark axial-vector SD interaction (b). From [62].

1.4 Dark Matter detection techniques

The Dark Matter evidence exposed in Section 1.2 are numerous and robust. However, they all rely on indirect observations, such as gravitational effects or anisotropies in the CMB. One big step forward in the comprehension of DM would be a signal coming from its interaction with ordinary matter. In this way, it would be possible to study its properties and possibly understand its nature. Thanks to all the theoretical hypotheses developed in the years, some of them exposed in the last Section, the number of experiments looking for DM signals has been growing for years; in particular, WIMPs have gained more and more interest. The experiments looking for Dark Matter are usually subdivided into three groups, based on the type of interaction they look for.

Indirect detection experiments (Section 1.4.1) rely on the DM annihilation process and look for a signal from the Standard Model particles produced from it.

The opposite process is also possible: Standard Model particles can annihilate and produce Dark Matter particles. Efforts to detect a signal in this way are made by high energy accelerators, constituting DM *production experiments* (Section 1.4.2).

Another way to detect DM is through their scatter on Standard Model particles, in particular on nuclei. *Direct detection experiments* (Section 1.4.3) search for such signal.

In Figure 1.11 a schematic representation of the different DM detection channels is shown.

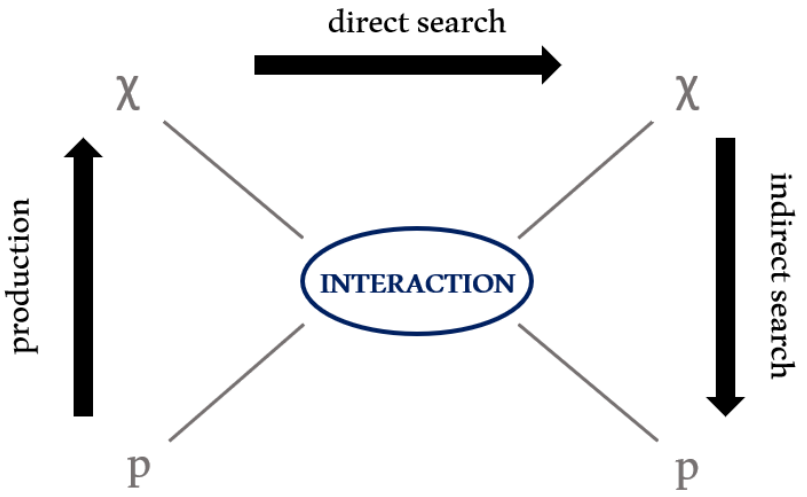

Figure 1.11: Schematic of the different attempts to observe DM; χ is a DM particle or antiparticle and p is a Standard Model particle or antiparticle. Indirect search: $\overline{\chi}\chi \to \overline{p}p$; production: $\overline{p}p \to \overline{\chi}\chi$; direct search: $\chi\, p \to \chi\, p$.

1.4.1 Indirect detection experiments

After the freeze-out, the number of WIMP particles has basically remained unchanged; however, even if far more rarely, annihilation processes keep undergoing across the Universe, in particular in high WIMP density regions. Many experiments, on the Earth surface or in the atmosphere, are looking for products of these annihilations. The main channels are γ-rays, neutrinos, and antimatter in cosmic rays [65].

γ-ray telescopes

One of the most relevant features of the observations of cosmological γ-rays is that they are not deflected by magnetic fields and travel in straight lines. Thus, gamma signals can be very useful in recognizing the position of the emission source. What

is not straightforward in this field, however, is to disentangle the DM signal from the background. The attempts to do it use mostly the spectral shape of the emission; the best signatures would be monoenergetic peaks, but the branching ratios for this kind of processes are thought to be very small [12].

At energies from $\sim 10^2$ MeV to $\sim 10^5$ MeV, the most sensitive experimental technique is that of satellites instrumented with pair-conversion detectors. The most relevant projects in this regard have been EGRET [66], which was able to isolate a considerable number of sources [67], and Fermi-LAT [68]. The former was more interested in the $0.1 - 10$ GeV energy range while the latter in $30 - 200$ GeV. Their region of interest was in both cases the galactic center, where the higher mass-to-light ratio is observed: no WIMP signal was found [69].

At higher energies, gamma rays are more commonly observed by ground-based experiments[8]. Since at those energies γ-rays interact with the atmosphere, they are detected in an indirect way, by looking at the shower of produced particles. These kinds of detectors are usually called Imaging Air Cherenkov Telescopes (IACT), since they look for the Cherenkov light produced by the charged particles of the electro-magnetic showers in the atmosphere. One disadvantage of this method, compared to satellite detectors, is the background coming from charged cosmic rays. Relevant examples of the application of this technique are HESS [70], MAGIC [71] and VERITAS [72]. A new generation of detectors is under development, namely the Cherenkov Telescope Array (CTA) [73].

Neutrino telescopes

Neutrinos are another very important channel for the WIMP indirect search. They travel in straight paths due to their neutral electric charge, as well as photons. Moreover, since they rarely interact with matter, neutrinos can be detected from massive objects such as the Sun, from which they can escape; Dark Matter accumulates there because of the gravitational attraction and the scatterings but at the same time, if neutrinos are produced by DM annihilations, they are likely not self-absorbed. They can provide information both on the WIMP annihilation directly into a $\overline{\nu}\nu$ couple and, as secondary particles, into couples of charged particles like $\tau^+\tau^-$ and $\bar{b}b$.

Neutrino telescopes typically use the Cherenkov light produced by charged particles coming from the interaction of neutrinos in the detector (or nearby it). Examples of telescopes applying this method are ANTARES [74] and IceCube [75]. ANTARES is an underwater $0.1\,\mathrm{km}^3$ telescope, placed 2400 m deep in the Mediterranean Sea. IceCube is instead placed at the South Pole and has dimensions of $1\,\mathrm{km}^3$ scale. They both look for TeV-scale 'up-going' neutrino: ANTARES is sensitive to the southern hemisphere sources and IceCube to the northern hemisphere ones. KM3NeT [76], the upgrade of ANTARES, is under construction in the Mediterranean Sea and will host almost 200

[8] In fact, the flux of photons at such high energies are too small to detect them in an effective way in the atmosphere, where the detectors have necessarily limited dimensions.

thousands of photomultipliers, covering $\sim 1\,\mathrm{km}^3$ volume. Super-Kamiokande, placed in the Kamioka mine in Japan [77], even if not properly a neutrino telescope can contribute to Dark Matter indirect search. Upgrade of Kamiokande, it adopts more than 11000 PMTs for a 50 ktons cylindrical detector. It has been and is one of the most relevant projects for neutrino physics, especially for its discoveries regarding neutrino oscillation [78, 79].

The studies of neutrino probes led to exclusion limits on $\overline{\chi}\chi$ annihilation cross-section. Exclusion limits coming from a 2015 IceCube analysis [80] are shown in Figure 1.12.

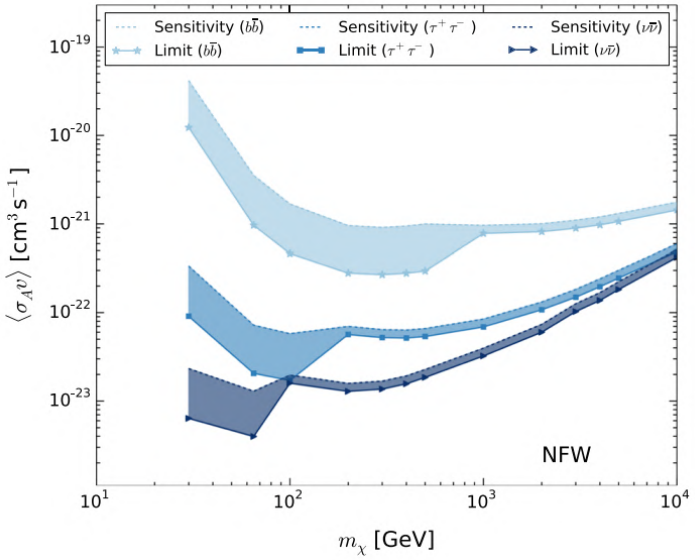

Figure 1.12: IceCube WIMP annihilation exclusion limits as a function of WIMP mass [80]. Sensitivities and limits are plotted for the channels $\overline{\chi}\chi \to \bar{b}b$, $\overline{\chi}\chi \to \tau^+\tau^-$ and $\overline{\chi}\chi \to \overline{\nu}\nu$, assuming a NFW Dark Matter profile.

IceCube, SuperKamiokande and KM3NeT are represented in Figure 1.13.

Antimatter in cosmic rays

Charged cosmic rays arriving at Earth atmosphere mainly consist of protons, nuclides and, in smaller abundances, electrons. Antimatter such as antiprotons and positrons are only produced in rare processes and a low frequency of them is expected; hence, even a relatively small number of such events can be a good WIMP annihilation signature. These signatures are mostly pursued by satellite experiments as PAMELA [84], AMS-02 [85] (placed on the International Space Station), and Fermi-LAT. While the antiproton spectrum does not show any statistically relevant excess, the e^+ flux measured by all the above-mentioned detectors results in an excess in the energy range 5-350 GeV (see Figure 1.14.

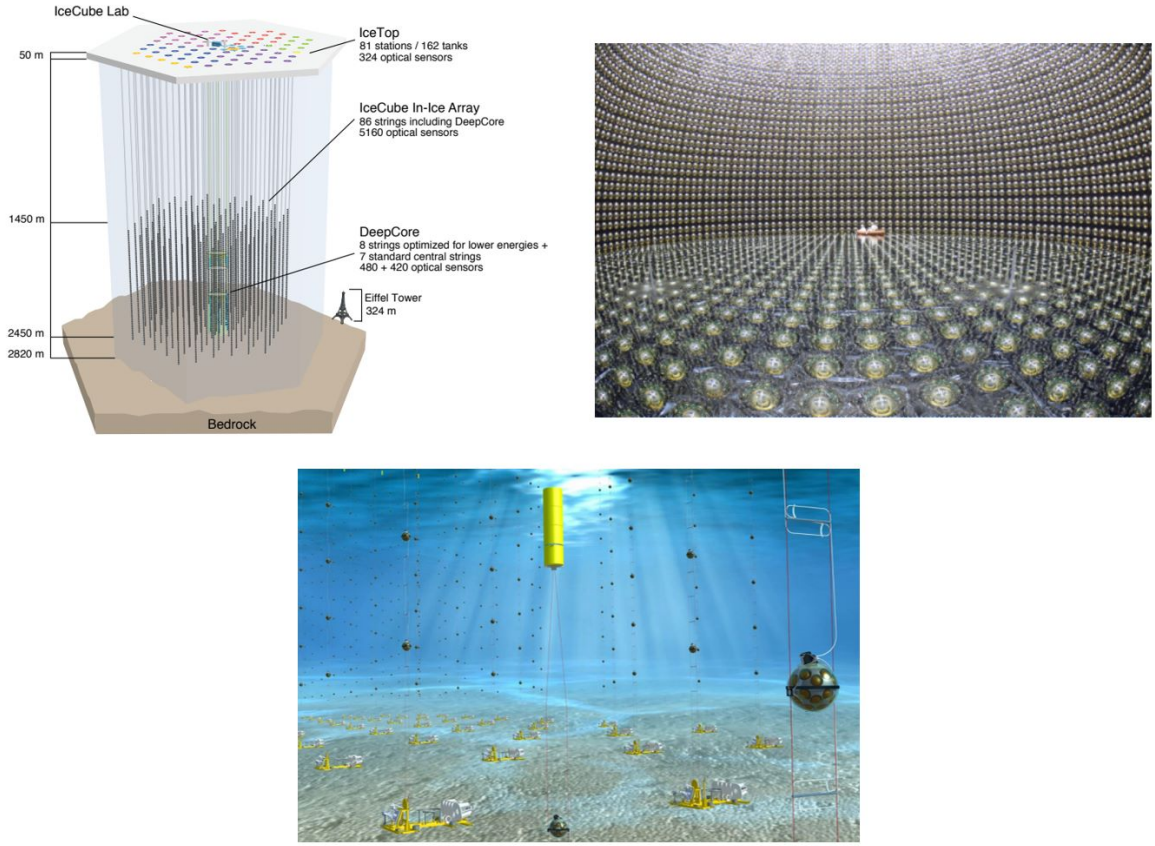

Figure 1.13: Present and future neutrino telescopes. Top-left: IceCube rendering [81]; top-right: picture of SuperKamiokande from inside [82]; bottom: artistic representation of how KM3NeT will look like [83].

From the plot, it is clear that the common models describing the propagation of cosmic rays across the Universe is not able to explain the observed spectrum of positrons. WIMP annihilations would certainly provide a coherent explanation to this; however, there are other possible causes. First, the physics of cosmic ray propagation could need a modification, although it is able to describe a big amount of experimental data. Second, other sources could be responsible for such positron excess, such as nearby pulsars [86]. In addition, the absence of an antiproton excess would suggest a leptonic preference for WIMP annihilation, which is not a natural assumption. The search for anisotropies in the arrival directions of positrons by AMS-02 could represent, in the future, a further element.

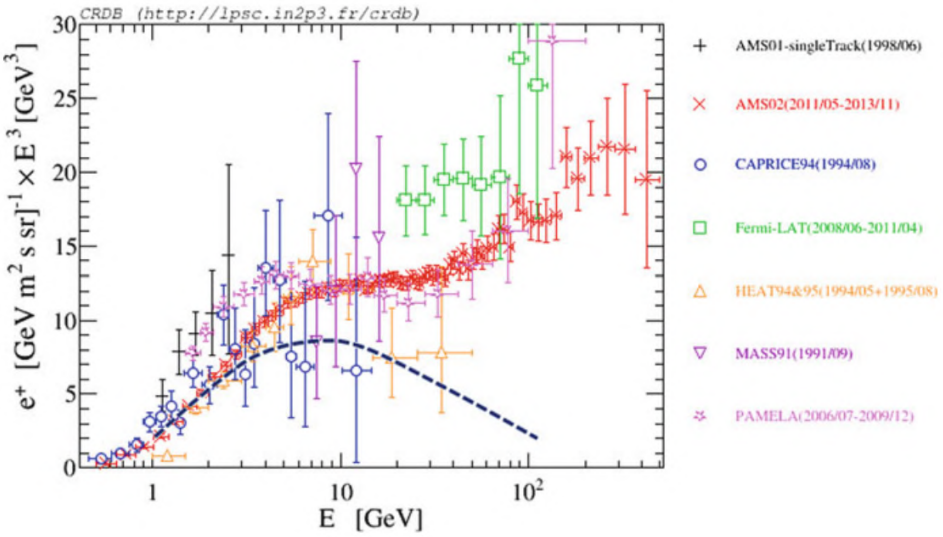

Figure 1.14: Positron flux multiplied by its energy at the third power: data by different experiments (especially AMS-02, in red). The dashed line is the expected spectrum coming from the cosmic ray propagation simulations. Plot from [12].

1.4.2 Production experiments

Thanks to the $\mathcal{O}(10$ TeV) center-of-mass energy reached by the Large Hadron Collider (LHC) at CERN, in addition to its world-leading research in high energy physics, it can be also a powerful instrument for WIMPs research. In fact, many WIMP models predict mass ranges just above the electroweak spontaneous symmetry-breaking energy. Possible 'signatures' for WIMPs in this context are events with some energy missing, due to WIMPs produced in the process and not interacting in the detector [57]. This signature suggests the presence of a neutral and stable particle in the final state of the collision. When looking for WIMPs at LHC, the kind of event of interest is the so-called *Mono-X*; it should include a large missing momentum and a recoil object, which can be a jet, a gauge boson, or a lepton. Experiments such as ATLAS [87] and CMS [88] are particularly fitting for such events. In Figure 1.15 the exclusion limits on the WIMP-nucleon scattering cross section in both SD and SI cases are shown, from a CMS analysis published in 2017 [89]. The production channel provides in general a lower sensitivity with respect to the other two; however, it is important to have complementary methods to make exclusions or discoveries more robust.

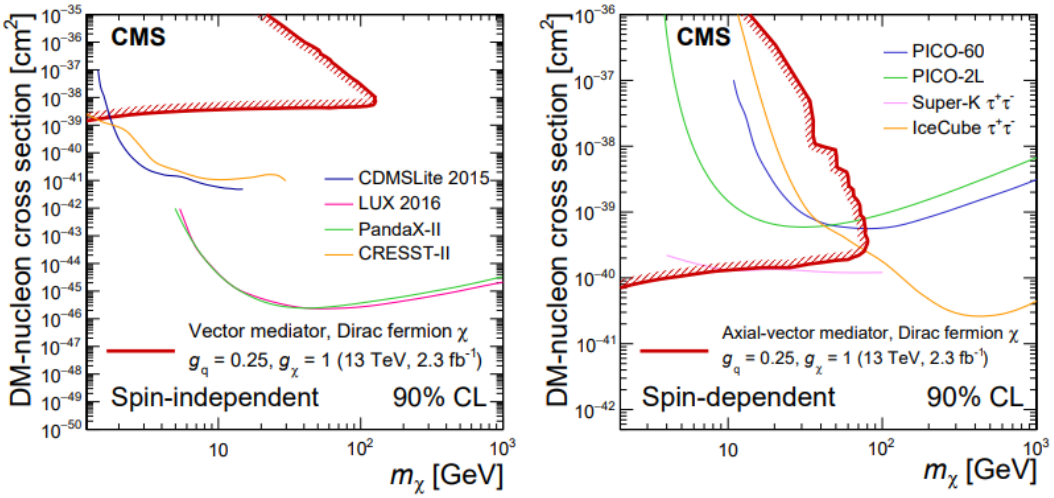

Figure 1.15: Limits on WIMP-nucleon scattering cross-section [89]. The absence of WIMP evidence is translated into a scattering cross-section and compared to experiments adopting other techniques. The difference in the excluded regions highlights the complementarity of the different methods.

1.4.3 Direct detection experiments

The idea behind the direct detection of Dark Matter is simple: since we know from galactic models that a DM halo in thermal equilibrium permeates the great majority of the observed galaxies, one can try to detect DM particles present in the Milky Way halo by direct interaction. The thermal equilibrium of the halo ensures that a DM particle has a null average speed in the galactic frame; however, due to the statistical distribution of speeds of the Dark Matter particles, a relative velocity between the Milky Way DM halo and the Earth is present. This makes possible for DM particles to interact with a target placed on Earth, with a probability proportional to the WIMP interaction cross-section with ordinary matter. Moreover, the solar system turns around the galactic center with a velocity of about 200 km/s: this speed is summed to the DM one and leads to a larger relative velocity for a given direction.

As already pointed out, the WIMP interaction cross section[9] is expected to be very small. A direct Dark Matter detection experiment consists in finding an extremely rare event on top of a potentially huge number of background sources. For this reason, there are strict requirements that they must satisfy.

First of all, it should be hosted by a deep-underground laboratory to reduce the background coming from cosmic radiation. The only cosmic background there, besides neutrinos, is due to muons; at a sufficient depth the rate of muons is reduced enough

[9] As well as the majority of the other Dark Matter particle candidates.

to allow for sensitive DM searches (see Figure 1.16), also with the help of dedicated *veto systems*. 14 underground laboratories are currently present in the world; they host experiments mainly interested in neutrino physics and rare decays in addition to DM direct search.

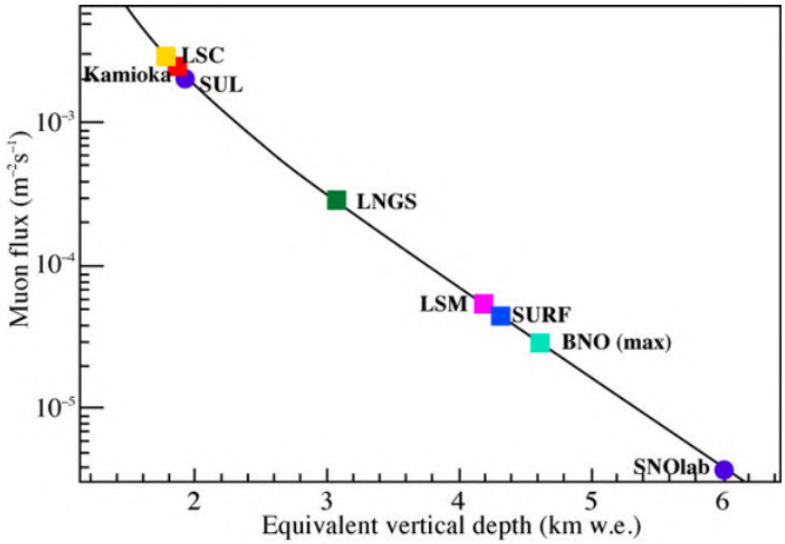

Figure 1.16: Some of the most important deep-underground laboratories in the world [90]. Among them, LNGS in Italy, SNOLab in Canada and the Kamioka Observatory in Japan host several projects aiming at the direct detection of Dark Matter. The depth in water equivalent (x axis) is related to the muon flux (y axis).

Another very important requirement is an extremely low background due to radioactivity in the environment and in the detector materials. This can be realized by adopting a strict material radioassay to reduce as much as possible the material radioactivity; good environmental shielding is essential as well; accurate background models are also required. α, β and γ radiations are all natural backgrounds to take into account; when the search is focused on WIMPs, another very dangerous background source comes from neutrons, due to their neutral electric charge and $\sim$ GeV mass which make them produce signals identical to WIMP ones.

Since the signal rate is extremely small, another way to increase the sensitivity of such experiments is, of course, to increase the *exposure*. This can be obtained in two ways: by increasing as much as possible the dimensions of the active target of the experiment and, on the other side, increasing its lifetime. The exposure is usually defined as the product of the effective mass of the target and the time of data acquisition.

There are additional DM *signatures* that can help discriminate between signal and background. One of them is the signal *directionality*. A DM signal is indeed expected

to be non-isotropic; the solar system motion around the Milky Way provides a greater relative velocity with respect to the Dark Matter halo towards a well-known direction, which increases the interaction rate. An *annual modulation* of the signal would represent a strong signature as well. The Earth revolution around the Sun provides a speed of about $30\,km/s$, which adds to the solar system one. Considering again that the event rate is proportional to the relative velocity, we can expect an annual modulation in the number of events found[10]. These two signatures can be very powerful since the background does not show in general neither a directional or annual modulation. Another tool used to discriminate between signal and background, in the case of WIMPs, is the distinction between *Nuclear Recoil (NR)* (when the scattering happens on target nuclei) and *Electronic Recoil (ER)* (when it happens on shell electrons). WIMPs are expected to produce NRs. Therefore, the impact of ER backgrounds (β and γ, which are typically much more abundant than NRs) can be greatly reduced thanks to the ER/NR discrimination

On top of the common properties and different strategies stated above, several kinds of detectors have been proposed and used for this class of experiments. The basic principle is to convert the very small amount of energy released by a hypothetical DM scattering on the detector to a measurable signal. The channels usually employed are *scintillation light*, *ionization electrons*, and *phonons*. Among the different techniques, there are *cryogenic detectors*, *scintillation crystals*, and *noble liquid detectors*.

Solid state cryogenic detectors

The strategy adopted by cryogenic detectors is to keep the system at very low temperatures, reaching the order of ~ 10 mK. Phonons caused by a temperature increase are detected with semiconductors operating near their phase transitions [91]: in this way the heat is converted into an electrical signal. Some of them are able to collect the scintillation light as well, useful to reject background events; an example is CRESST [92], which uses nuclei of $CaWO_4$ crystal as a target. The CDMS experiment and its upgrade SuperCDMS [93] use instead silicon and germanium crystals and superconductive tungsten to detect phonons; they are able to detect also the ionization signal using a bias voltage and a charge collecting electrode [94]. EDELWEISS [95] also measures both phonons and the ionization energy, with the ability to discriminate between ER and NR events. All these experiments found null results.

Scintillating crystals

Scintillating crystals are used in most of the fields of particle physics; they are relevant also for DM search, especially due to their low energy threshold. They make use of materials with a strong emission of scintillation light after the passage of a particle. They are

[10]The rate should be maximal in June and minimal in December.

usually instrumented with photomultiplier tubes to detect the photons emitted. Pulse shape discrimination can be used in this case to distinguish nuclear from electronic recoils; they often rely, in addition, on the annual modulation. DAMA/LIBRA [96] (and the former DAMA/NaI) at LNGS exploits this technique, using $\sim$ 250 kg of highly radiopure NaI(Tl) crystal. On the surfaces of the detector, quartz light guides connect it to low-background PMTs. In more than 13 years of data taking, DAMA/LIBRA accumulated 2.46 ton-years exposure and published in 2018 the results of phase-1 and phase-2 combined data [97], claiming an annual modulated DM signal with $12.9\,\sigma$ confidence level. When this impressive result is interpreted as WIMP-nucleon SI interactions, two allowed regions in the mass-cross section space can be identified, with a Dark Matter mass from a few GeV up to $\sim$ 100 GeV. Anyway, as it will be shown later, other experiments set exclusion limits on the WIMP cross-section that exclude those regions.

After the results of DAMA/LIBRA (which is still taking data and increasing its statistics), other projects arose, aiming to reproduce the same evidence with similar techniques, to confirm or deny the presence of a DM signal. COSINE [98] is a NaI(Tl) crystal experiment located at the Yangyang underground laboratory in South Korea. After 1.7 years of data taking they did not find any signal consistent with Dark Matter [99]. Recently, they also tried to reproduce the DAMA/LIBRA annual modulation using the same analysis methods as DAMA; interestingly, it resulted in an annual modulation with an opposite phase [100]. This suggests a possible biased analysis and adds a new element for the understanding of the DAMA/LIBRA results. The COSINUS [101] project also relies on a NaI crystal, with in addition the possibility to detect phonons. This latter provides a precise energy measurement while the scintillation light makes particle identification possible; the two information together allow a huge background reduction. COSINUS is currently under construction at LNGS in Italy and will search for a possible annual modulation. Another project looking in this direction is SABRE [102], which aims to search for the annual modulation with two detectors, one placed in the northern hemisphere and one in the southern hemisphere. This will give the chance to see, if the sinusoidal behaviour is present, and what is the relative phase between the two detectors. As the annual modulation is a global feature, a zero phase is expected in the case of a DM signal. Instead, if the observed modulation is a seasonal artifact, the phase would rule out Dark Matter from the possible causes.

Noble liquid detectors

Noble elements kept in liquid states have properties that make them appropriate targets for DM search [103]; the most successful detectors based on noble liquids are *dual-phase Time Projection Chambers (TPC)*. They are capable to reach $\sim$ keV energy thresholds. Among the noble elements, Argon and Xenon are the most used nowadays for this purpose. Xenon, in particular, has relevant features:

- due to its high mass number (A = 131) it has a high WIMP-nucleus SI scattering

cross section (it scales as A^2 by (1.47));

- due to its high atomic number (Z = 54) it has strong self-shielding properties;
- it is highly radiopure;
- it has odd-neutron isotopes: this makes it be sensitive to SD interactions in addition to SD interactions.

The energy released in an elastic scattering, either off a nucleus or a shell electron, provides kinetic energy to the recoiling particle; the recoiling particle, in turn, releases its energy through two different channels: excitations of the atomic electrons (which is followed by scintillation light) and ionizations. In double-phase detectors, an electric field is applied to drift the electrons along the liquid region, extract them in the gaseous phase and detect the secondary scintillation light emitted after their interaction with the gas atoms. Two signals are thus obtained, one coming from the scintillation (S1) and one from the ionization (S2). The energy of the event can be reconstructed by combining the reconstructed energies of the two signals; moreover, taking the ratio between them, a powerful ER/NR discrimination is possible. In fact, a recoiling nucleus travels a shorter path due to its high electrical charge and the electrons produced by the ionizations have more chances to recombine with ions; in noble elements, this recombination leads to additional scintillation emission that contributes to S1. Hence, for ER events the S2/S1 ratio is greater than for NRs.

Experiments such as XENONnT [104], LUX-ZEPELIN (LZ) [105] and PandaX-4T [106] use a Xenon double-phase detector for WIMP search and they have similar sensitivities. In the future, the DARWIN [107] project will also use liquid Xenon as a target with an increased mass. DarkSide-50 [108] and the future DarkSide-20k [109] use instead double-phase Argon.

None of the present noble element experiments found any WIMP signal. As they are upgrading their experimental setups and increasing the exposure, new regions of the WIMP mass-cross section space are being explored. The limits set by different experiments up to 2021 are shown in Figure 1.17.

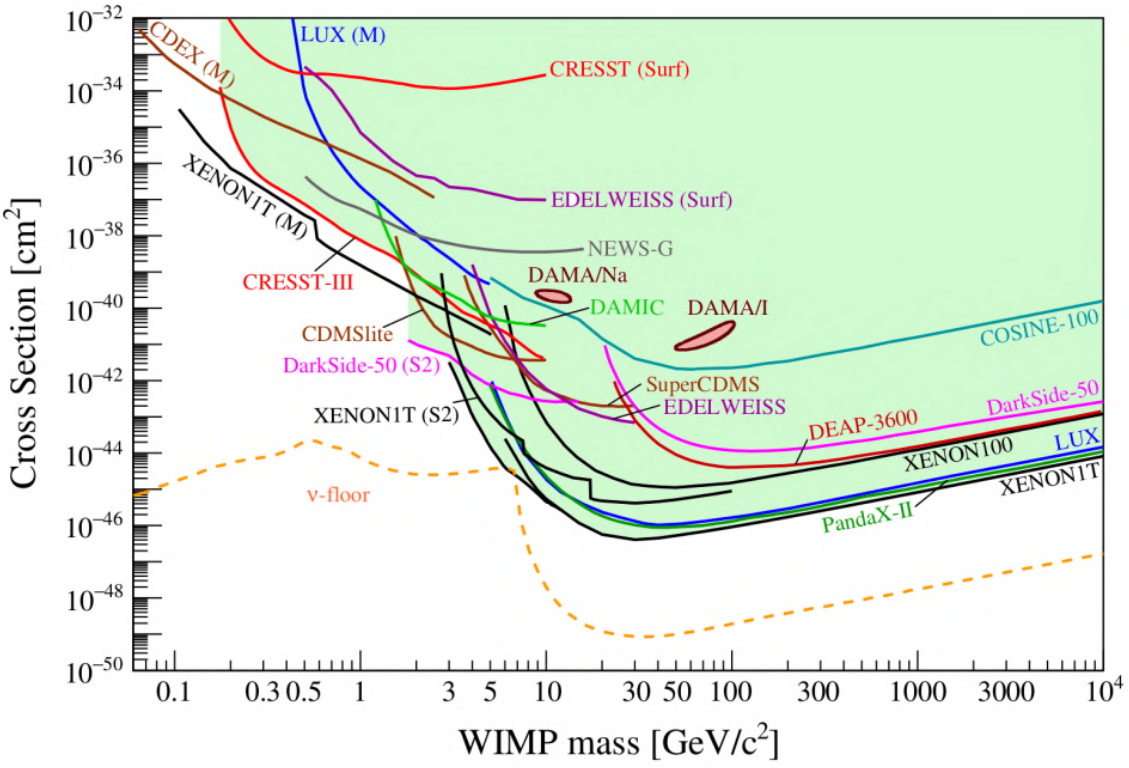

Figure 1.17: Exclusion limits on the spin-independent WIMP-nucleon interaction cross section, as a function of the WIMPs mass, for different works, up to 2021. From [110].

Chapter 2

The XENONnT experiment

The XENON project started in 2005, when the first detector called XENON10 [111] has been installed and commissioned at the INFN Laboratori Nazionali del Gran Sasso (LNGS) in Italy; consisting in a $\mathcal{O}(10\,\text{kg})$ Xenon double phase Time Projection Chamber (TPC), it was the prototype of this kind of detectors, demonstrating its effectiveness as direct Dark Matter detector. Important upgrades in the later years made it possible to increase the sensitivity by orders of magnitude, eventually reaching the multi-tonne scale with XENONnT [104], which was installed in 2020 at LNGS. Its key features include an increased target mass and a huge background reduction, facilitated by innovative active veto systems for muons and neutrons.

2.1 Xenon double-phase TPCs

As mentioned in Section 1.4.3, one of the most promising techniques for the direct Dark Matter search employs noble elements, kept in liquid or in double-phase state. Xenon double-phase TPCs currently provide the most stringent limits on the WIMP-nucleon interaction cross-section and have been also used to search for axions [112, 113, 53] as well as for two-neutrino double-electron capture (2νECEC) and neutrino-less double-β decay ($0\nu\beta\beta$) [114]). The importance of such detectors is mainly due to the possibility of running with a large mass of the active target, and of strongly mitigating the backgrounds.

2.1.1 Xenon properties

Natural Xenon has seven stable isotopes with an overall abundance of more than 90 %; among them ^{129}Xe, ^{131}Xe and ^{132}Xe are the most abundant, accounting for almost 75 % of the total. Two additional isotopes are present in nature, ^{124}Xe and ^{136}Xe, unstable (decaying respectively via $2\beta^+$ and $2\beta^-$) but with half-lives much greater than the Uni-

verse age ($> 10^{21}$ years). The lack of intrinsic radioactivity is one of the features that makes Xenon well-suited for rare events search. For WIMP direct detection experiments, the presence of two stable odd-neutron isotopes (^{129}Xe and ^{131}Xe) makes it also sensitive to the Spin-Dependent interaction channel.

Besides the nuclear properties, an important role is played by the chemical properties of Xenon. Being a noble element, it is naturally non-reactive and thus easy to find pure, even if it is not abundant on Earth. Moreover, when kept at ~ 2 bar of pressure its density is $\sim 3\,\mathrm{g/cm^3}$ and its boiling point is $\sim 178\,\mathrm{K}$: it can be maintained in a liquid state without reaching extremely low temperatures.

Xenon has also relevant scintillation and ionization properties. Per each keV of deposited energy, it emits ~ 50 photons and yields ~ 60 electron-ion pairs. The scintillation light has a wavelength of 178 nm to which it is self-transparent. Being in the VUV light range, wavelength shifters are not necessary (contrary to Argon detectors). An important feature of scintillation and ionization yields in Xenon is that the total amount of *energy quanta*, summing up scintillation photons and ionization electrons, is conserved.

The emission of a scintillation photon can occur in a direct way through

$$\begin{aligned} \mathrm{Xe}^* + \mathrm{Xe} &\rightarrow \mathrm{Xe}_2^* \\ \mathrm{Xe}_2^* &\rightarrow 2\mathrm{Xe} + h\nu \end{aligned} \tag{2.1}$$

where Xe^* denotes an excited Xenon atom; the process happens via the production of the *excited dimer* Xe_2^*. Instead, when a ionization occurs the atom is splitted in a electron-ion pair. In absence of electric field they recombine to form a neutral atom[1]. In this case, however, there is no loss of information since the atom is left in an excited state. At the end of the chain a scintillation photon is emitted:

$$\begin{aligned} \mathrm{Xe}^+ + \mathrm{Xe} &\rightarrow \mathrm{Xe}_2^+ \\ \mathrm{Xe}_2^+ + e^- &\rightarrow \mathrm{Xe}^{**} + \mathrm{Xe} \\ \mathrm{Xe}^{**} &\rightarrow \mathrm{Xe}^* + \mathrm{heat} \\ \mathrm{Xe}^* + \mathrm{Xe} + \mathrm{Xe} &\rightarrow \mathrm{Xe}_2^* + \mathrm{Xe} \\ \mathrm{Xe}_2^* &\rightarrow 2\mathrm{Xe} + h\nu\,. \end{aligned} \tag{2.2}$$

The fact that in both cases the scintillation light is emitted by the excited dimer state Xe_2^* is crucial for the photon detection: indeed, the photon energy does not correspond to any atomic Xenon structure; hence it is not absorbed by the surrounding xenon atoms and can reach the photosensors.

[1] It may happen, although with a smaller probability, also in presence of a drift field.

2.1.2 Working principles

Double-phase Xenon TPCs usually have a cylindrical shape, with a target mass of liquid Xenon (LXe) and a thin layer of gaseous Xenon (GXe) on top of it. The xy plane is parallel to the cylinder base while the z axis is parallel to the cylinder axis. The TPC is immersed in a cryostat keeping a constant inner temperature.

Three main electrodes are needed to apply electrostatic fields in the different regions of the detector:

- the *cathode* is placed at the bottom of the TPC and kept at a negative voltage;
- the *gate* is placed close to the liquid/gas surface, at ground voltage;
- the *anode* is placed at the top of the TPC, at a positive voltage.

Other electrodes can be employed for screening or as 'shaping wires'. The field inside the LXe volume, between the cathode and the gate, is called *drift field* and is used to drift the electrons released from the atoms after an ionization. The field inside the GXe volume, between the gate and the anode, is instead called *extraction field* and is used to extract the drifted electrons in the Xenon gas and accelerate them until they produce proportional scintillation light. Both fields must be directed parallel to the z direction and as uniform as possible; the drift field is usually of the order of 100 V/cm while the extraction field is much stronger, of the order of 10 kV/cm.

The top and bottom surfaces of the TPC are covered by PMT arrays which must be low-radioactive and sensitive to the Xenon scintillation wavelength. The lateral surface is covered by a material with high reflectivity for such wavelengths to enhance the collection efficiency, as polytetrafluoroethylene (PTFE) [115].

When a signal or background event happens within the LXe volume, either an electron or a nucleus gains recoil energy which is released to the Xenon atoms. Two different signals are expected. The first one (S1) comes from the scintillation photons, emitted isotropically and reaching both the top and the bottom PMT arrays. The ionization electrons are then drifted towards the liquid/gas surface, where they are extracted and accelerated by the extraction field, finally emitting a second scintillation light (S2). Due to its emission position, this latter is mainly observed in the top PMT array.

Assuming that the electrons travel parallel to the z axis, by looking at the distribution of S2 signal in the top array it is possible to estimate the xy position of the event. Moreover, since the drift velocity is constant and well known, by the time delay between S1 and S2 it is possible to infer the z position of the event. In this way, the 3D position of the interaction is completely reconstructed.

Figure 2.1 schematically shows the operations of a double-phase Xenon detector.

It has been mentioned that the total number of energy quanta is conserved. For this reason, the event energy can be estimated by summing the two signals S1 and S2 after applying appropriate corrections. These corrections depend on the reconstructed

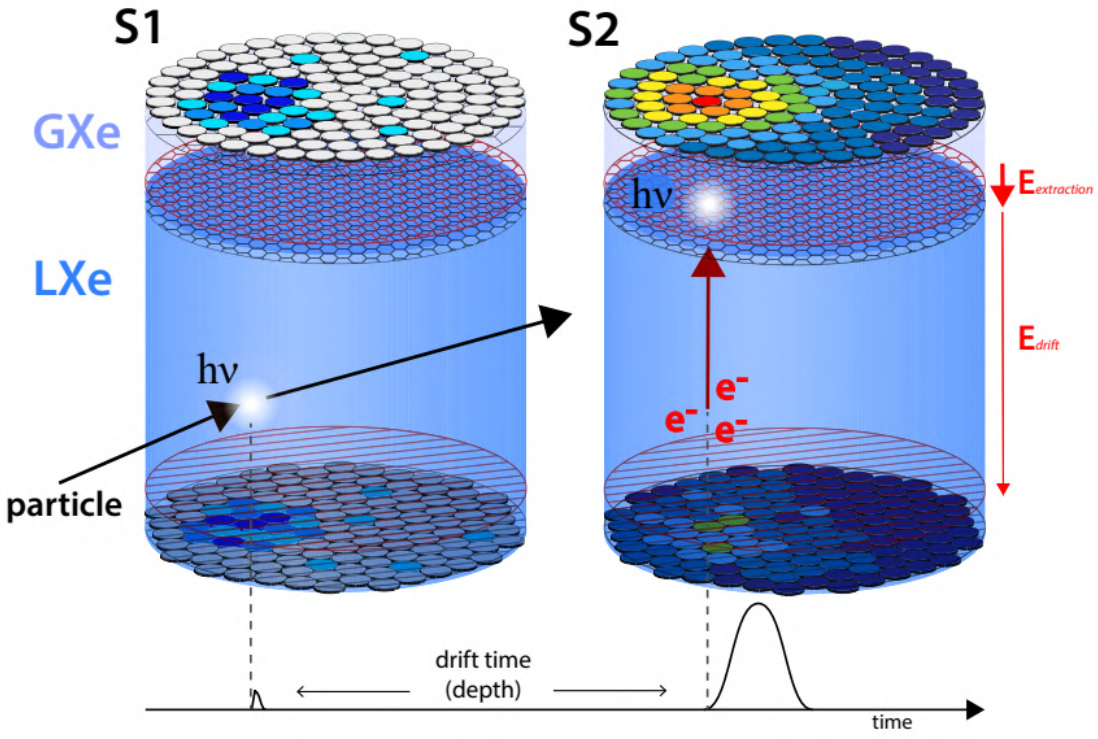

Figure 2.1: Schematic view of a particle interacting in a double-phase Xenon TPC [116]. After the prompt scintillation light produces the S1 signal, the electrons drift towards the liquid/gas interface and are extracted, producing S2. By the xy distribution of the fired PMTs in the top array the xy position of the event is reconstructed. The third coordinate is related to the time delay between the two signals.

position of the event since the light collection efficiency is not in general uniform across the detector; for this purpose one usually makes use of specific calibrations.

The strength of the S2 signal can also be affected by another factor, which is dependent on the z position of the event: while the electrons drift through the liquid Xenon they can be captured by electronegative impurities present in the detector, such as oxygen. This reduces the S2 yield and requires a further correction. To quantify this effect, the *electron lifetime* in LXe is usually defined; it can be increased by means of dedicated purification systems, and monitored with calibrations sources of fixed energy throughout the whole active volume.

2.1.3 Background rejection

One of the most tricky aspects of a direct DM experiment is to be sensitive to an extremely rare signal which is expected to occur on top of a number of background

events. Understanding, simulating and reducing the background sources is therefore of primary importance. The most relevant background sources for a WIMP direct search detector are summarized in Table 2.1, where they have been divided by type of radiation, origin, type of interaction, and expected spatial distribution in the LXe volume.

Type of radiation	**Origin**	**Type of interaction**	**Spatial distribution**
γ/β	^{60}Co, ^{40}K, ^{137}Cs, ^{238}U and ^{232}Th decay chains from detector materials	Electronic Recoil	mostly outer layer
	^{136}Xe, ^{85}Kr and ^{222}Rn (decay chain) dissolved in LXe	Electronic Recoil	uniform
n	(α, n) and spontaneous fission from detector materials	Nuclear Recoil	mostly outer layer
	induced by muons	Nuclear Recoil	mostly outer layer
ν	solar	Electronic Recoil	uniform
	solar, atmospheric and from Supernovae	Nuclear Recoil	uniform

Table 2.1: Background sources of a typical Dark Matter experiment. They come from detector materials, intrinsic impurities, and external sources.

Radioactive elements in the detector materials and in the experimental environment are a relevant source of background. The first action in order to reduce them is taken during the early phase of the experiment when a dedicated radioassay campaign must be performed. All the components must be selected with very low radioactivity. Indeed, decay products of ^{238}U and ^{232}Th are easily found even if in small quantities. Traces of the ^{40}K isotope are instead often present in the PMTs. γ and β radiations scatter on the shell electrons of the Xenon atoms, producing an ER event. Double-phase TPCs are powerful in distinguishing this kind of event from an NR one, as it has been introduced in Section 1.4.3. The kinetic energy gained by an electron or a nucleus after scattering is released in part via scintillation light and in part via ionization of the Xenon atoms. Some of the produced electron-ion pairs recombine; by the process described in (2.2), scintillation photons are then emitted and contribute to S1. Only a fraction of the electrons separated by the atoms, the ones which do not recombine, are drifted by the

electric field and produce S2. Since a nucleus has a greater Linear Energy Transfer (LET), they travel a shorter path in LXe; hence, the electron-ion pairs have a higher chance to recombine. For this reason, Nuclear Recoil events produce a smaller S2/S1 ratio. The variable $log_{10}\,(S2/S1)$ is usually used for the ER/NR discrimination; two well-separated bands are visible in the energy-$log_{10}\,(S2/S1)$ space. The events produced by the detector materials can be isolated also taking advantage of their spatial position in the liquid volume. They are expected to scatter mainly in the outer parts of the detector, near the surfaces of the TPC. Thanks to the 3D position reconstruction achieved in double-phase TPCs it is possible to define an internal *fiducial volume* where the materials and environmental backgrounds are suppressed; when searching for WIMPs, all the events that occur outside the fiducial volume are removed. In Figure 2.2 are shown the ER and NR bands coming from calibration data of XENON10 and the positions of their science data events with the fiducial volume defined for the analysis.

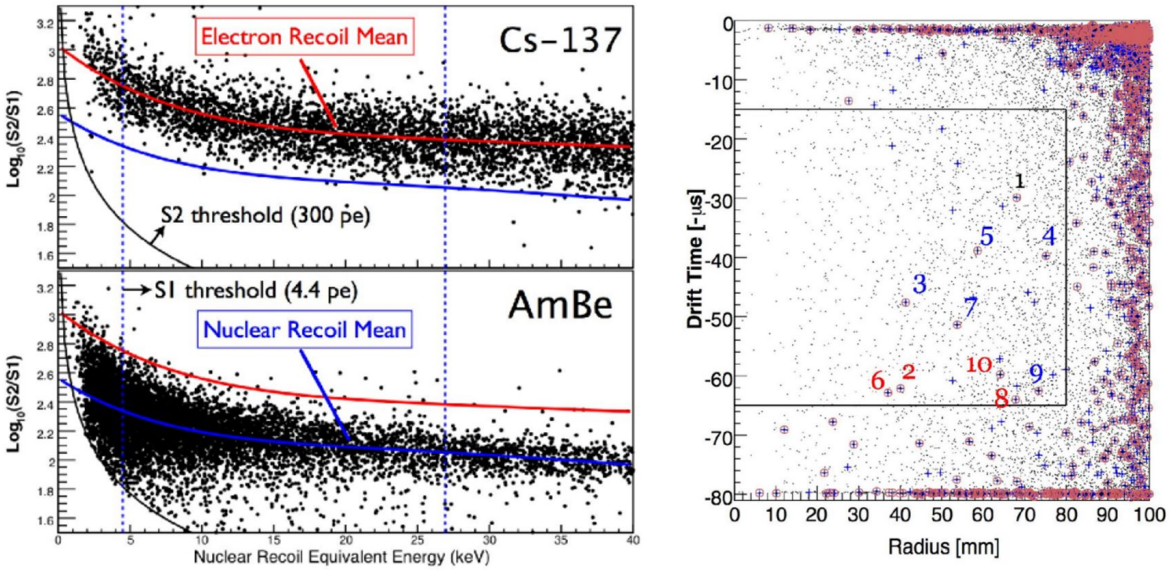

Figure 2.2: Left: XENON10 calibration data from ^{137}Cs γ-rays (producing ER) and AmBe neutrons (producing NR) in the energy vs $log_{10}\,(S2/S1)$ space. The separation between the two populations is a strong tool to reject the ER background. Right: event positions for the first WIMP search science run of XENON10; the fiducial volume is represented by the black line. From [117].

Not all the background sources can be mitigated by the technique explained above. Small quantities of impurities dissolved in Xenon can produce events that are uniformly distributed across the TPC and thus cannot be rejected by fiducialization. These impurities are mainly other noble elements as Kr and Rn with dangerous radioactive isotopes. The β emitter ^{85}Kr has an half life of $\simeq$ 10.76 years and contribute to the ER background.

^{222}Rn can be emanated by detector materials and, with a half life of $\simeq$ 3.8 days, has dangerous decay products as ^{214}Pb which can $\beta-$decay into ^{214}Bi. These Electronic Recoil backgrounds can leak toward the NR band due to statistical fluctuations and must be minimized. Dedicated purification systems are usually employed for this purpose, including cryogenic distillation, where the LXe and GXe are circulated and depleted in the undesired traces of other noble gases.

In deep underground laboratories the flux of muons produced by cosmic rays in the atmosphere is not negligible, even though orders of magnitude lower than on the surface. This background is not dangerous for DM search, since muons release much more energy and cannot be confused with WIMPs. However, they can lead to secondary emissions (as neutrons, as will be explained later) and are usually mitigated with veto systems, which effectively act as active detectors.

One of the most dangerous background is constituted by neutrons, since their signature can mimic a WIMP interaction. They can originate from muon-induces processes (as spallation on the surrounding materials) and more frequently from spontaneous fission (SF) or (α, n) reactions occurring in detector materials. Neutrons are electrically neutral and massive, so they necessarily produce a Nuclear Recoil; since they come from outside the detector their interaction is more frequent toward the surfaces, but not as strongly as with β or γ emission, since the cross sections involved are smaller. This background can be only partly mitigated by the fiducial volume cut and not at all by the $log_{10}\,(S2/S1)$ one. Another way to reduce the neutron background is distinguish between Single Scatter (SS) and Multiple Scatter (MS) events. While WIMPs are expected to only interact ones in the TPC, neutrons can produce more than one scatter. Cutting the MS events (which are characterized by a single S1 and two S2 signals) can thus reduce the neutron background. Another important way to significantly reduce the impact of neutron background is using a dedicated veto system able to tag neutrons. A Neutron Veto system has been built on this purpose in XENONnT: it is the main subject of this thesis, and will be described in more details in Section 2.3.

Neutrinos coming from different sources are another source of background for DM search. Due to their extremely low interaction cross section, the spatial distribution of the interactions in the target is uniform. In case of neutrinos from the Sun, which mostly come from the *pp* chain, they mainly interact with LXe electrons and the ER rejection can be applied. However, higher energy solar neutrinos such as those from ^{8}B decay, together with atmospheric neutrinos and Diffuse Supernovae Neutrinos (DSN), can also scatter off nuclei and produce a NR event. This interaction is known as Coherent Elastic neutrino-Nucleus Scattering (CEνNS) and has been observed by the COHERENT collaboration only recently [118]. When the direct DM detection experiments will reach higher sensitivities in the coming years, they will start exploring a region of WIMP interaction cross section where the irreducible CEνNS background will be dominant, and the sensitivity to discover WIMPs in that region will drop. This effect is known as *neutrino floor* or more optimistically as *neutrino fog* [119]. In Figure 2.3 an estimation

of the neutrino floor/fog is shown, compared to exclusion limits on WIMP-nucleon SI cross section.

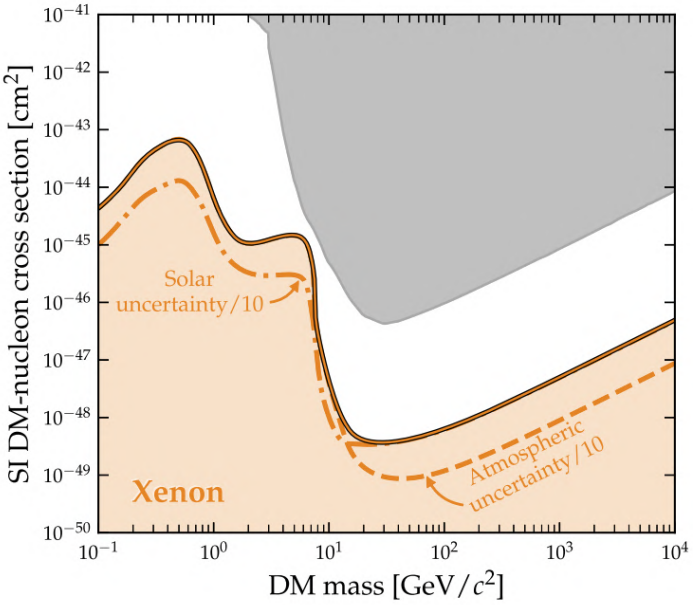

Figure 2.3: Grey: best exclusion limits in the mass-cross section space up to 2021 (found by XENON1T); orange: neutrino floor for Xenon detectors. The dashed lines refer to possible improvements in the neutrino flux uncertainties. From [119].

Another fictitious source of background in double-phase TPCs comes from the accidental coincidences (AC). When two lone signals (single S1 or single S2) happen within a relatively small[2] time window a fake event is recorded. This background can be reduced applying a stronger drift field: this decreases the drift time of the electrons and the probability of an accidental coincidence.

All the above-mentioned techniques for background reduction are powerful but not sufficient. Precise and detailed background models are needed to predict the sensitivity of an experiment and to infer exclusion limits or discovery significance. Full Monte Carlo (MC) simulations are often employed for the background predictions.

2.2 XENONnT

XENONnT is the current phase of the XENON project, started in 2005 with XENON10. Strong upgrades have been made in the years from all points of view, increasing the target

[2]The coincidence time window is usually taken as the maximum drift time of the electrons from the bottom to the top of the TPC.

mass (from tens of kg to ton-scales) and at the same time suppressing all the background sources by orders of magnitude. This led to a parallel growth in sensitivity, reaching nowadays one of the world leading one with XENONnT, as projected by dedicated studies [104].

2.2.1 The XENON project

XENON10

XENON10 has been the first Xenon double-phase TPC prototype of the XENON project; it consisted in a target mass of 15 kg of liquid Xenon. Its main purpose was to prove the feasibility of this technology and test the properties of Xenon as target prior to building bigger detectors of 100 kg-scale and even ton-scale.

The first results of XENON10 come from a period of 58.6 days of data acquired from October 2006 to February 2007 [117]; the analysis was performed in a *blind* way: all the events in the region of interest were analysed only after all the cuts had been defined and tested. This approach became a standard in all the later analyses of the XENON Collaboration and WIMP search in general. The fiducial volume used for this science run had a mass of 5.4 kg. The light signals were collected by two arrays of 41 (bottom) and 48 (top) Hamamatsu R8520-06-Al PMTs. The drift field applied to the LXe was 0.73 kV/cm. Calibration sources have been used to prove the discrimination between ER and NR using the S2/S1 ratio.

The analysis was performed in a region of interest between 4.5 and 26.9 keV. The results led to no excess over then known backgrounds, with new exclusion limits on the WIMP-nucleon SI cross section (the world record at the time) of about $8.8 \cdot 10^{-44}\,\mathrm{cm}^2$ for $100\,\mathrm{GeV/c}^2$ WIMPs mass at 90 % confidence level. The same data set has been used to perform a SD interaction analysis, again leading to an exclusion limit [120]. Another analysis at higher energies, up to 75 keV, led to the exclusion of a previously allowed region for the WIMP-nucleon inelastic scattering cross section [121].

XENON100

XENON100 [122], started in 2009 and hosted at LNGS as well, was the upgrade of XENON10. It contained a total amount of 161 kg of liquid Xenon, among which 99 kg were used as active veto. The number of PMTs in the top and bottom arrays were increased as well, respectively 98 and 80. 64 additional PMTs were employed for the external LXe active veto. The drift field was kept at 0.53 kV/cm in stable conditions. The obtained extraction field was instead $\simeq$ 12 kV/cm. The LXe purification system was improved, reaching a concentration of electronegative impurities below 1 part per billion (ppb). The amount of ^{85}Kr was reduced using a cryogenic distillation column which allowed to reach the impressive concentration of $\simeq$ 150 ppt [122].

XENON100 produced important results in different fields. The most stringent exclusion limits for WIMP-nucleon SI elastic cross section at the time have been set [123, 124, 125, 126] and important results for SD interactions [127], inelastic WIMP-nucleon scattering [128, 129], axions [112] and and other physics goals have been published as well. Dedicated analyses of the background sources have been also carried out [130, 131, 132].

XENON1T

XENON1T [133] was the first WIMP detector operating above the ton-scale of active Xenon mass. With a goal exposure of 2 ton-years, its sensitivity was predicted to approach the neutrino floor for low-mass WIMPs, starting to approach the sensibility needed to observe ^{8}B neutrino coherent scattering. The detector, placed at LNGS, completed its commissioning phase in 2016 and released its WIMP results in 2017 and 2018 [134].

The TPC hosted 2 tons of active liquid Xenon with a fiducial mass of $\simeq 1$ ton. A total of 248 Hamamatsu R11410-21 PMTs have been used, with 127 photosensors in the top array and 121 in the bottom one. The drift field applied varied among science runs lying around 100 V/cm and the extraction field was $\simeq 10$ kV/cm. The TPC was contained by a double-walled cylindrical stainless-steel cryostat made of low-radioactivity material. In order to purify LXe from electronegative impurities, it was constantly circulating in a purification loop able to provide a high electron lifetime. A cryogenic distillation column [135] was employed to remove the radioactive ^{85}Kr contained in natural Kr. The goal was to reduce the concentration of natural Kripton dissolved in Xenon to < 0.2 ppt; they succeded to operate the column online, during science data acquisition, reaching a Kr concentration of 0.36 ppt [133].

An important upgrade brought by XENON1T was the employment of a separate water Cherenkov *Muon Veto (MV)* system. The cryostat containing the TPC was enclosed in a cylindrical water tank with a diameter of 9.6 m and a height of 10.2 m. 84 Hamamatsu R5912ASSY PMTs (with a diameter of 20.3 cm) were placed on the lateral surfaces of the water tank disposed on 2 rings made of 24 PMTs and 3 rings made of 12 PMTs each, detecting the Cherenkov photons emitted by muons and muon-induced shower particles. The demineralized water contained in the tank, working as a passive shield against environmental radioactivity (gamma and neutrons) and as an active target for muons, had a mass of $\simeq 700$ tons and was continuously purified to enhance the water transparency for visible and UV light. Moreover, the inner surfaces were covered by highly-reflective foils with a measured reflectivity greater than 99 % for wavelengths between 400 nm and 1000 nm and acting also as wavelength shifter (WLS) for photons in the 250 nm - 390 nm range, shifting them to higher wavelengths which better match the PMT quantum efficiency [136].

XENON1T was able to decrease by almost two orders of magnitude the accessible

region of WIMP cross section. In addition to an increased target mass and exposure, the key ingredient for that was the huge background reduction achieved thanks to the new muon veto system [137], the ^{85}Kr distillation column [135], the careful choice of low-radioactivity materials for the construction [138] and a dedicated background modelization [139, 140]. It produced important results for the WIMP search, finding no excess of events and setting the most stringent exclusion limits at the time [134, 141, 142], with the minimum exclusion limit of $4.1 \cdot 10^{-47}\,\mathrm{cm}^2$ at a WIMP mass of $30\,\mathrm{GeV/c}^2$ (at 90 % confidence level), as shown in Figure 2.4. The sensitivity of XENON1T was not enough to detect CEνNS of neutrinos from solar ^{8}B [143] but allowed to see the double electron capture of the ^{124}Xe isotope [144], measuring a half life for this process of $1.8 \cdot 10^{22}$ years with $4.4\,\sigma$ significance.

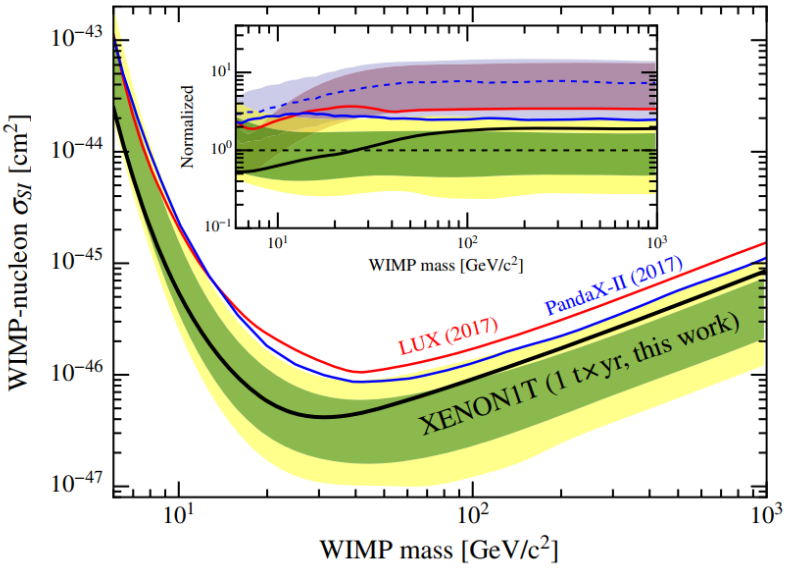

Figure 2.4: Exclusion limit for the SI WIMP-nucleon elastic cross section with 1 ton-year exposure of XENON1T [134], compared with other experiments. The one provided by XENON1T was the most stringent limit at the moment.

An interesting analysis on the low-energy ER events published in 2020 on 0.65 ton-years exposure data resulted in an excess of events in the energy range between 2 keV and 3 keV [52]. The significance of the excess in the reference region 1 keV - 7 keV was $3.3\,\sigma$. Figure 2.5 reports the event rate as a function of energy, where a peak is visible at very low energies.

Different explanations are possible for this excess. From one side solar axions, enhanced neutrino magnetic moment and bosonic Dark Matter could explain it with respective significances of $3.4\,\sigma$, $3.2\,\sigma$ and $3.0\,\sigma$. Each of them would constitute important physics discoveries, in contrast with the current stellar models. On the other side, an un-

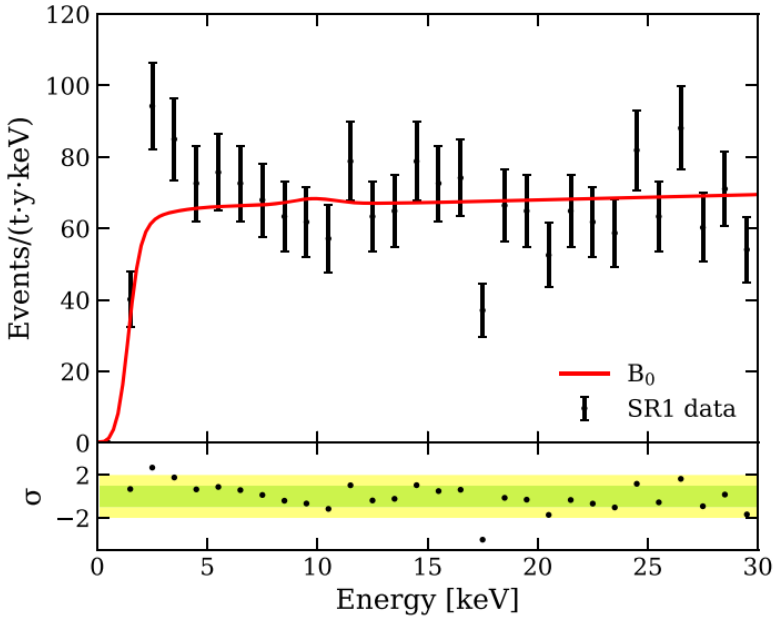

Figure 2.5: Event rate histograms of the low-energy ER made on 0.65 ton-years data of XENON1T [52]. At low energy, the observed event rates (black dots and bars) are significantly higher than expected by the background-only hypothesis (red line). The significance of the excess in the 1 keV - 7 keV energy range is $3.3\,\sigma$.

expected presence of tritium with a concentration of $(6.2 \pm 2.0) \cdot 10^{-25}$ mol/mol in Xenon would also explain the result, with a $3.2\,\sigma$ significance. XENONnT, the successor and upgrade of XENON1T, performed a similar analysis with a ~ 5 times lower background and particular attention to tritium mitigation during the construction phase: it observed no excess in low-energy ER events suggesting that the XENON1T excess is likely due to tritium instead of new physics [53].

2.2.2 Upgrade to XENONnT

XENONnT is the direct successor of XENON1T, from which it inherits many systems and infrastructures. With ~ 3 times more target mass with respect to XENON1T and lower background, it is designed to improve its sensitivity exploring a region of WIMP-nucleon SI elastic cross section more than one order of magnitude lower [104]. It was installed and commissioned at LNGS (in the same water tank of XENON1T) in 2020, started acquiring science data in 2021 and is currently operating.

TPC and cryostat

The cryostat contains 8.5 tons of LXe among which 5.9 tons in the TPC active region and $\simeq$ 4.5 tons in the fiducial volume. The top array is instrumented with 253 3" Hamamatsu R11410-21 low-background PMTs and the bottom one with 241 PMTs of the same kind. Pictures of top and bottom arrays during the assembly are shown in Figure 2.6 (left). The TPC is enclosed in a double-walled stainless-steel cryostat, keeping Xenon at a temperature of -96°C. The inner walls of the TPC are covered by PTFE to enhance the reflectivity for VUV light.

Five electrodes made of stainless-steel wires are used to apply the needed electric fields inside the TPC. The anode and gate electrodes are positioned 3.0 mm above and 5.0 mm below the liquid/gas interface. Perpendicular wires are also present close to them to minimize the sagging effects. The cathode is placed at the bottom of the TPC and two additional electrodes, *top screen* and *bottom screen*, are placed above the anode and below the cathode respectively, protecting the PMTs from high electric fields. The designed drift field was of 191 V/cm but during the commissioning, in November 2020 a short circuit happened between the cathode and the bottom screen, limiting the cathode voltage. The obtained drift field is $\simeq$ 23 V/cm (and the relative extraction field is $\simeq$ 2.9 kV/cm); this turned out to be enough to get operate the TPC for science data.

A rendering of the TPC and the cryostat, including PMTs and electrodes is shown in Figure 2.6 (right).

Veto systems

In addition to the already existing Muon Veto, inherited by XENON1T, a second veto system called *Neutron Veto (NV)* was one of the most relevant upgrades of XENONnT. Placed around the TPC and inside the water tank, it is designed as a Gadolinium-doped water Cherenkov detector, able to detect and tag neutrons in time coincidence with the TPC, to reduce the neutron background. With a octagonal prism shape all around the cryostat, it is instrumented with 120 8" Hamamatsu R5912-100-10 low-background PMTs to detect Cherenkov photons. All the surfaces of the NV are covered with expanded PTFE (ePTFE) panels to enhance the reflectivity. The details about the XENONnT Neutron Veto will be given in Section 2.3.

Xenon handling and storage

The Xenon cooling system is very similar to the one of XENON1T. It is based on the 'remote cooling' concept: it employs a 6 m long vacuum-insulated cryogenic pipe connecting the cryostat to an external cooling station. In case of short term power failure the pressure is maintained within the acceptable range with a battery-powered backup LN_2 cooling system.

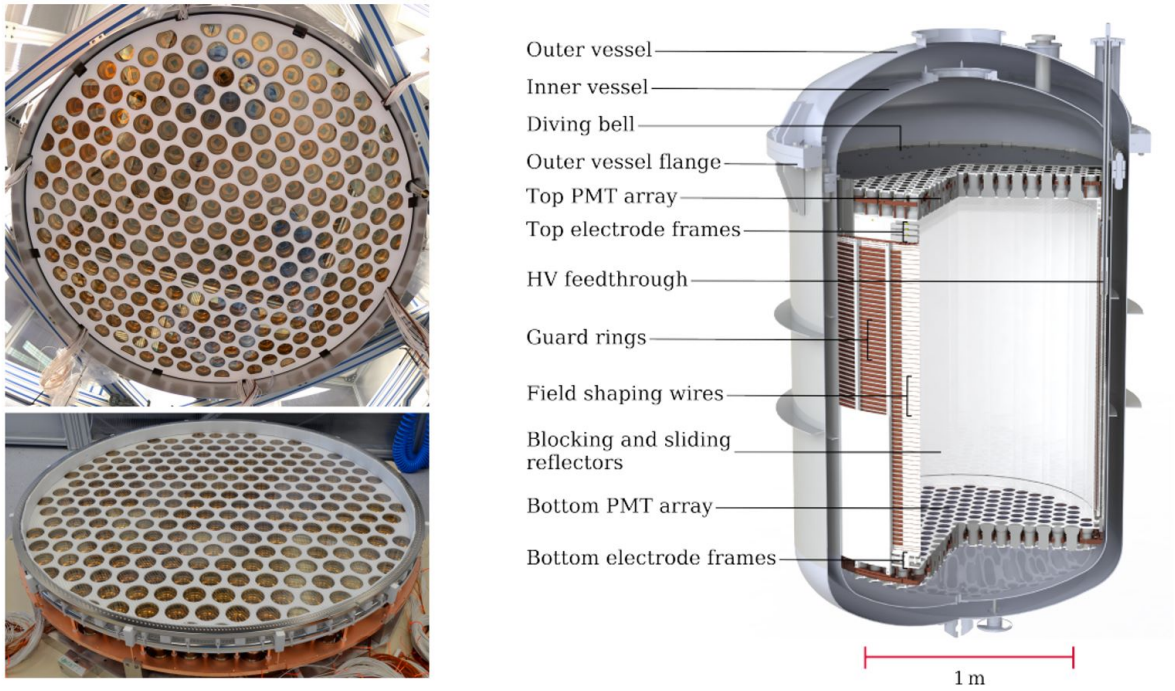

Figure 2.6: Left: pictures of the top and bottom PMT arrays taken during the assembly of the TPC. Right: CAD rendering of the XENONnT TPC and cryostat from [104].

In order to store Xenon in case its quick removal from the cryostat is necessary, two units called *ReStoX*1 and *ReStoX*2 are present. The first was planned and implemented for XENON1T and allows to store 7.6 tons of Xenon. Since this is not enough for the XENONnT content, ReStoX2 was developed to complement the capability of ReStoX1.

Purification and distillation systems

As already pointed out, electronegative impurities as O_2 and H_2O must be removed from Xenon to keep the electron lifetime high enough. In XENON1T, the liquid Xenon circulated through a dedicated line where it was evaporated and then cleaned by a gaseous purification system, employing getters to remove impurities in gaseous form. XENONnT uses this system, basically unchanged, in addition to a novel liquid purification system. Xenon is sent in liquid form through vacuum-insulated filters with getter pills that removes O_2 and other impurities. This new purification system is able to purify the whole XENONnT LXe inventory to < 0.1 ppb O_2-equivalent in ~ 7 days. The measured electron lifetime is > 10 ms, improving by more than a factor 10 the XENON1T performances.

On the other hand, the removal of radioactive isotopes dissolved in Xenon is essential

to minimize the intrinsic background. XENONnT employs the same Kr distillation column as XENON1T. Gaseous Kr is separated by GXe thanks to its higher vapor pressure. In addition to an initial offline distillation, Kr was removed in an online way for 3 weeks. The two distillations allowed to decrease the natural Kripton concentration by almost one order of magnitude with respect to XENON1T, reaching $\simeq 0.05$ ppt. This process is also capable to remove a hypothetical tritium content, under the HT molecular form. This is particularly important to investigate the low-energy ER excess found by XENON1T, cited in Section 2.2.1.

In order to mitigate the ER background caused by Radon emanation, a completely new Rn online removal plant has been developed for XENONnT. It is capable to independently distill Xenon in gaseous and liquid phase. In order to match the ^{222}Rn lifetime ($\sim$ 5.5 days) Xenon from the TPC circulates at 1.7 t/day. The Rn level goal is $< 1\,\mu$Bq/kg; thanks to an intensive material selection the initial level was already very low ($\sim 4\,\mu$Bq/kg) and during the first science run the distillation column worked in GXe only and achieved a level of $1.7\,\mu$Bq/kg; the addition of the LXe circulation should provide another factor 2 of reduction.

Calibrations

Several calibrations are employed to check the response of the detector to different kinds of event. Some calibrations are performed with diffuse sources inside the TPC, directly injecting radioactive gases:

- ^{83m}*Kr calibration*: ^{83m}Kr is a metastable isotope emitting two monoenergetic γ lines at 9.4 keV and 32.2 keV. Thank to its short half life of about 1.83 hours, it is uniformly injected inside the TPC every $\sim$ two weeks even during the science runs, to monitor the spatial response and the electron lifetime;
- ^{220}*Rn calibration*: it emits a broad β spectrum used to calibrate the ER events, and their separation from the NR band. It is usually used before and after each science run;
- ^{37}*Ar calibration*: ^{37}Ar produces two γ lines at 0.27 keV and 2.8 keV, particularly useful to see the response to very low-energy ER events, close to the detector threshold. Due to its 35 days of half life, it can only be performed at the end of a science run and followed by a dedicated distillation procedure through the Kr-column.

In Figure 2.7 (left) calibration data of ^{220}Rn and ^{37}Ar used for low-energy ER analysis of XENONnT science run 0 are shown.

In addition to these internal calibrations, three hardware systems have been built to allow external sources to be placed close to the detector to calibrate both the TPC and the Neutron Veto. These are:

- an *I-belt*: vertically crossing the NV, reaching close to the TPC, has been used to host a ^{88}YBe source, which can be kept at different heights and can calibrate the TPC for low-energy NR events (as the one expected for ^{8}B solar neutrino CEνNS);
- two *U-tubes*: stainless-steel tubes that run around the cryostat. They have been used to calibrate both the TPC and the NV with high-energy γ sources as ^{228}Th as well as the neutron source ^{241}AmBe;
- an *L-shaped beam pipe*: designed to provide a collimated beam of neutrons.

In Figure 2.7 (right) the systems for external sources calibrations are represented.

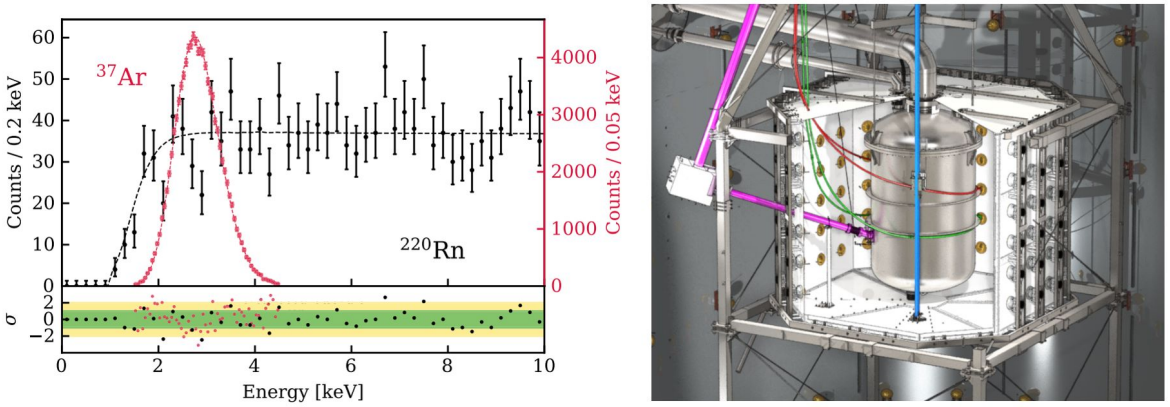

Figure 2.7: Left: ^{220}Rn (black) and ^{37}Ar (red) calibration data for science run 0 of XENONnT. While Rn provides a broad spectrum capable to calibrate the whole low-energy ER range, the Ar peak is useful to correctly model the detector response at very low energies. From the XENONnT first low-energy ER study [53]. Right: CAD rendering representing the Neutron Veto and Muon Veto systems around the central cryostat hosting the TPC, together with the building components. The external calibration lines are shown: I-belt (blue), U-tubes (green, red) and L-shaped beam pipe (pink).

Other calibrations are weekly performed to check the optical performances of the TPC and of the veto systems. Low-intensity light pulse LED sources are placed close to each PMT of the TPC, Muon Veto and Neutron Veto; they are used to monitor single PMT performances as gain, afterpulses and noise. Other light sources as diffuser balls and lasers are used in the MV and NV to check global properties of the detector. The optical properties of the Neutron Veto are measured by a dedicated calibration system called *Reflectivity Monitor*, which will be described in details in Chapter 3.

Slow Control, DAQ and computing

To constantly monitor and control all the subsystems a Slow Control system is employed, featuring Programmable Automation Controllers (PACs) as control hardware and Cimplicity SCADA as software. It consists in the Slow Control system used for XENON1T integrated with the handling of the novel subsystems of XENONnT. The most relevant parameters of the detector are stored in a Proficy Historian database and linked to alarm conditions triggered in case of anomalous states.

Concerning data acquisition, the signals coming from the 494 PMTs present in the TPC are amplified by dual-gain amplifiers and then digitized by CAEN V1724 modules operating at a rate of 100 MHz. The PMTs of the Neutron Veto are instead digitized by CAEN V1730 modules at 500 MHz, without any additional amplification. CAEN V1724 100 MHz digitizers are used for the Muon Veto. All the digitizers of the TPC, NV and MV use a clock module that delivers GPS-time stamped signals. This ensures that all individual channels are time synchronized. All the data is collected in trigger-less mode[3], without a global trigger logic.

All the data produced by the digitizers are processed online by the python-based softwares Strax and Straxen. The raw data consist in fragments of waveforms of the different channels. With multiple steps, event reconstruction is performed reaching progressively higher-level data, then processed and stored in a distributed grid. After a temporary storage at the local LNGS servers, they are transferred to remote storage units sited in Europe and in the USA. A copy of raw data is stored on tapes at CNAF, in Italy.

Physics goals

XENONnT, with its increased Xenon mass and lower background than XENON1T, after reaching a large enough exposure will be much more sensitive to several research channels. The main target is the search for the direct detection of WIMPs. Spin Independent WIMP-nucleon elastic scattering is the favourite process, but inelastic scattering and Spin Dependent scattering are also available channels. Besides WIMPs, rare decays as 2νECEC of ^{124}Xe and $0\nu\beta\beta$ of ^{136}Xe [114] are pursued. CEνNS from ^{8}B solar neutrinos is another ambitious goal.

In light of the results obtained by XENON1T in the low-energy ER events analysis, applying a similar analysis to XENONnT is particularly interesting in order to possibly have an explanation of the observed excess. The first physics result published by XENONnT [53] is indeed referred to this topic. Looking at the same energy range with a larger exposure (1.16 ton-years vs 0.65 ton-years) and ~ 5 times lower background (the smallest ever achieved by this kind of detectors) no excess has been found (see Figure 2.8).

[3]With the exception of LED calibration data.

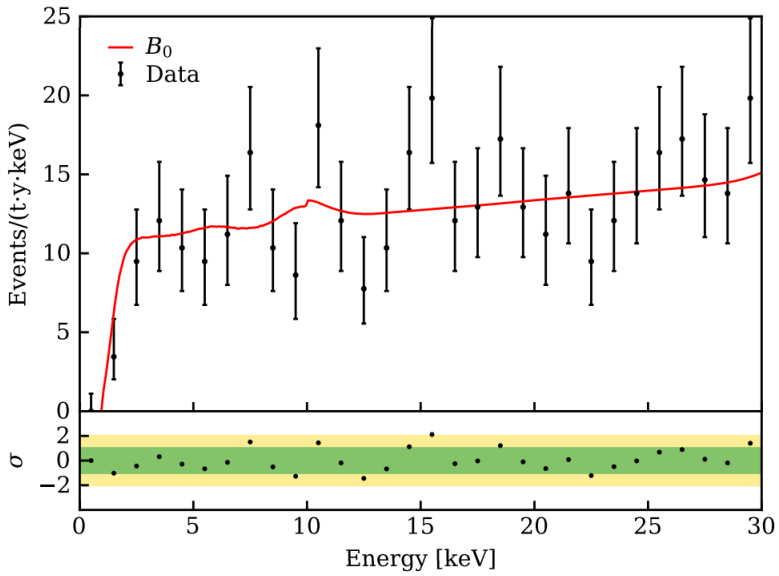

Figure 2.8: Low-energy Electron Recoil event rates for 1.16 ton-years exposure of XENONnT [53]. No excess at low energies is observed.

Since the presence of tritium was a possible explanation for the XENON1T excess, two weeks of tritium-enhanced data has been taken in XENONnT right at the end of the science run used for the low-energy ER analysis. Bypassing the getter of the GXe purifier, the hypothetical amount of tritium in the detector would increase by a factor > 10. Since no trace of tritium decay has been found in those data, it was not included in the background model. Given these results, the most likely hypothesis for the XENON1T excess is the presence of tritium rather than a signal of new physics.

2.3 The XENONnT Neutron Veto

In Section 2.1.3 it has been pointed out that neutrons are among the most dangerous background sources for a WIMP experiment, which fiducial volume and Multiple Scatter cuts are only partly able to mitigate. For this reason, an active neutron veto system is one of the most relevant upgrades of XENONnT with respect to XENON1T. After the design and test phase, where Monte Carlo simulations have been run to find the best design and all 120 PMTs have been tested, the system was installed during Summer 2020.

2.3.1 General description

The XENONnT Neutron Veto consists in an octagonal prism-shaped Gadolinium-doped water Cherenkov detector, placed around the cryostat, inside the water tank which acts as muon veto. It is instrumented with 120 8" Hamamatsu R5912-100-10 PMTs, chosen for their low radioactivity and high quantum efficiency in the Cherenkov spectrum. The PMTs are disposed in 20 columns with 6 PMTs each, across the lateral surfaces. All the surfaces are covered with ePTFE reflector panels, crucial to obtain the highest possible reflectivity for optical and UV photons. More details on the Neutron Veto design and on the tests performed on the PMTs can be found in [145]. A CAD rendering of the Neutron Veto of XENONnT is shown in Figure 2.9. In Figure 2.10 is instead reported a picture of the inside of the NV as seen from below.

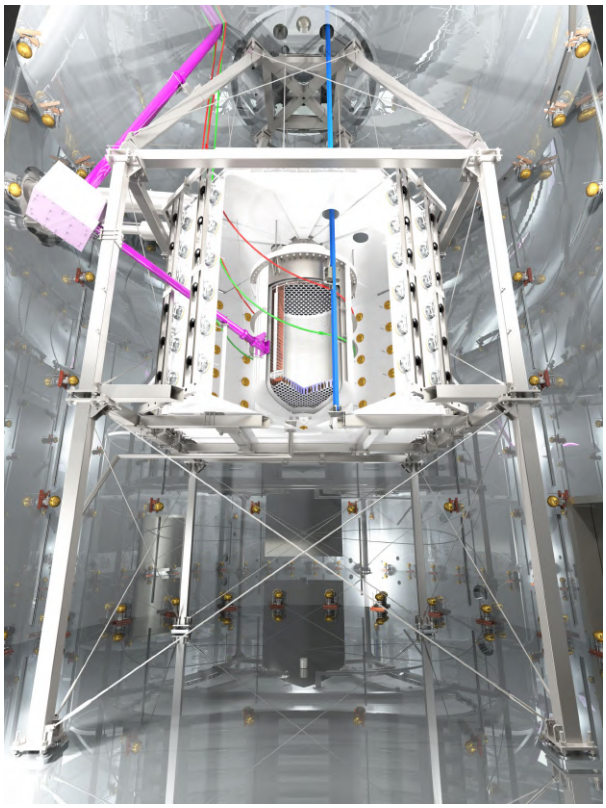

Figure 2.9: CAD rendering of the XENONnT Neutron Veto, placed in between the TPC and the Muon Veto PMTs [104]. In the rendering are highlighted the support structure, the PMTs and the reflector panels of the NV.

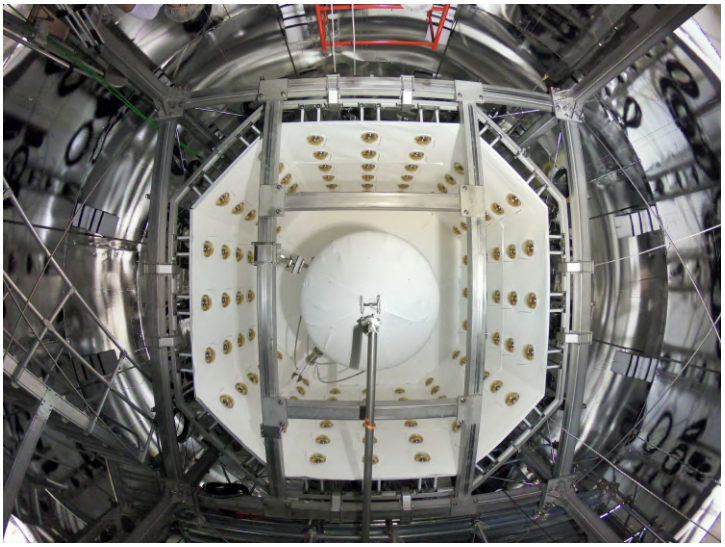

Figure 2.10: Picture of the Neutron Veto inner part from below, taken during the assembling. The cryostat is visible at the centre, also covered with white reflective panels.

Neutron capture and tagging

The working principle of the Neutron Veto relies on the capture of neutrons which can happen on Hydrogen or Gadolinium nuclei after the thermalization in water. The choice of Gadolinium is due to its large neutron capture cross section (further details will be given in Section 2.3.3). After the capture process, the nucleus is left in an excited state and it comes back to the ground state emitting one or more γ-rays with energy of the order of MeV ((n, γ) process). The γ-rays most likely undergo Compton scattering on shell electrons of the water; the recoil energy distribution of the electrons presents a peak in correspondence of the maximal available kinetic energy which is given by [146]

$$E_{max} = E_\gamma \left(\frac{2\gamma}{1 + 2\gamma} \right) \tag{2.3}$$

where γ is defined as $E_\gamma / m_e c^2$. Such peaks are known as *Compton edges*. As shown in Figure 2.11, the electrons have still a $\sim$ MeV energy.

The Cherenkov radiation [147] is emitted anytime a charged particle travels inside a medium with a speed greater than the light speed in that medium. Thus, if the medium has refractive index n, the condition for the Cherenkov emission is

$$v > c/n \,. \tag{2.4}$$

The refractive index of water is $\simeq 1.33$ and the electron mass is $m_e \simeq 0.5\,\mathrm{MeV/c^2}$. The

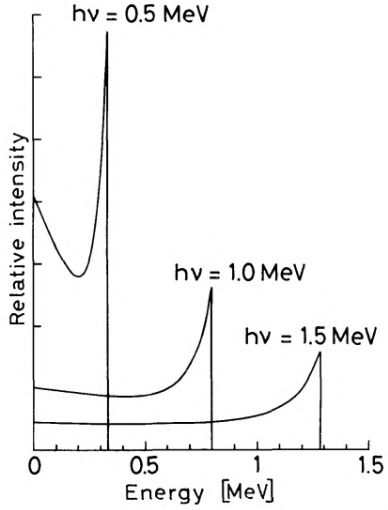

Figure 2.11: Kinetic energy distribution of the recoil electrons after the Compton scattering by gamma rays of different energies [146]. For MeV energy photons, the electrons have $\lesssim$ MeV kinetic energies.

threshold kinetic energy for an electron needed to emit Cherenkov light in water is

$$E_{th} = \frac{m_e c^2}{\sqrt{1-(1/1.33)^2}} - m_e c^2 \sim 0.25\,\text{MeV}\,. \tag{2.5}$$

Hence, $\sim$ MeV electrons produced by the Compton scatterings are above threshold and emit Cherenkov photons.

The Cherenkov photons are emitted along a cone whose axis is coincident with the charged particle trajectory. The angle between the particle path and the emission direction is given by

$$\cos\theta = \frac{c}{n\,(\lambda)\,v} \tag{2.6}$$

(the dependence of n by the wavelength λ has been highlighted). Unlike other experiments as SuperKamiokande that use the Cherenkov light to reconstruct the particle direction, for the Neutron Veto purposes this is not needed. The photon directions are not important as they experience multiple reflections on the surfaces before being detected by the PMTs. The number of photons detected can be used to infer the energy of the primary event, with the help of simulations and dedicated calibrations.

The spectrum of the number of photons emitted per unit path is given by

$$\frac{d^2N}{d\lambda dx} = \frac{2\pi z^2 \alpha}{\lambda^2}\left(1 - \frac{1}{\beta^2 n\,(\lambda)^2}\right)\,, \tag{2.7}$$

where z is the charge of the particle and α the fine structure constant. The spectrum is roughly $\propto 1/\lambda^2$, with the largest emission in the UV range and a tail toward the visible range. The PMTs have to be chosen in order to match as much as possible their Quantum Efficiency (Q.E.) spectra and the Cherenkov spectrum. Since the Q.E. spectra are usually peaked in the optical range, the detected photons will belong to a wavelength range extending from the near UV to the blue light, $\sim 300\,\text{nm} - 550\,\text{nm}$. The number of emitted photons is not very large (of the order of 100 photons/cm), orders of magnitude less than what yielded by scintillator materials.

The Neutron Veto constitutes a further cut to be applied to WIMP data. When a neutron-like event is recorded in the NV, all the events happened inside the TPC in a previous time window are cut away. The duration of the time window and the trigger conditions for the Neutron Veto are parameters that influence the *neutron tagging efficiency*. It can happen, in fact, that a neutron (muon-induced or, more likely, by SF or (α, n) process by the detector materials as the cryostat itself) single scatters inside the fiducial volume of the TPC and is then pushed toward the Neutron Veto. If the latter is able to capture and tag the neutron, the related cut prevents that it is erroneously identified as WIMP.

DAQ and data types

The data coming from the 120 Neutron Veto PMTs are digitized by eight CAEN V1730 modules. The sampling rate is 500 MHz (2 ns per sample) and the input voltage is 2 V with 14-bit resolution: each ADC count represents $\simeq 0.12\,\text{mV}$. Two trigger modes are used. The *self-trigger* mode is used for science and high-level calibration data; when the signal of a single channel overcomes a threshold of 15 ADC counts with respect to its baseline it is recorded, in a time window which starts 32 samples before the trigger and ends 38 samples after (but can be further extended if the signal is longer). The digitized signals of each PMT's *waveform* constitute the raw data. The other trigger mode, called *external-trigger*, is used for the LED calibrations. All the PMT channels signals are recorded starting from a trigger time and for a fixed time window. The length of the time window as well as the trigger rate can vary depending on the requirement of each calibration.

From the raw data emerging by the digitizers a chain of processing starts, producing progressively higher-level data. Each higher-level data type is produced by one or more lower-level data through python codes called *plugins*. The main Neutron Veto data types are:

- `raw_records_nv`: raw data coming from the digitizers. They contain informations about the start and end times of the record, the relative PMT number and its signal as a function of time (waveform);
- `hitlets_nv`: signals found in the PMTs, requiring a coincidence of at least 3 signals

over threshold in a time window of 300 ns. They do not contain the waveform but the computation of the hit *area*, i.e. the estimation of the number of photoelectrons (PE) causing the signal;

- `events_nv`: NV events, defined as all the hits in a $\geqslant 3$ coincidence within a 200 ns time window. The time window can be extended in steps of 200 ns if other hits are found. This data type includes informations on the area of each hit, the relative PMT channel, the number of distinct PMTs inside the event and the *center time*, defined as the area-averaged timings of each hit with respect to the beginning of the event. The latter variable aims to estimate the time extension of the event;

- `event_positions_nv`: they are on the same level of `events_nv`, providing informations on the 3D position of the event in the Neutron Veto. The position is averaged on the hits occurred in the first 20 ns of the event.

Water purification

As outlined above, the Cherenkov emission does not provide a large amount of photons. Thus, a crucial role in the detection efficiency of the Neutron Veto is played by the *wall reflectivity* and by the *water transparency* to optical and UV photons. While the former is enhanced by the use of highly reflective ePFTE panels, the latter requires a continuous purification process.

At a first stage, the Neutron Veto has been run in pure-water mode, with the addition of Gadolinium left to a second phase. Pure water is highly transparent to visible and UV light, with absorption lengths $\gtrsim 100$ m [148]. A dedicated water purification system, called Water Loop Plant (WLP), has been inherited by XENON1T and used in this first phase. Its main purpose is remove ions and bacteria dissolved in water that can cause a decrease of transparency and thus a degradation of the NV optical performances. It is a relatively simple system, with a de-ionizing filter and pressure, flow and resistivity sensors. Resistivity is essential to monitor the amount of ions dissolved in water: pure water exhibits a resistivity at 25°C[4] of about 18.18 MOhm $\cdot$ cm [149]. Further details on the relation between conductivity, transparency and ion content of water solutions will be given in the next chapters.

The WLP cannot be used to purify water when Gadolinium is added to the water, since it will quickly remove Gd ions from the solution. To accomplish this goal, a new purification system called *Gadolinium-Water Purification System (GdWPS)* has been designed; its commissioning is the topic of this thesis and will be detailed in the following chapters.

[4]Resistivity has a strong dependence on the temperature; for this reason, it is usually reported at 25°C.

In order to monitor the optical properties of the Neutron Veto, in terms of reflectivity of the walls and transparency of the water, a calibration system called Reflectivity Monitor has been introduced. It will be detailed in Chapter 3.

2.3.2 First performances with pure water

Even during the first operations with pure water, the Neutron Veto showed already remarkable performances. The neutrons are captured by Hydrogen with the reaction:

$$\mathrm{H} + n \rightarrow {}^{2}\mathrm{H}^{*} \rightarrow {}^{2}\mathrm{H} + \gamma\,(2.2\,\mathrm{MeV})\ . \tag{2.8}$$

The thermal neutron capture cross section of Hydrogen is (0.329 ± 0.004) barn [150]. As seen in (2.8), a single ~ 2.2 MeV photon is emitted in the formation of the Deuterium nucleus. The relative capture time constant in pure water is $\sim 200\,\mu$s.

The performances of the Neutron Veto in this configuration have been tested with a calibration consisting in an AmBe neutron source placed in one of the U-tubes. The AmBe source is very useful; its relies on the α-decay of ^{241}Am followed by an (α, n) process occurred to Be. The full process is [151]:

$$\begin{aligned} {}^{241}\mathrm{Am} &\rightarrow {}^{237}\mathrm{Np} + \alpha \\ {}^{9}\mathrm{Be} + \alpha &\rightarrow {}^{13}\mathrm{C}^{*} \\ {}^{13}\mathrm{C}^{*} &\rightarrow \begin{cases} {}^{12}\mathrm{C} + n \\ {}^{12}\mathrm{C} + n + \gamma \end{cases} \end{aligned} \tag{2.9}$$

The excited state ^{13}C* can de-excite in two ways:

- emitting a neutron with energy up to $\sim 7 - 10$ MeV of kinetic energy;
- emitting a neutron with maximum energy of $\sim 2 - 6$ MeV of kinetic energy and a 4.4 MeV photon.

The photon is thus emitted in coincidence with the neutron, with a probability that is source dependent ($\mathcal{O}\,(50\ \%)$). When it is emitted, it constitutes a strong signature and can be used as a trigger to look for a neutron. In the XENONnT Neutron Veto the AmBe calibration has been performed using 4.4 MeV $\gamma-$rays detected by the TPC as trigger and looking at the NV events in a subsequent time window.

In Figure 2.12 (left) is reported the energy spectrum (in photoelectrons) of the neutron events, after appropriate cuts, of the AmBe calibration. The first two peaks are due, respectively, to neutron capture on Hydrogen (2.2 MeV) and on Carbon (4.4 MeV). The two higher-energy peaks are due to neutron captures on heavier elements (as ^{56}Fe present in the cryostat). In Figure 2.12 (right) the time delay distribution of events in the Neutron Veto with respect to the triggering $\gamma-$ray is shown. The distribution is, as

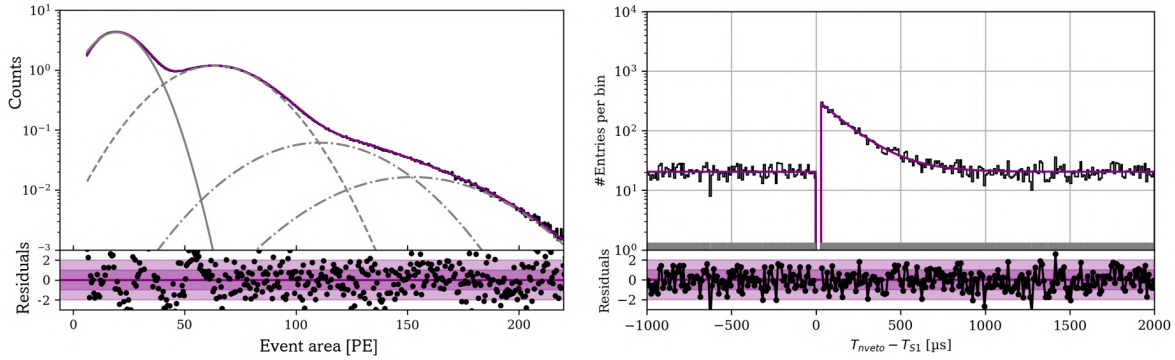

Figure 2.12: Left: energy spectrum of AmBe neutron events detected by the Neutron Veto. The first peak corresponds to the neutron capture by Hydrogen, the second one by Carbon. The 2.2 MeV peak is converted to $\sim$ 20 PE. Right: distribution of the time delays between the 4.4 MeV photon detected by the TPC and the neutron detected by the NV.

expected, exponential; the extracted time constant is 171 μs and provides an estimation of the neutron capture time.

From this calibration it has been possible to estimate the neutron tagging efficiency, i.e. the fraction of neutron that, after being scattered inside the TPC, are correctly identified by the Neutron Veto. It mainly depends on two parameters: the threshold area (in PE) and the coincidence window chosen to apply the cut. Choosing a low threshold and a long time window the tagging efficiency will increase, but that will affect the effective livetime of the experiment because more time will be cut away by the Neutron Veto cut. With a threshold of 5 PE and a 600 μs time window the neutron tagging efficiency has been measured to be 65.6 % $\pm$ 1.3 %, while the livetime loss is 6 %.

2.3.3 The impact of Gadolinium

Gadolinium is the most powerful elements for neutron detection, since it features the highest capture cross section for thermal neutrons, orders of magnitude greater than the Hydrogen one. It is a rare but stable element (two isotopes are very long-living). The most relevant contributions to the cross section come by the isotopes ^{155}Gd and ^{157}Gd. In Table 2.2 are reported the natural isotopes of Gadolinium, with their abundance and capture cross section [152, 153].

After the capture, Gadolinium de-excites emitting 3-4 gammas, with total energy $\sim$ 8 MeV. The advantages of using capture on Gadolinum instead of on Hydrogen are mostly two. First, the greater Q-value of the process guarantees a greater tagging efficiency.

Isotope	Abundance	Cross section [barn]
^{152}Gd	0.2 %	735
^{154}Gd	2.18 %	85
^{155}Gd	14.8 %	60900
^{156}Gd	20.47 %	1.8
^{157}Gd	15.65 %	254000
^{158}Gd	24.84 %	2.2
^{160}Gd	21.86 %	1.4

Table 2.2: Relative abundance and thermal neutron capture cross section of the natural isotopes of Gadolinium.

Furthermore, the neutron capture time in Gd-loaded water is reduces from $\sim 200\,\mu$s to $\sim 30\,\mu$s[5]; this allows to use a shorter coincidence time window for the Neutron Veto cut, losing a smaller fraction of livetime.

Gadolinium will be dissolved in water in the form of Gadolinium sulfate octahydrate salt: $Gd_2(SO_4)_3 \cdot 8H_2O$. In water, it dissolves in divalent ions SO_4^{2-} and trivalent ions Gd^{3+}. This technology has been recently used in the SuperKamiokande experiment [154] after intensive tests at the EGADS facility [155]. The work made by EGADS is particularly useful for the XENONnT Neutron Veto because of the similar mass of water used: 200 tons for EGADS and 700 tons for the NV. The fraction of neutron captures on Gadolinium as a function of its concentration is shown in Figure 2.13.

The goal concentration for the Neutron Veto is 0.2 % of Gd in mass. In this way, more than 95 % of the captures will happen on Gadolinium and the performances will get significantly better. With the help of simulations, it is possible to predict the neutron tagging efficiency of the Neutron Veto with Gd-doped water. In Figure 2.14 is shown the trend of the tagging efficiency for different choices of *N-fold coincidence* (i.e. the number of distinct fired PMTs in coincidence required to trigger an event) and for different Gd-water concentrations: pure water, 0.02 % Gd-water solution and 0.2 % Gd-water solution.

From the plot it is visible that the expected tagging efficiency at 10-fold coincidence with pure water is $\simeq 64$ %, consistent with what found by the AmBe calibration. Inserting the Gd salt and reaching 0.2 % concentration of Gadolinium mass, the expected tagging efficiency with the same trigger conditions is $\simeq 85$ %. The neutron background consists in all the neutrons not vetoed by this cut. The addition of Gadolinium would

[5] At a Gd mass concentration of 0.2 %.

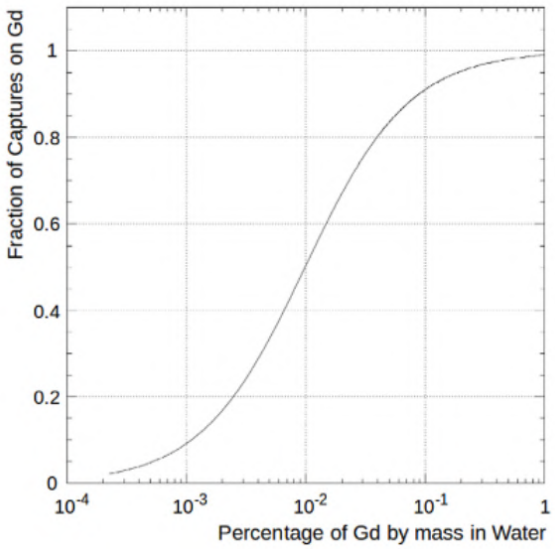

Figure 2.13: Fraction of neutron captures that happen on Gd as a function of Gd mass concentration. At ~ 0.01 % concentration, around half of the captures occur on Gd and half on H. Above 0.1 % concentration, more than 95 % of the captures happen on Gd.

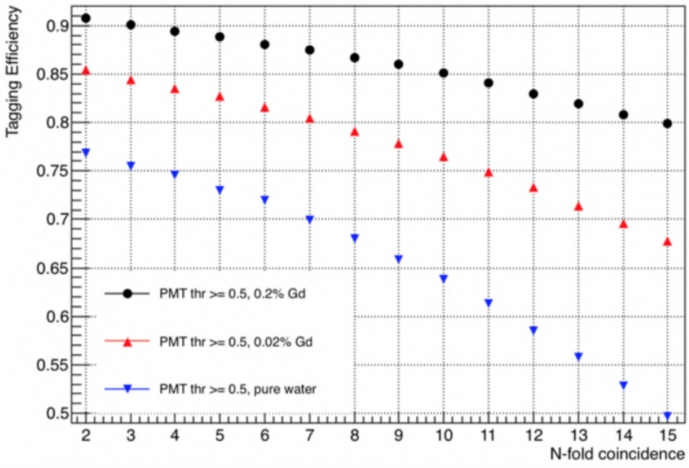

Figure 2.14: Neutron tagging efficiency as a function of N-fold coincidence. Blue triangles: pure water; red triangles: 0.02 % Gd-water solution; black dots: 0.2 % Gd-water solution. At 10-fold coincidence, the tagging efficiency raises from $\simeq 64$ % to $\simeq 85$ %.

then cause the reduction of the un-tagged neutrons from $\simeq 36$ % to $\simeq 15$ %, that leads to a background reduction of a factor ~ 2.4. Adding 0.02 % Gd concentration the effect is already visible, causing an increase of the tagging efficiency to $\simeq 76$ %.

Chapter 3

Neutron Veto Reflectivity Monitor

For a water Cherenkov detector, one of the key ingredients to achieve a high light collection efficiency is maintaining good optical properties. If either the transparency of the water or the reflectivity of the surfaces drop, the performances of the detector degrade. For this reason, it is important to constantly check that the optical properties remain constant or in an acceptable range. The tool used in the XENONnT Neutron Veto for this purpose is a calibration system featuring a laser light source. Running periodically this calibration, it is possible to see if one of the two parameters, transparency or reflectivity, experience a decrease. It gains particular importance in light of the doping of water with Gadolinium, since it may affect the transparency.

3.1 Hardware and data acquisition

The Reflectivity Monitor calibration relies on a laser source emitting a short pulse of UV light. It is able to provide a pulse length of $\sim 50\,\text{ps}$ at a wavelength of 375 nm, in the near UV range. This wavelength has been chosen within the region where most of the photons are detected by the Neutron Veto PMTs. The laser is connected to four quartz optical fibers that guide light until a support placed on one of the lateral walls of the Neutron Veto, at nearly half height. Each optical fiber provides an output channel from which the light is shot; they are labeled with 1, 2, 3 and 4. Channels 1 and 3 direct the light upward while channels 2 and 4 point downward.

In Figure 3.1 (left) a picture and a CAD rendering of the support with the four outputs of the optical fibers are shown; in Figure 3.1 (right) is reported a drawing of one of the lateral surfaces of the NV, with the PMTs and the Reflectivity Monitor support positions.

The Reflectivity Monitor runs are performed separately for each optical fiber channel, selected with an optical switch. The laser is linked to the DAQ and to the trigger system: this is crucial to have a precise time synchronization. The acquisition mode is external-

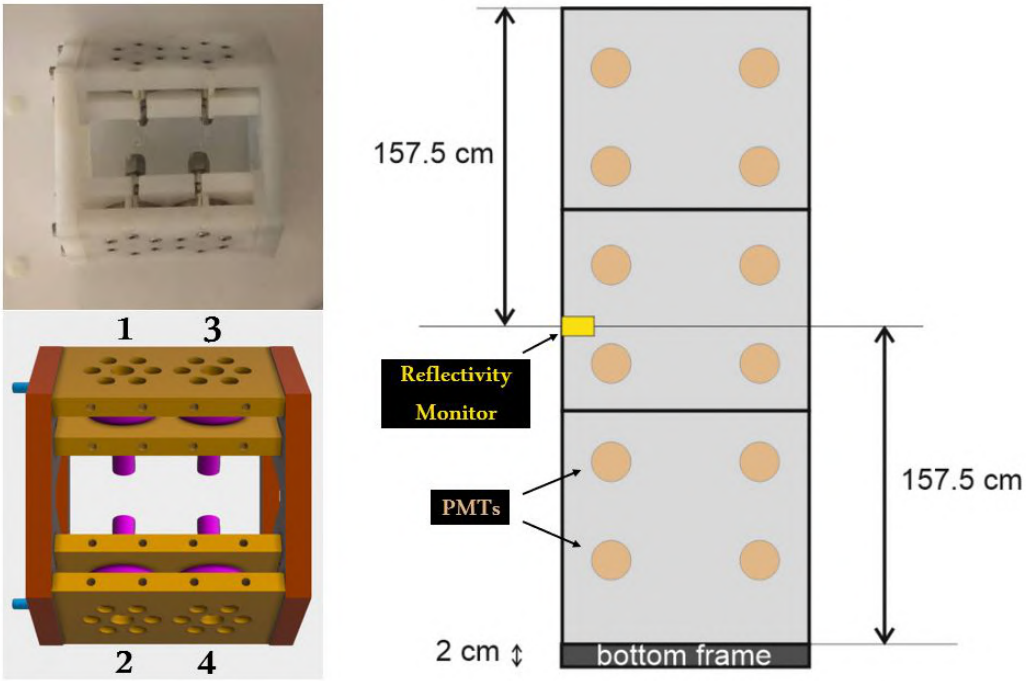

Figure 3.1: Left: picture and CAD rendering of the support element for the Reflectivity Monitor, with the labels of the four channels: channels 1 and 3 look upward while channels 2 and 4 look downward. Right: position of the Reflectivity Monitor support on the later wall of the Neutron Veto, compared to the PMTs positions.

trigger: the trigger signal is sent both to the digitizers and to the laser which emits the light pulse. The digitizers record the data of all the NV PMTs within a fixed time window; this procedure is repeated at a given rate until the end of the run. The trigger rate and the time window length have to be correctly regulated in order to not exceed the data rate supported by the DAQ. In this way, thanks to the fast response of the laser, the light pulse is sent with a fixed time delay with respect to the trigger time, and the latter corresponds to the initial time of each PMT signal[1].

During 2021 the system has been commissioned and tested; several runs have been acquired with different configurations until a stable condition has been found. For the first months of 2022, until the beginning of May, the trigger rate has been kept to 400 Hz with a corresponding time window of 320 samples (640 ns). After that, the time window has been extended to 500 samples (1 μs) and the trigger rate rescaled to 300 Hz. All the runs, with the exception of a few ones for test purposes, lasted 5 minutes.

[1]However, the trigger signal does not reach each digitizer simultaneously. This problem can be easily solved as will be shown in the next Section.

3.2 Data analysis

The goal of the Reflectivity Monitor is to quantify the performances of the Neutron Veto in terms of optical properties by measuring the characteristic time constant of the photons that travel inside the system. If N photons are produced at a time t_0, $N' < N$ of them will be detected by the PMTs. The times after which each photon is detected are distributed accordingly to an exponential with time constant τ. This time constant is affected both by water transparency and by ePTFE reflectivity. At a fixed transparency, a larger reflectivity leads to a larger time constant; at a fixed reflectivity, a larger transparency leads to a larger time constant. By measuring the time constant it is not possible to disentangle these two contributions. However, the efficiency of neutron tagging is directly influenced by the time constant, rather than by either the reflectivity or transparency individually. As a result, monitoring the time constant enables to keep under control the optical performances of the system.

It is possible to get the time constant by the Reflectivity Monitor runs with the following procedure. Considering a run which uses a given optical fiber channel, the data recorded belong to a series of time windows started at each trigger time. For each time window, the `hitlets_nv` data are used: the time delays between the trigger time and each hit's time are calculated and used to build a histogram. All the histograms of each time window are summed up to build an overall timing histogram, which has an exponential shape characterized by a time constant τ. The time of each trigger can be found by looking at the `raw_records_nv` data; not all the PMTs have the same trigger time, since the trigger signal is connected in series to the different boards that host the digitizers (what is called 'daisy chain'). This problem is solved simply extracting the trigger time always by the first PMT that starts acquiring data and using it as time reference.

This procedure has been coded in a plugin that, taking as input `raw_records_nv` and `hitlets_nv`, provides a new data type called `ref_mon_nv`. This latter contains the relevant informations for the Reflectivity Monitor analysis; it consists in a series of hits for which the PMT channel, the area and its time with respect to the previous trigger are stored. The last parameter is the most important, used to build the exponential distributions.

Examples of exponential distributions for different optical fiber channels are shown in Figure 3.2, corresponding to a run acquired on April 29$^{\text{th}}$ 2022.

3.2.1 Preliminary checks

Prior to defining the final procedure for the analysis, some checks on the data have been carried out to better understand the features of this calibration.

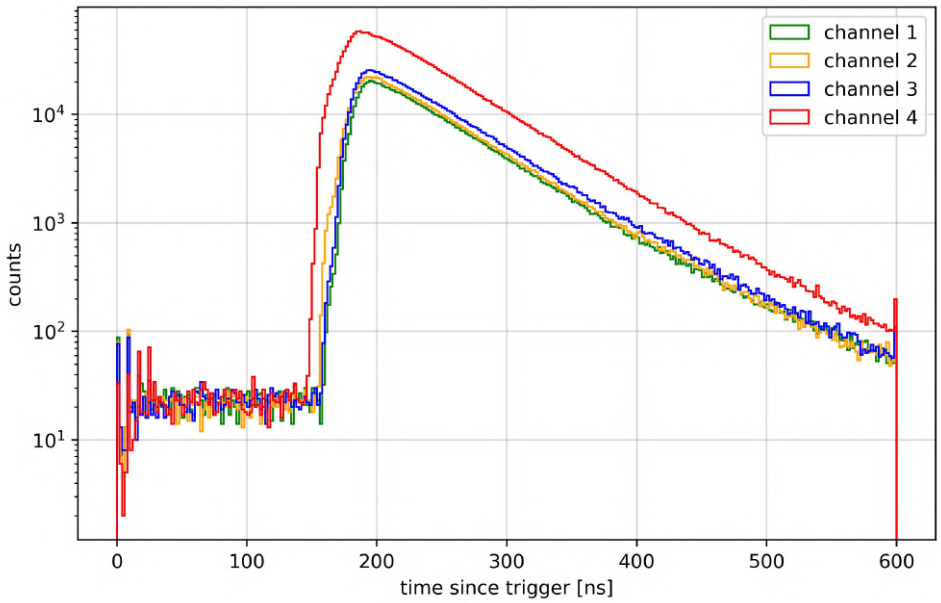

Figure 3.2: Exponential distributions of hit times for the four channels. The main pulse of the laser is detected by the PMTs $\sim$ 200 ns after the trigger, than there is an exponential decay.

Event positions

The `event_positions_nv` data can be used to see the positions of the Reflectivity Monitor events in the Neutron Veto. By the definition of NV event explained in Section 2.3.1 it is clear that the hits recorded within each time window are likely joint into the same event. Since the light is shot from the lateral surface toward the TPC in upward or downward directions depending on the channel, it is expected to be reflected by the ePTFE panels that cover the cryostat and then be detected firstly by the PMTs close to the emission point, the upper or lower ones depending on the optical fiber used. The paths of photons are affected by several random factors: the emission direction, the Rayleigh scattering on water molecules and the diffusion by the ePTFE panels (which shows a Lambertian behaviour).

In Figure 3.3 are shown the event positions for the four channels (reported in cylindrical coordinates). A difference is visible between upward and downward pointing channels. Channel 4 looks different than the others; this difference is not only visible in the event positions but also evident by other parameters, as will be shown later.

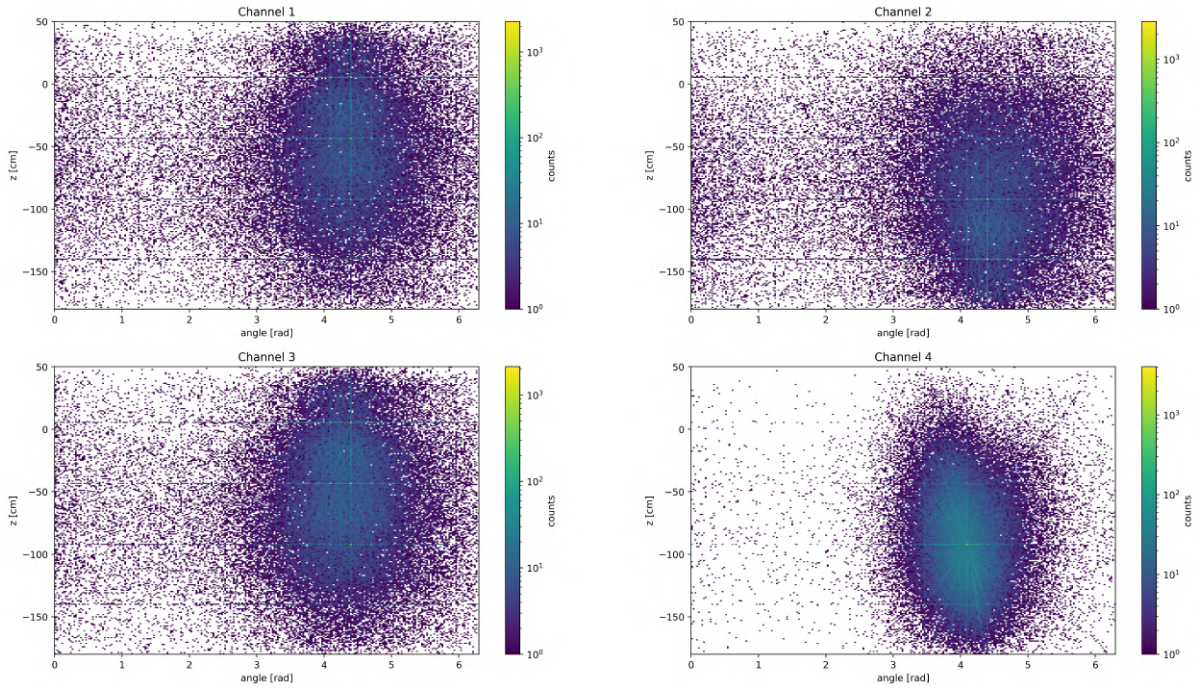

Figure 3.3: Event positions for different optical fiber channels. They are represented in cylindrical coordinates, as a function of the angle around the Neutron Veto and of the z position. Channel 4 shows a more peaked distribution. It is possible to notice a difference between upward looking channels (1 and 3) and downward looking channels (2 and 4).

Cuts

In order to obtain clearer distributions, some cuts have been applied prior to make the exponential fits. On the level of the single hits, in order to get rid of fake signals, a cut on the area has been applied: only the hits with at least 0.3 PE have been kept. This threshold has been chosen to remove most of the unphysical signals but keep the real signals that may experience a negative fluctuation.

On the event level, another cut is applied. Events with a small number of PMTs involved are removed; this cut has been chosen in a different way between channel 4 and the others, due to the different behaviour observed. In Figure 3.4 are indeed shown the distributions of events (again for a 5 minutes run acquired on April 29$^{\text{th}}$ 2022) in terms of number of different PMTs contributing to the event and total area. For channels 1, 2 and 3 only the events with at least 3 PMTs fired have been kept. For channel 4, this threshold has been raised to 7.

These two cuts, on hits and events, guarantee an acceptance greater than 90 %.

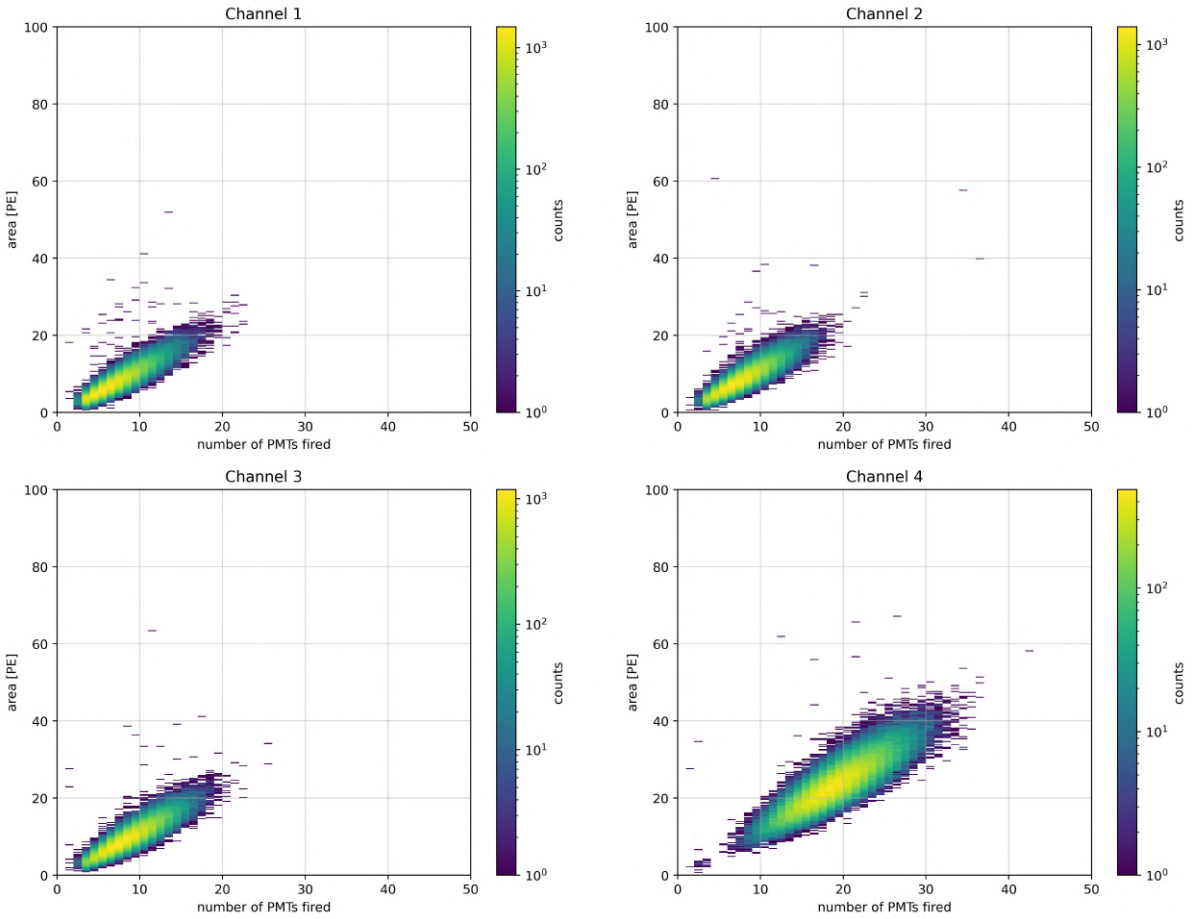

Figure 3.4: Distributions of events, for the four channels, in the number of PMTs vs area space. Channel 4 shows approximately the double of PMTs and area than the other three channels.

3.2.2 Exponential fit and results

To fit the distributions, a least squares fit with 3 parameters has been performed through the *iminuit* python package [156]. The fitting function is

$$f(t) = A\, e^{-t/\tau} + c\,. \tag{3.1}$$

The parameter of interest is the time constant τ; A is a normalization factor; c accounts for the background due to the dark rate of the PMTs and physical events not related to the calibration (both of them uniformly distributed over time). Figure 3.2 shows that the exponential distribution starts $\sim 200\,\text{ns}$ after the reference time, but this time delay is reabsorbed into A and thus does not need to be described with an additional parameter. The three parameters are left free, with the only constraint of keeping c greater than

zero.

The choice of binning for the histogram and the range in which the fit is performed are critical to achieving a successful fit; hence, the number of bins has been chosen, for all the runs, in order to match the timing resolution of the digitizers (2 ns). Concerning the fit range, attempting to fit the entire distribution resulted several times in a bad χ^2 or even failure due to the need for a more sophisticated model to describe it. Nevertheless, since the objective of these fits is solely to extract the time constant of the exponential distribution, the range has been limited, which has led to good fits. Channel 4 showed a better behaviour than the others; for this reason, its fitting range has been kept longer, from 250 ns to 600 ns. The best range for channel 1 and 2 has been identified to be from 260 ns to 450 ns. Channel 3 yielded the worst results, requiring an even shorter range to adequately adapt the model to data. However, using such a short range would lead to high uncertainties and a poor description of the constant component. Thus, the range has been set to the same as channels 1 and 2, even if the goodness-of-fit test was not optimal. As stated in Section 3.1, from the beginning of May 2022 a longer time window has been used for the data acquisition. This was made to attempt a longer range fit and possibly better describe the constant component; however, fitting in a longer range always showed larger χ^2, so the fit range has been maintained equal to the previous ones. This also guarantee consistency between short-window and long-window runs.

In a 5-minutes run, the number of hits generated by channel 1, 2, 3, and 4 is approximately 500 000, 700 000, 800 000, and 2 000 000, respectively. While channel 4 produces significantly more hits, increasing the duration of runs for the other channels did not result in any noticeable improvements. The different behaviour of channels 1, 2 and 3, providing less light than channel 4, might be due to some damage happened to the optical fibers during the installation.

To find the best solutions for the fits, a set of runs acquired between the end of 2021 and July 2022 have been used. They consist in 16 runs for channel 1 and 17 runs for the other three channels. Goodness-of-fit tests have been employed to assess the accuracy of the exponential curve's fit to the data. The p-value distribution can be examined, based on a series of repeatable runs, to determine whether the data are appropriately modeled. If the distribution is uniform, it indicates that the model is correct. Conversely, if there are systematic discrepancies, a clustering of low p-values will be observed [157].

In Figure 3.5 are shown the p-value distributions for the four channels, referring to the fits performed in the range 250 ns − 600 ns for all of them. In Figure 3.6, instead, the fit range for channels 1, 2 and 3 has been restricted to 260 ns − 450 ns. It is clear that, while for channel 4 the fit works well also in a longer range, for the other channels the restriction is necessary to obtain an acceptable goodness-of-fit.

In Figure 3.7, an example of fit for channel 4 for a run acquired on May 13$^{\text{th}}$ is shown.

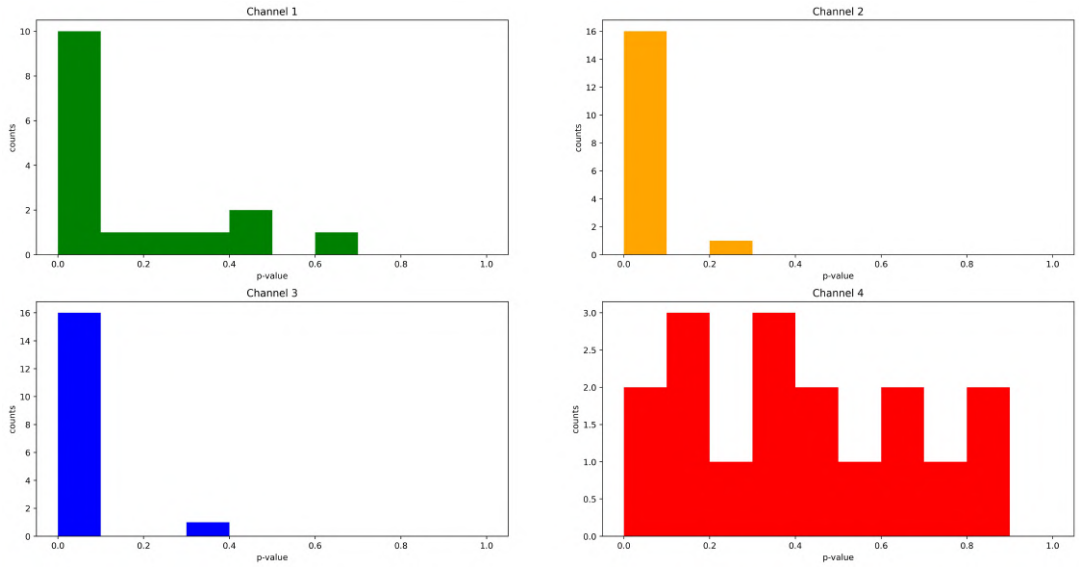

Figure 3.5: p-value distributions for the four channel, referring to the 16 runs of channel 1 and 17 runs of the others used to adjust the fits. The fit range used is 250 ns − 600 ns for all the channels. Channel 4 is the only one which shows a distribution almost uniform: the other three channels have several p-values close to zero.

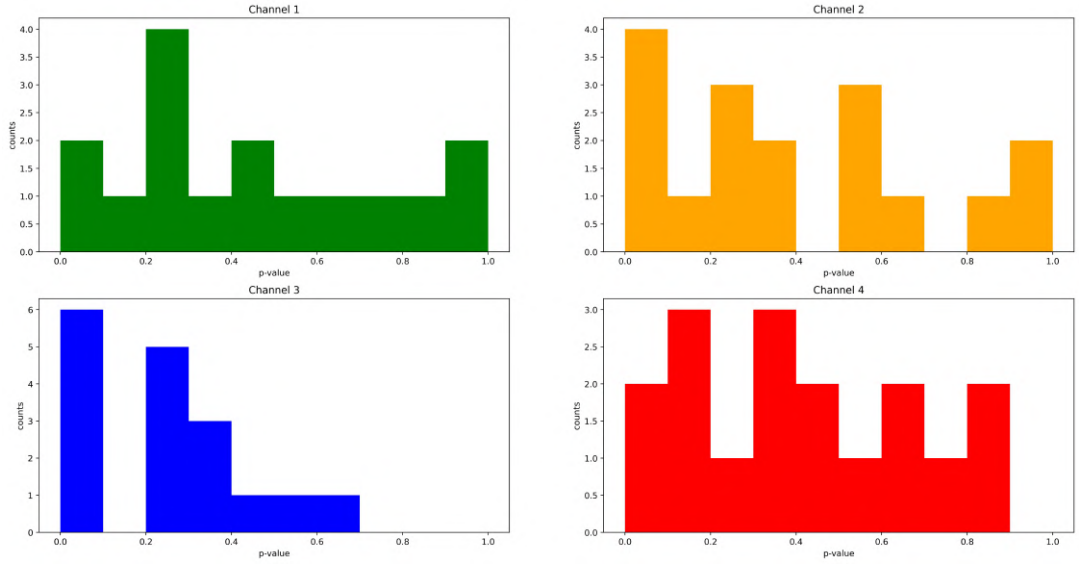

Figure 3.6: p-value distributions for the four channel, referring to the 16 runs of channel 1 and 17 runs of the others used to adjust the fits. The fit range used is 260 ns − 450 ns for channels 1, 2 and 3 and 250 ns − 600 ns for channel 4. With this restricted range, channels 1 and 2 have an almost uniform distribution as channel 4; channel 3 still shows an accumulation toward zero, but the fitting range has not been further restricted.

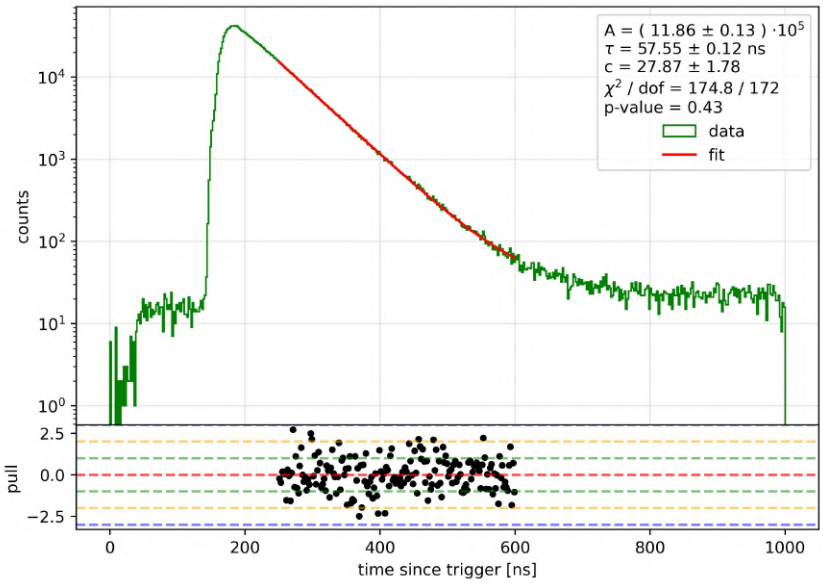

Figure 3.7: Exponential fit for channel 4 on a run acquired on May 13$^{\text{th}}$. The fitting curve in red is overlapped to the distribution, and the goodness-of-fit test shows a perfect agreement to the data; the extracted time constant is $\simeq 57.5$ ns.

The cuts applied and the fit configurations used in the final analysis for the different channels are summarized in Table 3.1.

	Hit level cut	**Event level cut**	**Bin width**	**Fit range**
Channel 1	$\geqslant 0.3$ PE	$\geqslant 3$ PMTs	2 ns	[260 ns ; 450 ns]
Channel 2	$\geqslant 0.3$ PE	$\geqslant 3$ PMTs	2 ns	[260 ns ; 450 ns]
Channel 3	$\geqslant 0.3$ PE	$\geqslant 3$ PMTs	2 ns	[260 ns ; 450 ns]
Channel 4	$\geqslant 0.3$ PE	$\geqslant 7$ PMTs	2 ns	[250 ns ; 600 ns]

Table 3.1: Cuts on hit and event levels, binning and fit range for the different channels, used for the final analysis.

The time constant results from the different channels, shown in Figure 3.8 (left), express the trend of the Neutron Veto optical properties in the period between December 2021 and July 2022. The Reflectivity Monitor provides precise measurement with small statistical errors, less than 1 %. However, different optical fiber channels lead to different results for the time constant, so a systematic uncertainty is also present. Considering the tendencies rather than the absolute values, the behaviours of the time constants are in

agreement: the trend is constant and no decrease is observed in the considered period[2]. The values stay between 55.5 ns and 57.5 ns. The measures obtained using channel 4 have a significantly smaller uncertainty compared to the others.

In Figure 3.8 (right), weighted averages of the time constants are made to get a unique result from the different channels for each acquisition day. $1/\sigma^2$ (with σ statistical error coming from the fit) have been used as weights. Due to its smaller error, the values are dominated by the results from channel 4. The measured time constant is $\simeq 57.3$ ns.

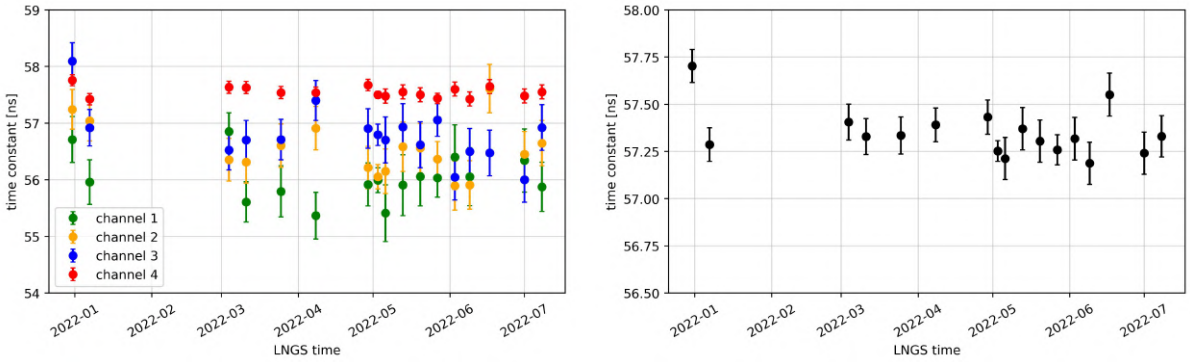

Figure 3.8: Left: results of the time constants for the considered runs of the fours channels. A constant trend is observed for all of them, even if a shift is present between different channels. Error bars represent the uncertainties coming from the fits. Right: weighted averages of the four channels, using $1/\sigma^2$ as weight.

It is important to notice that the errors associated to the weighted averages (~ 0.1 ns) cannot be interpreted as errors on the final measurements; in fact, they do not take into account the systematic differences between values provided by different channels, which are much larger (~ 2 ns). They only represent the expected statistical fluctuations of the weighted averages. The time constant result of this first phase can be expressed as $\tau = (57 \pm 1)$ ns.

3.3 Simulations

The time constant obtained by the fits as illustrated in the last Section is the parameter that best describe the optical properties of the Neutron Veto; the photon absorption time is the main information to be monitored. However, it does not provide separate informations about water transparency and walls reflectivity. If we observe a drop in the time constant and we suspect a loss of transparency (for example, after the insertion

[2]The first run for each channel, acquired on December 31$^{\text{th}}$ 2021, are characterized by systematically larger time constants, in particular for channels 2, 3 and 4. Since the corresponding p-values are 0.02, 0.01 and 0.01, it is probably due to some issue related to those runs.

of the Gd sulfate) we are not able to quantify such decrease. On the other hand, if we expect a decrease of transparency or reflectivity for some reason, we aim to predict the corresponding drop of the time constant.

Monte Carlo simulations have been performed in order to better characterize the different contributions that affect the time constant τ, with the help of a dedicated model.

3.3.1 Photon absorption model

A simple model describing the behaviour of photons in the Neutron Veto has been built, as starting point to interpret and analyse the results of the simulations. Considering a photon traveling inside the NV, for each time interval dt it has a given probability λ to be lost[3]. The number of photons as a function of time is then governed by the equation

$$\frac{dN\left(t\right)}{dt} = -\lambda N\left(t\right) . \tag{3.2}$$

If N_0 photons were present in the detector at time zero, the number of photons at time t is

$$N\left(t\right) = N_0\, e^{-\lambda t} = N_0\, e^{-t/\tau} \tag{3.3}$$

with the definition $\tau = 1/\lambda$; this τ is nothing else than the time constant measured with the Reflectivity Monitor. The loss probability λ can be expressed as the sum of different contributions. Three sources can be identified:

- λ_{abs}: the probability that the photon is absorbed by the water (or Gd-water solution);
- λ_{ref}: the probability that the photon hits a wall and is not reflected back (absorbed or transmitted);
- λ_{geom}: the probability that anything else happens; the photon can be absorbed by other detector materials (as iron supports) or by a PMT (either being detected or not). This contribution takes into account everything is not affected by transparency or reflectivity and only depends on the geometry of the Neutron Veto.

Photons, especially in the blue light and UV range, can also elastically scatter with the water atoms (Rayleigh scattering); since this interaction does not change the wavelength of the photons and only results in changing their paths, it does not affect the Neutron Veto efficiency and can be neglected.

In this way:

$$\lambda = \lambda_{abs} + \lambda_{ref} + \lambda_{geom} . \tag{3.4}$$

[3] 'Lost' here does not necessarily mean that it is not detected but rather that its path is interrupted for some reason. Even a photon hitting a PMT and producing a signal is considered as lost.

Each of them corresponds to a time constant; hence, the total time constant τ can be written as

$$\tau = \left[\frac{1}{\tau_{abs}} + \frac{1}{\tau_{ref}} + \frac{1}{\tau_{geom}} \right]^{-1} . \tag{3.5}$$

The different contributions can be described in the following way.

τ_{abs} is related to the absorption length ℓ_{abs} of photons in water; if they travel with a speed $v = c/n$, the absorption time constant is given by

$$\tau_{abs} = \frac{\ell_{abs}}{v} . \tag{3.6}$$

In the simulations a parameter T has been defined as multiplicative factor to be attached to the nominal absorption length of pure water ℓ_0, such that $\ell_{abs} = T\,\ell_0$. The latter comes by a predefined model (more details will be given in Section 3.3.2).

The probability λ_{ref} is instead the multiplication of two factors:

- the probability that the photon hits one of the walls in the given time interval, k_w;
- the probability that the photon is not reflected. The reflectivity is described by a parameter R, so this probability equals $1 - R$.

In this way, $\lambda_{ref} = k_w \cdot (1 - R)$ and the respective time constant reads

$$\tau_{ref} = \frac{1}{k_w\,(1 - R)} . \tag{3.7}$$

Altogether, the time constant can be written as a function of T and R:

$$\tau\,(T, R) = \left[\frac{v}{T\,\ell_0} + k_w\,(1 - R) + \frac{1}{\tau_{geom}} \right]^{-1} . \tag{3.8}$$

3.3.2 Simulations and analysis

To simulate Reflectivity Monitor runs, a predefined macro has been employed. The geometry of the Neutron Veto is implemented as part of the Monte Carlo simulations used in XENONnT. Photons are generated with a single wavelength (375 nm in this case) from the position corresponding to the Reflectivity Monitor support, pointing downward or upward depending on the channel to simulate. The photons propagation and interactions are simulated with the software GEANT4 [158]. We considered a simplified approach where no waveform nor hit simulators were used for the Neutron Veto: when a photon hits a PMT, it is always detected and provides 1 PE area; timings are also saved and referred to the beginning of each event. Pure water has been used as medium since these simulations aimed to provide an interpretation to the results of the first phase

of operations of the Neutron Veto, without Gadolinium doping. For each simulation, different values of the parameters T and R have been selected, corresponding to different values of transparency and reflectivity.

A 2D scan has been performed running a total of 36 simulations, using all the combinations of the parameters T (with values 0.5, 0.6, 0.7, 0.8, 0.9, 1.0) and R (with values 0.95, 0.96, 0.97, 0.98, 0.99, 1.0). The absorption length of pure water as a function of the photon wavelength is modeled as in Figure 3.9. At the Reflectivity Monitor laser wavelength the absorption length is 487 m; values of $T = 0.5, 1.0, 2.0$ correspond so to absorption lengths of 243.5 m, 487 m, 974 m.

In Figure 3.10 the distributions of photons, as a function of wavelength, reaching the NV PMTs are plotted, overlapped to the average PMTs Q.E..

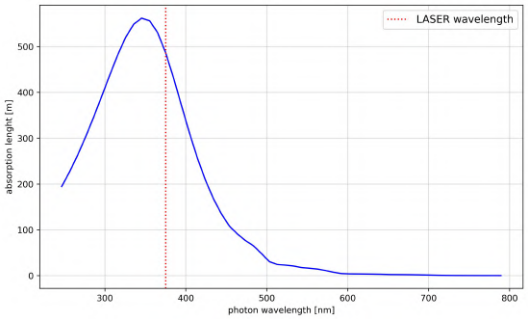

Figure 3.9: Pure water absorption length as a function of the photon wavelength. The wavelength used for the Reflectivity Monitor is denoted by the red dotted line.

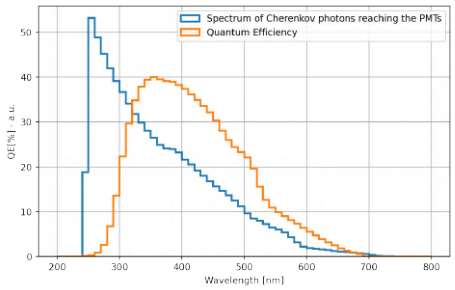

Figure 3.10: Distribution of signals reaching the NV PMTs as a function of the wavelength. In blue, the Cherenkov spectrum convoluted with the pure water absorption; in orange, the average Q.E. of the PMTs. At 375 nm we are close to the maximum Q.E..

For these simulations, 100 photons per event have been produced and directed downward (to emulate channel 4, which shows the best performance in real data). 10 000 events have been simulated per each run. In this way the number of distinct PMTs detecting a photon and the total area of the events (which correspond to the total number of detected photons), reported in Figure 3.11, are similar to the ones in the real Reflectivity Monitor runs for channel 4 (see Figure 3.4). The total number of hits per run is $\sim$ 400 000.

The hit timings with respect to the beginning of each corresponding event have been used to build the exponential distributions. In Figure 3.12 (left) examples of exponential distributions with fixed T (= 0.5) and different values of R are reported; the effect of walls reflectivity is visible in the different slopes of the curves. In Figure 3.12 (right) is shown an example of exponential fit on a run with parameters $T = 0.7$ and $R = 0.98$.

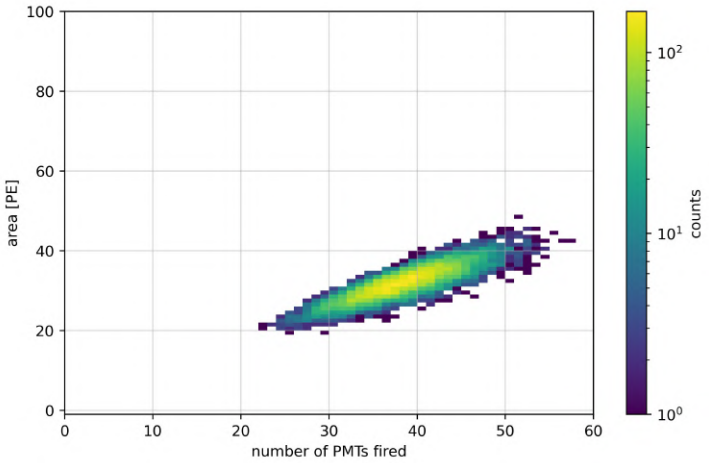

Figure 3.11: Number of PMTs contributing to the events and area (i.e. total number of hits) of the events for one of the simulated runs.

The fits have been performed, for all the runs, in the range $[\,50\,\text{ns}\,;\,400\,\text{ns}\,]$ and with 2 ns width bins. The fitting curve is similar to the one in (3.1) used for the Reflectivity Monitor analysis but without the constant component described by the parameter c. Indeed, the flat background component was not simulated in the Monte Carlo macros. No cuts on data were necessary.

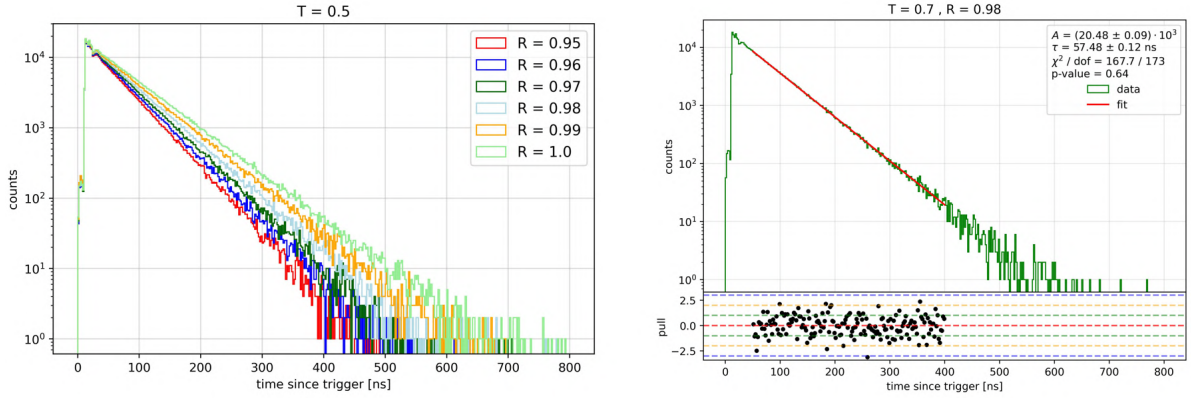

Figure 3.12: Left: exponential distributions for runs with $T = 0.5$ and $R = 0.95, 0.96, 0.97, 0.98, 0.99, 1.0$. Larger reflectivities produce larger time constants of the exponential. Right: Example of exponential fit performed on one of the simulated runs. It shows good fit performances (p-value = 0.64) and the time constant obtained (57.5 ns) is similar to the ones measured by the Reflectivity Monitor on real data shown in Figure 3.8.

3.3.3 Results

For each simulated run, an exponential fit with the same conditions has been performed, extracting a time constant τ. The values obtained and the goodness-of-fit in terms of p-values are shown respectively in Figure 3.13 (left) and Figure 3.13 (right).

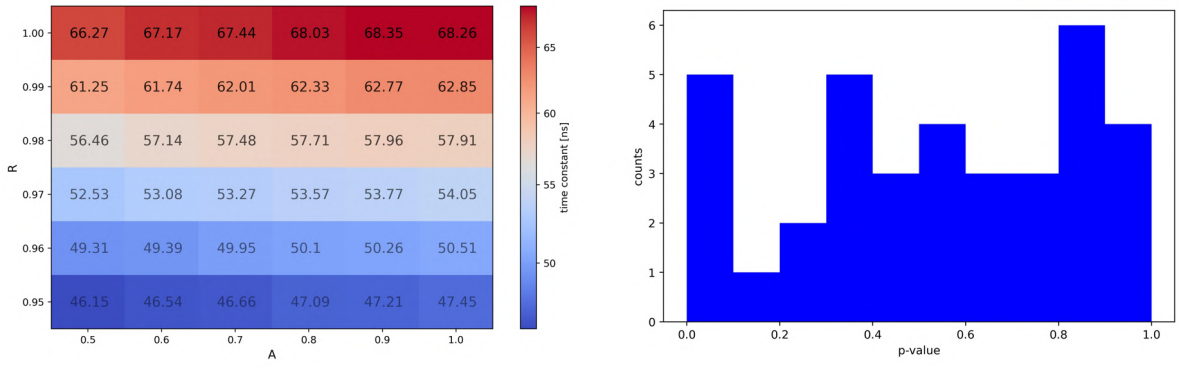

Figure 3.13: Left: time constants expressed in nanoseconds obtained from the 36 simulated runs varying T and R. Right: p-values of the exponential fits. The distribution is almost uniform, so the fits are acceptable.

In the range studied here, a variation of the reflectivity has a stronger impact on the time constant than a variation of the transparency. At fixed T, changing A from 0.5 to 1.0 increases the value of τ by ~ 3 %; at fixed A, changing T from 0.95 to 1.0 the increases it by more than 40 %.

3.3.4 Estimation of the geometric component

From the results of the 2-dimensional scan, reported in Figure 3.13 (left), it is possible to make further analyses and extract an estimation of the geometric time constant τ_{geom}. This has been done in two ways which use the same data and so are not independent; however, the agreement between the two results is a confirmation of the analysis made.

Estimation from runs at fixed R

For each fixed value of R, (3.5) can be rewritten as

$$\tau = \left[\frac{1}{\tau_{abs}(T)} + \frac{1}{\tau_{as}(R)} \right]^{-1} \tag{3.9}$$

where $\tau_{as}(R)$ is the asymptotic value of τ when the reflectivity parameter is R and in the limit $T \to \infty$ (in that case τ_{abs} is also infinite). The asymptotic time constant is

given by

$$\frac{1}{\tau_{as}(R)} = \frac{1}{\tau_{ref}(R)} + \frac{1}{\tau_{geom}}. \tag{3.10}$$

For each of the six values of R, the time constants obtained from the fits as a function of T have been fitted with the function in (3.9). The fits have been performed with the least squares method with the asymptotic time constant τ_{as} as only parameter. One of these fits is plotted in Figure 3.14. The p-values demonstrate that the fits and the model are correct, as reported in the same figure.

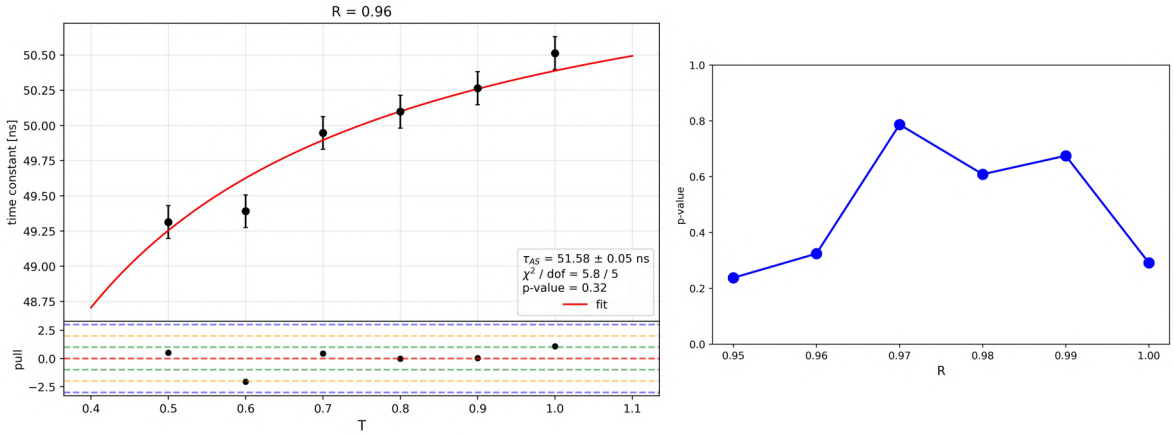

Figure 3.14: Examaple of fit performed on the runs with the parameter R fixed at 0.96. The estimated value is $\tau_{as}(R = 0.96) = 51.58\,\text{ns}$ and the χ^2 proves that the fit is good. The p-values for all the six fits are shown on the right.

The six values of the asymptotic time constant, each referring to a different R, have been in turn fitted with the function in (3.10). Two parameters have been used: the geometric time constant τ_{geom} (the parameter of interest) and the probability k_w, which enters in τ_{ref} by (3.7). The result of the fit is displayed in Figure 3.15.

The geometric time constant has been found to be (70.69 ± 0.05) ns. The value of k_w can provide informations about the correctness of the simulations. In fact, considering that photons travel in water at a speed of $\simeq 0.2\,\text{m/ns}$, if they hit a wall every $1/k_w \simeq 7.7\,\text{ns}$ that means that they travel on average $\simeq 1.5\,\text{m}$ between each hit, which is similar to the characteristic dimensions of the Neutron Veto. This is another proof that the model is correct.

Estimation from runs at fixed T

The same approach has been applied in inverse order. Considering groups of runs characterized by the same T, least squares fits have been performed to the values of the time

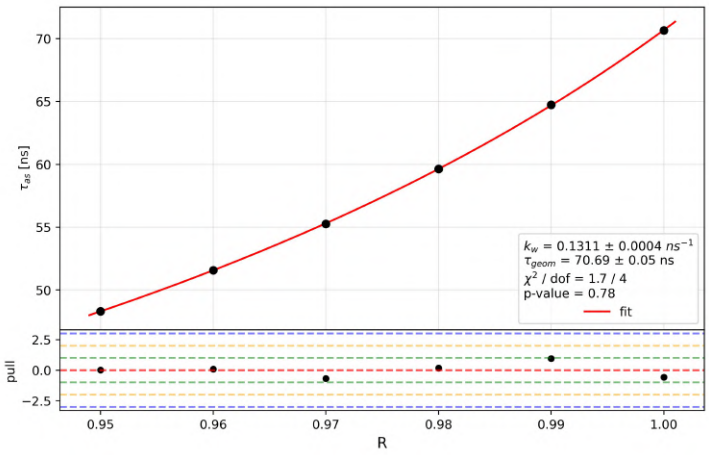

Figure 3.15: Fit on the asymptotic time constants obtained by the previous fits. The p-value is 0.78. The parameters found are $\tau_{geom} = 70.69\,\text{ns}$ and $k_w = 0.13\,\text{ns}^{-1}$.

constant within each group. It has been expressed as

$$\tau = \left[\frac{1}{\tau_{ref}\,(R)} + \frac{1}{\tau'_{as}\,(T)}\right]^{-1} \tag{3.11}$$

where a second asymptotic time constant τ'_{as} has been defined as

$$\frac{1}{\tau'_{as}\,(T)} = \frac{1}{\tau_{abs}\,(T)} + \frac{1}{\tau_{geom}}\,. \tag{3.12}$$

It is the asymptotic value of τ with a fixed T and in the limit $R \to 1$. Six fits with the function in (3.11) have been performed, extracting a value of $\tau'_{as}\,(T)$ for each of them. An example of such fits and the p-values are reported in Figure 3.16.

The six τ'_{as} obtained by the fits, displayed as a function of T are shown in Figure 3.17, together with the fit with the function in (3.12). The geometric time constant is found to be $\tau_{geom} = (70.69 \pm 0.05)$ ns, the same obtained with the previous method. As already stressed, these two methods use the same data fitted in different orders, so the same results were expected.

Estimation with new simulations

In order to prove the result of τ_{geom} in a more direct and independent way, other simulations have been performed. Eight runs have been simulated, with the same settings as the previous ones; the value of R has been fixed at 1.0 and the values of T were 1, 2, 5, 10, 25, 100, 10^3, 10^4. With perfectly reflecting surfaces ($R = 1$) and going to

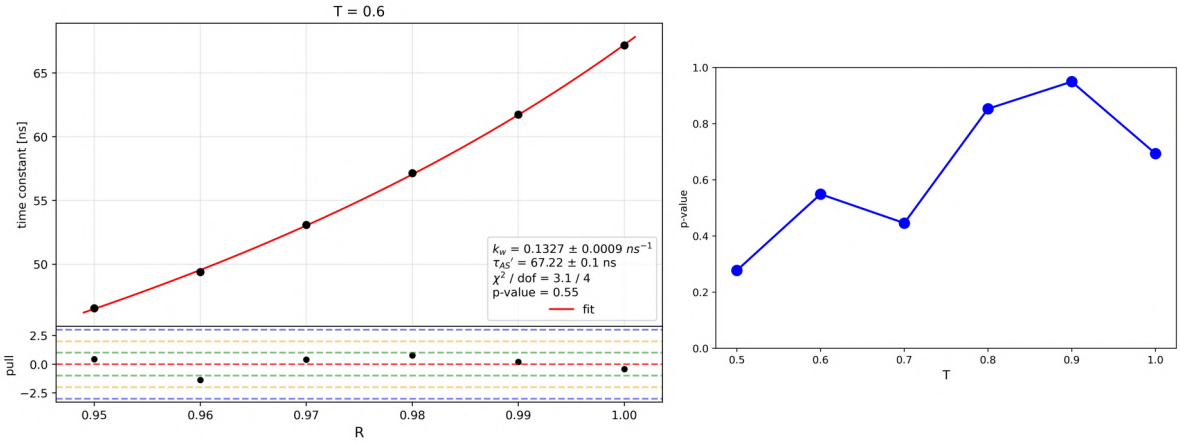

Figure 3.16: Examaple of fit performed on the runs with the parameter T fixed at 0.6. The estimated value is $\tau'_{as}\,(T = 0.6) = 67.22\,\text{ns}$ and the χ^2 proves that the fit is good. The p-values for all the six fits are shown on the right.

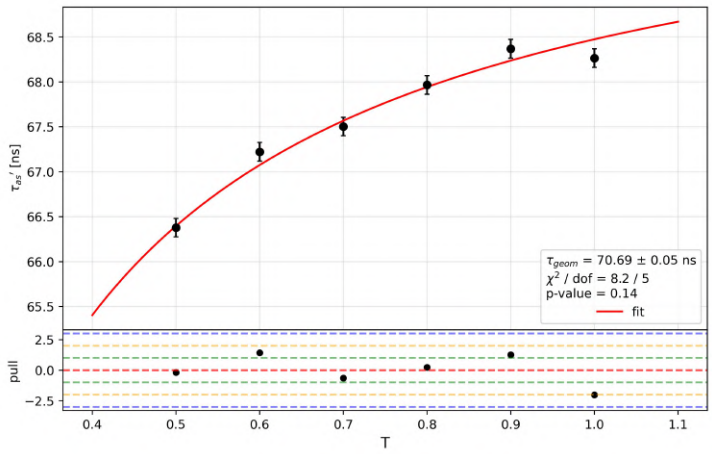

Figure 3.17: Fit on the asymptotic time constants obtained by the previous fits. The p-value is 0.14. The parameter found is $\tau_{geom} = 70.69\,\text{ns}$.

a perfectly transparent water ($T \to \infty$) the measured values of the time constant τ approach the geometric time constant τ_{geom}. In fact, from (3.8), we have:

$$\tau\,(T \to \infty, R = 1) = \tau_{geom}\,. \tag{3.13}$$

The time constants obtained by these new simulations (extracted again by exponential fits) are reported in Figure 3.18, where the value of τ_{geom} found with the method exposed above is also shown. The plot shows that with $T \gtrsim 10$ the time constant already approaches τ_{geom} and stays constant, within statistical fluctuations, for greater values.

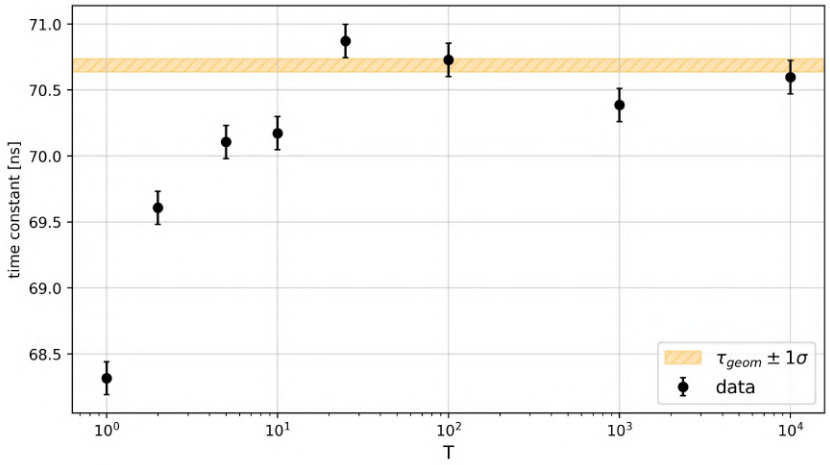

Figure 3.18: Time constants found by the new simulations, represented by black dots and error bars, compared to the value of τ_{geom} previously estimated. This latter is represented by the yellow bar, covering 1σ uncertainty. After $T = 10$, the values of τ are already close to τ_{geom}.

3.3.5 Summary of the simulations

From the results of the simulations exposed in Section 3.3.3 and the analyses of Section 3.3.4, the main informations that can be extracted are:

1. in the studied range of reflectivity and transparency, the reflectivity has a larger impact on the time constant, as shown in Figure 3.13 (left);

2. the Neutron Veto is characterized by a geometric time constant τ_{geom}, independent on reflectivity and transparency, that affects the time constant measured with the Reflectivity Monitor. Its estimated value is (70.69 ± 0.05) ns.

The first point can be understood considering the nuisance parameter, k_w, which was found to be $\simeq 0.13\,\text{ns}^{-1}$. Its inverse, $\simeq 7.7$ ns, represents the average time between two reflections on the NV walls. Considering that photons travel in the Neutron Veto $\simeq 57$ ns before being absorbed or detected, the average number of reflections that they experience is $\simeq 7.5$. During their path, they travel $\simeq 11$ m inside the NV, a distance much smaller than the absorption length of pure water; going from $T = 1.0$ to $T = 0.5$ translates in absorption lengths going from ~ 500 m to ~ 250 m and it does not have a strong impact. So, the reflectivity is more crucial for the time constant given the relatively small dimensions of the Neutron Veto and the consequent high number of reflections occurred to photons.

The second point allows to better understand the time constant results obtained with the Reflectivity Monitor. First, τ_{geom} represents the maximum possible value of τ,

corresponding to perfect walls reflectivity and water transparency. Knowing its value, there is a degree of freedom less in (3.5) and a measure of τ corresponds to a line in the T-R space. In Figure 3.19, the possible values of T and R are shown for different values of τ.

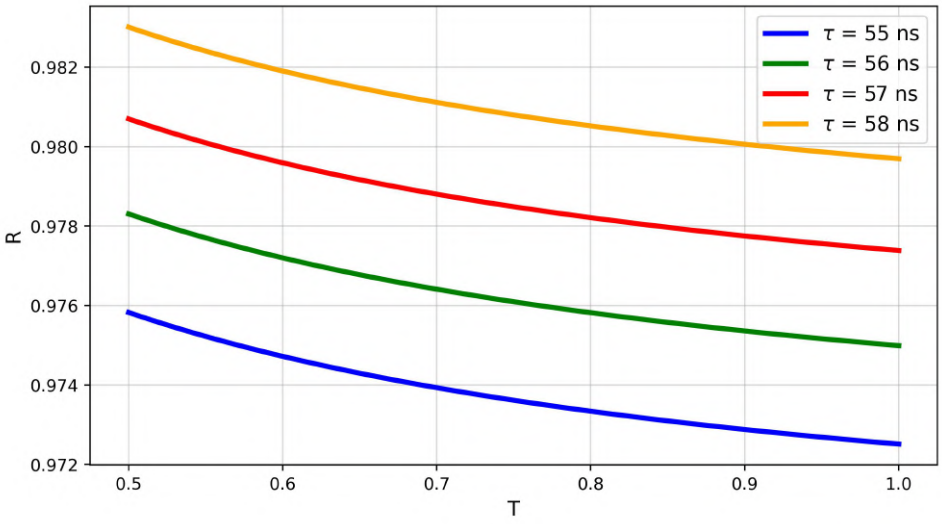

Figure 3.19: Values of T and R corresponding to different values of τ. With these curves, if an independent measurement provides the absorption length of water or the reflectivity of the ePTFE in addition to the time constant measurement of the Reflectivity Monitor, it is possible to estimate the other variable.

3.4 Validation with background data

The Reflectivity Monitor showed to be a reliable tool to monitor the optical properties of the Neutron Veto. Each optical fiber channel provides measurements with small statistical errors, even though a systematic difference is present between different channels. However, the Reflectivity Monitor employs a monochromatic source of light; scientific data of the Neutron Veto consist instead of in Cherenkov light, which has a continuous spectrum as in (2.7). In addition, the PMTs Q.E. also depend on the photon wavelength.

For these reasons, it is important to validate the Reflectivity Monitor results making an analysis on a wide wavelength spectrum. Using NV background data is the best solution since they are the same used for high-level analyses. They have been used to extract a time constant which has been compared to the one obtained with the Reflectivity Monitor.

3.4.1 Time constant from background data

In the neutron veto there is an almost constant rate of events due to background, mostly coming from gammas from radioactivity of the materials surrounding the veto (PMTs, ePTFE reflectors, stainless-steel support structure, etc.). The overall rate is about 100 Hz with a coincidence threshold of at least 4 PMTs. The trend of this background rate for two different coincidence thresholds is shown in Figure 3.20.

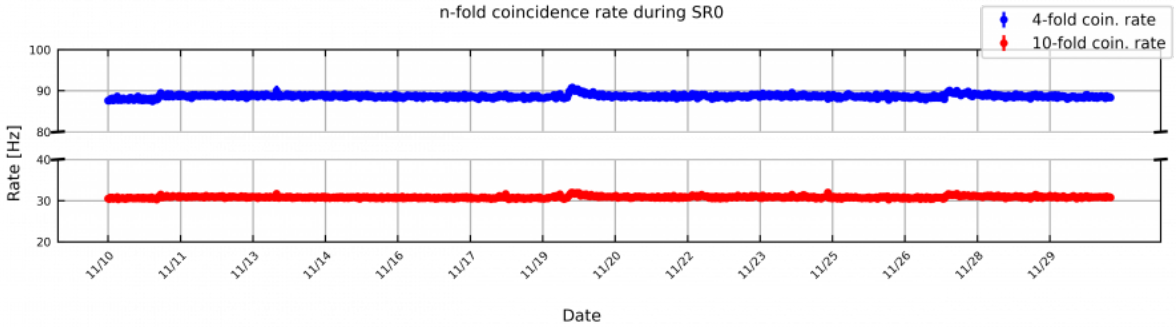

Figure 3.20: Neutron Veto background rate for 4-fold coincidence (blue) and 10-fold coincidence (red).

A procedure similar to the one used for the Reflectivity Monitor analysis can be applied to background data. For each background event, it is possible to build an exponential distribution by taking the timings of all the hits within the event and subtracting the timing of the first hit. Background data are acquired in self-trigger mode so, differently from the Reflectivity Monitor runs, there is no reference time; the time of the first hit is the best reference that can be chosen, but it is subject to uncertainties. Some selection cuts are needed before the analysis: 'clean' events must be chosen in order to build an exponential distribution from which it is possible to extract a time constant.

To characterize background data and study the cuts suitable for this purpose, a run acquired on September 16$^{\text{th}}$ 2022 has been chosen as reference. In Figure 3.21 (left) the distribution of number of PMTs contributing to each event and total area of the event for the reference run are plotted. The majority of the events accumulate at low area and low number of PMTs, but the spread is much greater than the one shown in Figure 3.4. In Figure 3.21 (right) is reported the distribution as a function of number of PMTs only; some particular values are highlighted. Events with a low number of PMTs likely have high uncertainties, due to the small number of hits contributing to the exponential distribution. Events with a large number of PMTs are likely due to muons, that produce a big number of hits but can provide other sources of uncertainties, as PMTs afterpulses.

To measure the time constant with background data, different cuts on the number of PMTs per event have been tested on the reference run. They provide strong differences in the temporal distributions of hits within each event; in Figure 3.22 are shown some

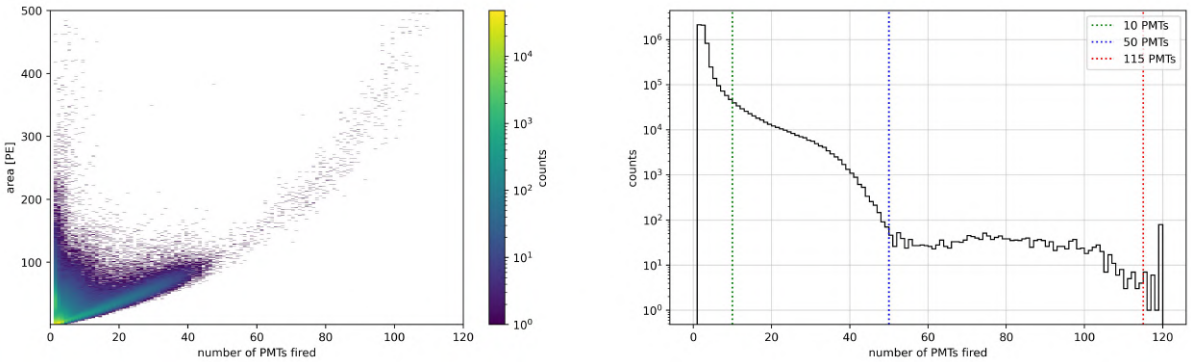

Figure 3.21: Left: distribution of number of PMTs fired and total area of the events for a run acquired on September 16$^{\text{th}}$ 2022, taken as reference. Right: same distribution as a function of number of PMTs involved only. Different values (10, 50, 115) are proposed to separate different events categories.

examples of that.

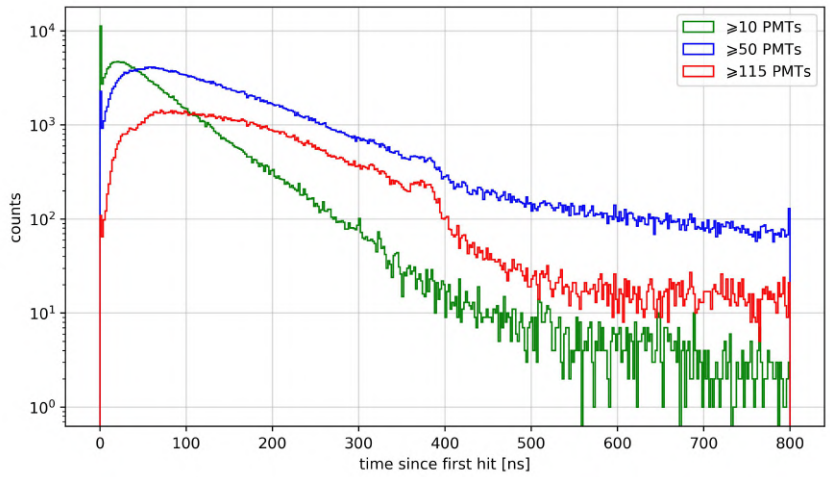

Figure 3.22: Distribution of the hits timings with respect to the first hit of each event, for the reference run. Different cuts in the minimum number of PMTs lead to different distributions. The one built after requiring only 10 PMTs fired is more similar to an exponential.

For the reference run different cuts in the minimum number of PMTs have been attempted. 17 thresholds have been chosen between 5 and 115 PMTs. For each of them, the time distribution of the hits have been built and an exponential fit as in (3.1) has been performed with 2 ns width bins and in the range 50 ns − 200 ns. The results of the fits, in terms of time constants and p-values, are reported in Figure 3.23 (left). It

is possible to see that the p-values are acceptable until the threshold of 40 PMTs, then they drop to zero. The corresponding time constants are almost stable until 30 PMTs threshold and then are subject to an increase. A zoom in the region with the lower cuts (reported in Figure 3.23 (right)) shows that the values stay particularly stable in the region $\sim 15 - 25$ PMTs.

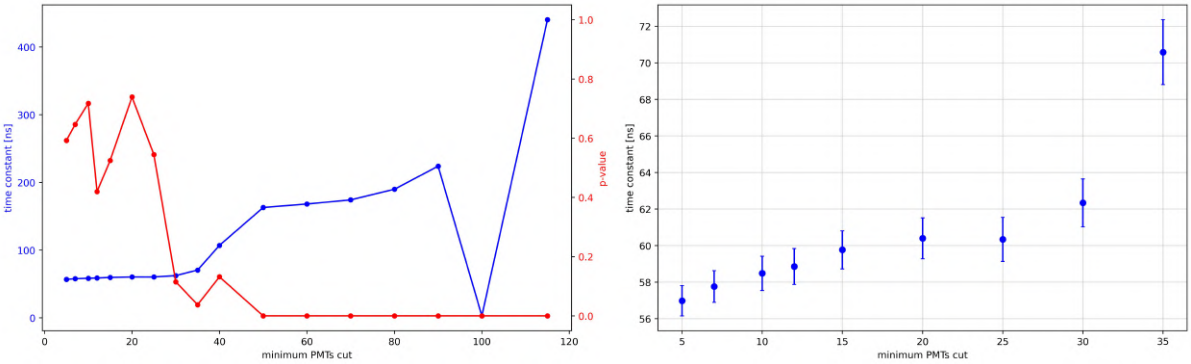

Figure 3.23: Left: results of the minimum number of PMTs cut scan. The time constants (blue) are almost stable until 30; at the same point, the p-values (red) start becoming unacceptably low. Right: zoom of the time constant behaviours at lower values of the cut; they show a slight increase at the beginning, then stay stable until $\sim$ 25 before starting another increase.

The value chosen as minimum number of PMTs is therefore 20. Another scan has been then performed, fixing the minimum number to 20 and adding a cut on the maximum number of PMTs. This is not expected to give a strong impact, since the events with a high number of PMTs involved are orders of magnitude less than the ones with $\lesssim 55$ PMTs, as shown in Figure 3.21; however, they have a bigger weight since they contain more hits and provide distributions not exponentially shaped (see Figure 3.22). The results of this second scan are shown in Figure 3.24. The time constant stays stable until ~ 40 PMTs cut and then starts increasing: including events with more than $\sim 40 - 50$ PMTs has a visible effect in the time constant. Hence, for the final analysis, only the events with a number of contributing PMTs between 20 and 40 have been selected.

3.4.2 Results

After establishing the cuts on the number of contributing PMTs described in the previous paragraph, exponential fits have been applied to a series of self-trigger runs. The time distributions have been binned, as usual, with 2 ns width bins. The fits have been performed in the range 50 ns $-$ 200 ns. The results of 14 runs taken in the period April-July 2022 compared to the results of the Reflectivity Monitor runs in the same temporal range are shown in Figure 3.25: the time constants extracted by background data show

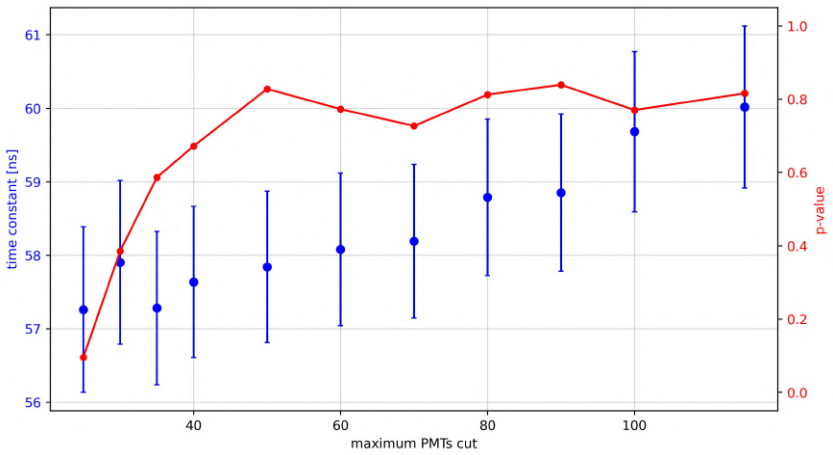

Figure 3.24: Time constant results and corresponding p-values for different choices of maximum number of PMTs per event, with the minimum number fixed at 20 PMTs. A constant trend is observed until 40.

a larger uncertainty, ~ 10 times the ones of the Reflectivity Monitor runs. However, it is important to see that the two measures are in agreement, confirming that the Reflectivity Monitor is a good measure of the optical properties of the Neutron Veto, even if it only employs a single wavelength. The p-values, also reported in Figure 3.25, show acceptable performances of the fits.

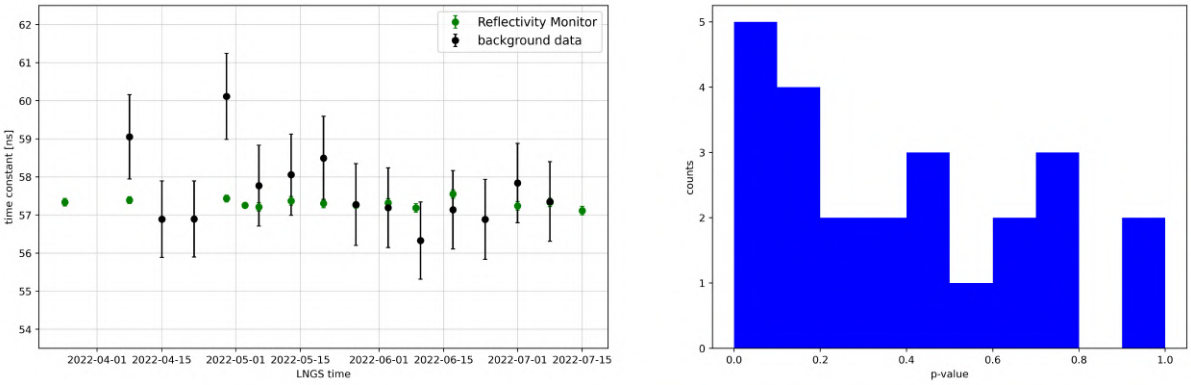

Figure 3.25: Time constant results from background data, in black, compared to the Reflectivity Monitor results (in green). On the right, the p-values of the fits on background data. The two measurements are in agreement.

Chapter 4

Gadolinium-water purification system

In Section 2.3.3 we summarized the main reasons why the addition of Gadolinium to the Neutron Veto water will increase its performances. The importance of maintaining at the same time a good water transparency has also been underlined. The Water Loop Plant (WLP) has been used so far to purify the Neutron Veto water and has shown excellent results; however, it cannot work when Gd is dissolved in water because it would remove Gd ions together with the other impurities. A new system, the Gadolinium-Water Purification System (GdWPS) described in detail in this Chapter, has been designed and installed at LNGS with the double goal of dissolving the Gd salt in water and preserving the transparency of the solution. This latter can be then monitored in two ways: with the Reflectivity Monitor described in the last Chapter and by direct measurements of transparency on samples of water or Gd-water, which will be described in Section 4.3.

4.1 Purposes and description

The goals of the GdWPS can be summarised in three points:

1. insert and dissolve the Gd sulfate in the NV (and MV) water;
2. reach the target concentration, maintain it over time and be able to monitor it;
3. preserve the optical properties of the Neutron Veto by purifying the solution from impurities that may affect the transparency.

The EGADS facility [155], used by the SuperKamiokande experiment to test the technology of the Gd insertion and water purification before applying it to the detector, has been taken as model for the GdWPS thanks to a formal agreement and the presence of colleagues involved in both projects: XENON and SK. The strategies used by the two

plants to achieve the above mentioned goals are similar. After Gadolinium is dissolved in water, Gd-enriched and Gd-depleted solutions are divided along the system via dedicated filters; then, an ion purification system removes impurities from the Gd-depleted part, avoiding in this way a relevant loss of Gadolinium. The two parts are finally rejoined and purified with filtration elements unable to absorb Gd ions. In this way, the solution is purified from impurities and the concentration of the Gd-Sulfate is preserved. A picture of the GdWPS is shown in Figure 4.1.

Figure 4.1: Picture of the Gadolinium-water purification system, placed close to the XENON tank.

The elements used by the GdWPS can be divided in the following subgroups:

- *circulation elements*: they make the plant running and allow to adjust pressures, temperatures and flow rates;
- *Gadolinium insertion system*: a dedicated system to insert the Gd-Sulfate in the GdWPS;
- *purification elements*: they purify water and perform the separation in Gd-rich and Gd-depleted solutions;

- *sensors*: their importance is not only in monitoring the technical parameters for making the plant running, but also in quantifying the purification and separation powers of the system.

All the component of the system are schematised in the Piping and Instrumentation Diagram (P&ID), reported in Figure 4.2.

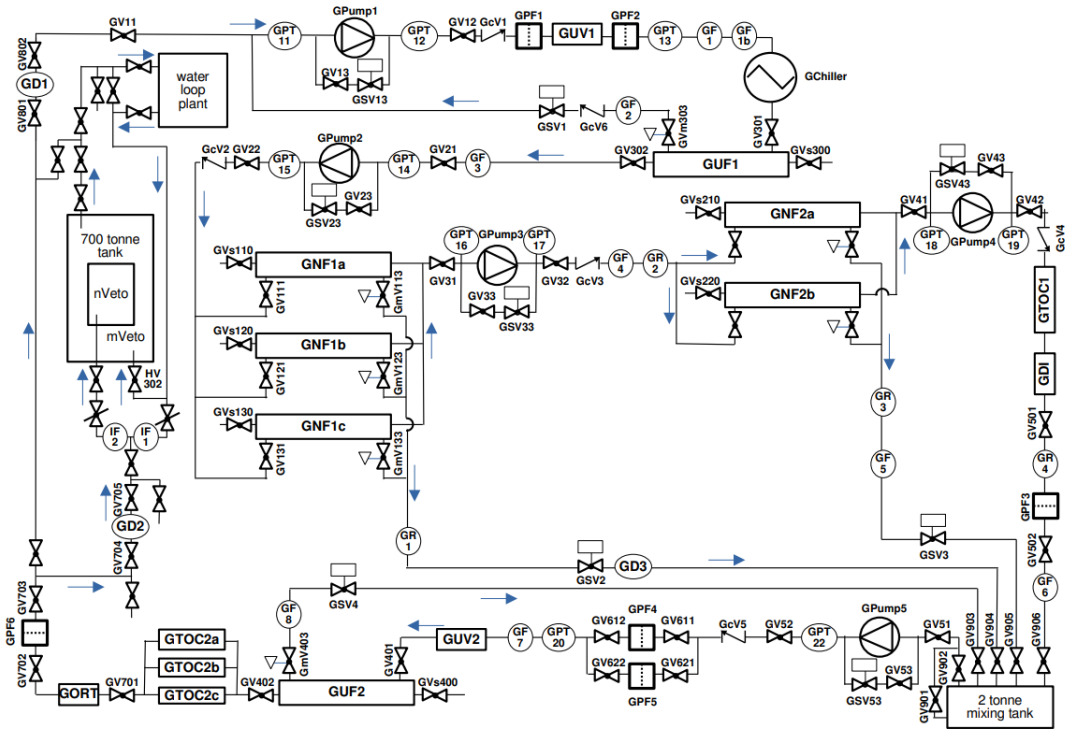

Figure 4.2: Piping and Instrumentation Diagram (P&ID) of the GdWPS. All the relevant circulation elements (as pumps and valves), filters and sensors are reported.

In the next sections, all the elements and the functioning of the system are explained in details.

4.1.1 Circulation elements

In the GdWPS five pumps operate in series to make water circulate along the plant. Water is extracted from the top of the 700 m^3 tank hosting MV and NV (that will be called XENON tank), as represented in the top-left part of Figure 4.2. Four pumps, labeled from 1 to 4, make water flow in different branches where filtration stages and various sensors are placed; they will be detailed in the next sections. The different branches finally reconnect in the *mixing tank* (bottom-right angle of Figure 4.2), a 2 tons

stainless-steel container where the Gd sulfate dissolution happens (see Figure 4.3). From the mixing tank, water is extracted by another pump (GPump5) that pushes it back to the XENON tank, where it enters by two separate branches: one is connected to the floor of the tank and the other directly to the Neutron Veto. In this way water circulates in loop between the XENON tank and the mixing tank: the purification procedure happens between them. The goal flow rate to be achieved during the circulation is 2.4 ton/hour, equivalent to 40 l/min.

The connection of the plant to the XENON tank can also be bypassed; in this case, the outlet of GPump5 is connected to the inlet of GPump1. This *bypass mode* is particularly useful to test the GdWPS during the commissioning phase, since it avoids impacting the MV and NV water.

The pumps are responsible for keeping pressures and flow rates at the correct values across the plant. In addition, valves are placed on all the pipes. Some of them are manual (GV in the P&ID) and others are proportional solenoid valves (GSV in the P&ID) which have the advantage of being remotely adjustable via the Slow Control system. The valves are used to change pressures and flows through different branches, to 'isolate' elements of the system during particular operations (as assembly, disassembly, maintenance) and to mitigate the intensity of each pump. In fact, a bypass line is present around each pump with a solenoid valve installed; by opening (closing) the solenoid valve it is possible to weaken (enhance) the power of the pump. One of the pumps with its relative bypass branch is shown in Figure 4.4.

The power provided by the pumps, as well as other elements as UV lamps (which will be described in Section 4.1.3) heats up the whole system. Furthermore, the dissolution of Gd sulfate in water is favoured by low temperatures since the process is exothermic. A chiller is therefore needed to keep the temperature constant during the operation of the GdWPS. The chiller used by the plant is a ThermalCare Accuchiller NQA10 and is placed between the pumps 1 and 2. It features a compressor and two heat exchangers. The refrigerant is a hydro-fluorocarbon (HFC), with trade named R-410A, air-cooled by a condenser. The chiller contains a reservoir with demineralized water circulating in an internal loop. This water is chilled by the refrigerant through one of the two heat exchangers and cools down the GdWPS water through the other exchanger. In this way the water circulating in the plant does not come into contact with the refrigerant fluid. The temperature is set with an adjustable setpoint. The goal is to reach $\simeq 12$°C in the mixing tank. Two fans, placed on the chiller top, are used as vent. A picture of the chiller is shown in Figure 4.5.

4.1.2 Gadolinium insertion system

The Gadolinium sulfate is inserted in the system through the mixing tank. There, it is mixed and dissolves in water before starting circulating along the plant. The complete procedure for the Gadolinium insertion is:

Figure 4.3: Mixing tank of the GdWPS. The Gd sulfate is inserted by the top (see next Section). It holds 2 tons of water and has four input lines and two output lines (on the right in the picture).

Figure 4.4: One of the pumps of the GdWPS. In front of it, the corresponding bypass line with the solenoid valve adjusting the pump intensity.

Figure 4.5: Picture of the GdWPS chiller. In front of it, the control display acts as interface to the user; on the top, the two fans are used as vent.

- insert the Gd salt in an apposite *hopper* (see Figure 4.6 (1)) above ground;
- transport it sealed to the underground laboratory;

- connect the hopper to the pneumatic transfer system above the mixing tank through a flexible tube as in Figure 4.6 (2);
- activate the transfer system; a lance (Figure 4.6 (3)) helps catching the salt inside the hopper which can be seen through a window;
- after the insertion of the salt, a *stirrer* (see Figure 4.6 (4)) inside the mixing tank mixes the solution favouring the dissolution.

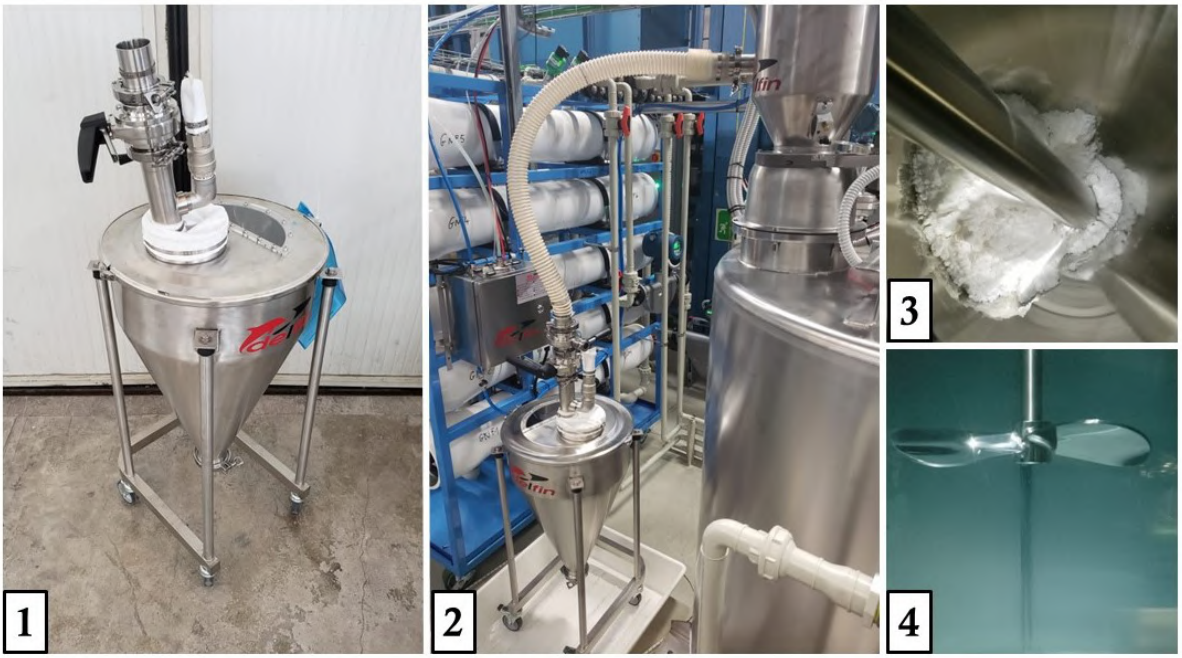

Figure 4.6: Pictures of all the elements needed for the insertion of Gadolinium salt inside the GdWPS: hopper for the Gd transport (1), connection to the pneumatic system above the mixing tank (2), lance which helps catching the salt inside the hopper (3) and stirrer inside the mixing tank which mixes the solution (4).

4.1.3 Purification elements

The filtration and purification procedure in the GdWPS happens in various steps. Different kinds of impurities must be removed by water: particulates are removed by dedicated filters; the growth of organic impurities, such as bacteria, is prevented using ultraviolet irradiation through lamps; different ions species can dissolve in water during the circulation and are removed by de-ionizing resins. This latter is a crucial point: the separation in Gd-rich and Gd-depleted water makes possible to reduce the ion concentration minimizing at the same time the Gadolinium loss.

Particle filters

The *particle filters*, denoted as GPF in Figure 4.2, are used to remove the impurities of relatively large dimensions by the GdWPS. There are six of them in different points of the plant; all of them are 'static' filters, so it is not foreseen to reject the impurities, which stay trapped in the filters themselves. They are Shelco Filters 4FOS series, with MS20 cartridges, effective on impurities larger than $20\,\mu$m. Pictures of two different types of particle filters used in the GdWPS are shown in Figure 4.7.

Figure 4.7: Particle filters of the GdWPS. On the left, two filters placed in parallel (GPF4 and GPF5); on the right, GPF2 (of different type).

Ultrafilters

For smaller impurities, ultrafilters have a stronger impact. Differently from particle filters, they have one input line and two output lines: a *product* and a *reject line*. The membranes of which they consist trap impurities and send them to the reject line, while purified water is directed to the product line. They do not trap Gd ions, which penetrate through the product lines. Two ultrafilters are used by the GdWPS (GUF1 and GUF2). Their reject lines are connected back to the main branch, so that the impurities circulate in loops. One of them is placed in the input line between the XENON tank and the GdWPS, and the other one in the output line, before returning the solution from the GdWPS to the XENON tank.

Nanofilters

The nanofilters are the key component of the GdWPS. Their purpose is to perform the separation between Gd-rich and Gd-depleted solutions. They are similar to the ultrafilters: the input water is divided into a prouduct and a reject. On the contrary of ultrafilters, however, all the ions with at least double valence are sent in the reject line (as well as Gd, which is in the form of trivalent Gd^{3+}). A total of five nanofiltration membranes are used in the plant. Three of them, placed in parallel, constitute the first nanofiltration stage (GNF1), which provides a reject line with high Gd concentration and a product line lacking in Gd; the second stage (GNF2) is placed in the product line of the first one and provides in its product line a further decreased Gd concentration. This second stage is made of two membranes in parallel. The performances of the nanofilters are quantified by their *Gadolinium separation efficiency*, i.e. the capability to remove Gd ions from the main branch.

The separation efficiency can be quantified in the following way. Considering the input line to a nanofilter[1], with flow rate ϕ_{in} and Gd concentration c_{in}, the number of ions that enters the filter is proportional to $\phi_{in}\, c_{in}$. In analogy, the product and reject lines will provide a number of Gd ions proportional respectively to $\phi_{prod}\, c_{prod}$ and $\phi_{rej}\, c_{rej}$. A picture of one of the GdWPS nanofilters and a schematic of the separation mechanism are shown in Figure 4.8.

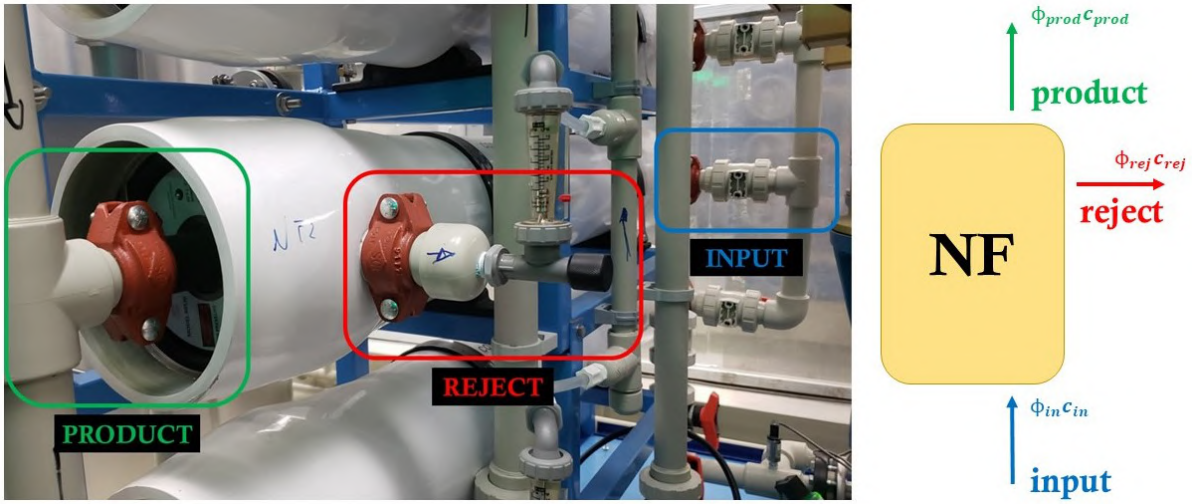

Figure 4.8: Picture of a GdWPS nanofiltration unit with input line (blue), product line (green) and reject line (red). On the right, a schematic summarizing its operation.

[1]Here the contributions of different membranes placed in parallel to form a nanofiltration stage are neglected. Their effects are joint together as unique element.

To ensure the conservation of the number of ions

$$\phi_{in}\, c_{in} = \phi_{prod}\, c_{prod} + \phi_{rej}\, c_{rej} \tag{4.1}$$

must hold. The separation efficiency can be defined as

$$\epsilon_{sep} = 1 - \frac{\phi_{prod}\, c_{prod}}{\phi_{in}\, c_{in}}\,. \tag{4.2}$$

Assuming (4.1), it can be expressed also as

$$\epsilon_{sep} = 1 - \frac{\phi_{prod}\, c_{prod}}{\phi_{prod}\, c_{prod} + \phi_{rej}\, c_{rej}}\,. \tag{4.3}$$

A perfect separation is obtained when no ion passes the filter and all of them exit through the reject line; in this case $c_{prod} = 0$ and so $\epsilon_{sep} = 1$.

Resins

Two kinds of resin are used in the GdWPS. They consist in polymer beads contained in plastic tanks and connected to the plant via flexible pipes (see Figure 4.9).

The *De-Ionizing resin (DI)* is used to remove the ionic component of the impurities: it works as ion exchanger and captures the great majority of ions dissolved in water and passing through it. For this reason, it cannot be placed in a branch where Gd ions are abundant: they would be absorbed and lost in the resin. In the GdWPS the DI is placed in the product line of NF2[2] (GDI in Figure 4.2). After two nanofiltration stages, the amount of Gd in this branch is strongly reduced and so the Gadolinium loss due to the DI is negligible. This is the key point of the GdWPS: Gd is 'removed' from water and afterwards the DI purifies Gd-depleted water from all the other ion species possibly present. Then, the de-ionized branch and the others are re-unified in the mixing tank, before being sent back to the XENONnT tank.

The other type of resin is the *Organic Removal Tank (ORT)* (GORT in the P&ID), drawn in the bottom-left part. Its important feature is that, contrary to the DI, it does not catch Gadolinium ions. Thus, it can be placed in the branch that brings the mixing tank water to the XENON tank without Gd losses. It aims to remove the residual organic compounds from the solution and has been found by EGADS to improve the water transparency [155].

The resin tanks do not have reject lines; after a period of continuous operation ($\sim$ months) they saturate and need to be replaced with new resin. Thanks to the flexible tubes which connect them to the plant, they can be easily bypassed. This is very important for test purposes, as will be described in the following Chapter.

[2]For brevity, in the following the prefix 'G' from the names of the GdWPS ultrafilters and nanofilters will be omitted.

UV lamps

UV lamps are powerful tools to kill organisms that might generate and grow inside the system. Ultraviolet light can prevent their reproduction by breaking chemical bounds. A total of six lamps are used in the GdWPS. GUV1 and GUV2 are placed in two different points of the plant; the other four (three of them in parallel) are specifically placed before the DI and ORT resins and are used for Total Organic Carbon removal (GTOC). They aim to break chemical bounds of organic compounds and make the produced ions be captured by the two resins. They constitute another source of heat to the system, motivating the need for the chiller.

In Figure 4.10, a picture of three TOC units disposed in parallel is shown.

Figure 4.9: Picture of the black tank holding the resins used in the GdWPS. The two flexible tubes on the top are the input and output lines connected to the plant.

Figure 4.10: Three UV lamp units disposed in parallel to form GTOC2. They are placed before the ORT resin.

4.1.4 Sensors

Manometers

Manometers are important to monitor the pressures in different points of the plant. In the GdWPS there are analog (GP) as well as digital (GPT) sensors (REOTEMP Series TG); these provide an electronic readout which can be readout remotely. Pressure sensors are placed before and after each pump and in other critical points (as before and

after particle filters, where a pressure drop can indicate a saturated filter that must be replaced).

Flow rate meters

KEYENCE FD-Q Series ultrasonic flow meters are used in the GdWPS to measure flows in the different branches (GF in the P&ID). They are used, in addition to the manometers, to check the correct functioning of the plant: during normal operations they must be stable. In addition, their importance enters also in the definition of separation efficiency, as can be seen in (4.2) and (4.3). They act as weights for the ion concentrations and are a relevant source of uncertainty.

Two additional flow meters, labeled as IF1 and IF2, are placed in the two pipes connecting the GdWPS to MV and NV; they are important to monitor the rate at which the overall circulation and purification in the plant happens.

One of the flow meters used in the GdWPS is shown in Figure 4.11.

Density meters

Density is another essential parameter for the GdWPS: since density increases as Gadolinium concentration increases, density meters are important to estimate the Gd concentration in the system.

In the GdWPS three Coriolis Tactical FlowMeters are used. GD1 is placed in the main branch of the plant, in the input line from the XENONnT tank (see the P&ID in Figure 4.2); GD2 is also placed in the main branch, in the return line from the mixing tank to the XENONnT tank (when operating in bypass mode this sensor is bypassed); GD3 is in the reject line of the first nanofiltration stage (NF1), where the highest concentration of Gadolinium is expected.

The functioning of these sensors relies on the Coriolis force. The fluid is made flow through a tube where a fixed vibration is externally induced. The passage of the fluid causes a modification in the tube vibration which can be detected by specific sensors. In this way it is possible to measure flow rate and density [159]. Temperature is also measured for compensation purposes. It is worth mentioning, however, that the temperature is measured in this case outside the tube and so it is not sensitive to fast variations of the fluid temperature.

Conductivity meters

Electrical conductivity is a key parameter to operate a purification plant. Pure water is known to have a relatively low conductivity, $\simeq 55\,\mathrm{nS/cm}$ at 25°C [149]. The temperature must be specified, since it strongly affects the measured value of conductivity, as also shown in [149]. For this reason, conductivity measurements are usually reported after compensating them to a fixed and standard value of temperature (25°C). With ultrapure

water its inverse, resistivity, is often adopted as unit; pure water has a resistivity of $\simeq 18.18\,\mathrm{M}\Omega \cdot \mathrm{cm}$. The non zero conductivity of pure water is caused by the dissociation occurring to H_2O molecules into $H_3O^+ + OH^-$. If ions are present in water, they increase the conductivity since they act as charge carriers. However, the relation between conductivity and concentration of each specific ion is not simple. In fact, conductivity is also affected by the mobility of each ion in the solution; this latter depends on several factors, among them the temperature, the ion species and the concentration itself (higher concentration leads to lower mobility).

The values of conductivity in different parts of the GdWPS can be used as indications on the amount of ions present in water. Operating with pure water, low values of conductivity correspond to high-purity water; when Gd salt is dissolved, they are related to its concentration. More details on this point will be given in the next Chapter.

Four METTLER TOLEDO UniCond 2E are installed in the GdWPS:

- GR1, in the reject line of NF1;
- GR2, in the product line of NF1;
- GR3, in the reject line of NF2;
- GR4, in the product line of NF2, after the DI resin tank.

Their working principle consists in applying an alternating voltage and measuring the resulting electric current. The highest value of the conductivity is expected to be measured by GR1, since it is placed in the first reject branch and thus where the highest concentration of ions is expected. GR4, on the contrary, is placed in the product line of the second nanofilter; furthermore, it is placed after the DI (as can be seen by the P&ID) which blocks most of the ions present in that branch. Hence, it is expected to show the lowest conductivity. The four sensors also provide temperature measurements that they use to make the compensation at 25°C.

One of the conductivity meters used in the GdWPS is shown in Figure 4.12.

Temperature sensors

Temperature is measured, as already pointed out, by density and conductivity sensors. Its monitoring is important since for a fast Gadolinium dissolution in water a low temperature must be kept ($\sim$ 12°C). Two additional thermometers are placed at the bottom and at the top of the mixing tank (GT1 and GT2). They are important since the mixing tank is where the Gd dissolution takes place.

Figure 4.11: Picture of one of the ultrasonic flow meters (IF2) used in the GdWPS.

Figure 4.12: Picture of one of the conductivity (and temperature) meters used in the GdWPS: GR2. It is placed in the product line of NF1.

4.2 Operations with pure water

In order to test all the different components of the GdWPS, before inserting the Gadolinium salt a long period of commissioning with pure water has been performed. Even during pure water runs, the system is able to purify water in an efficient way from different types of impurities, with the methods explained in the previous Section. The separation made by the nanofilters applies on residual ionic impurities of water, but in this case it is not helpful since all these ions must be removed to obtain clean water. From May 2022 to the end of the year the plant worked alternatively in bypass mode and connected to the XENON tank; in the meantime, a series of tests and modifications have been made, in preparation to the first Gadolinium insertion which took place in January 2023 (it will be described in Chapter 5).

The situation during May 2022 was the following. The plant was filled with demineralized water (produced with a dedicated plant used by the XENONnT experiment) and running in bypass mode. The XENON tank was being purified by the WLP. The ORT resin was not yet present; the DI resin was present but placed in the nominal position of the ORT (after UF2). This modification was made in view of the first connection of the plant to the XENON tank: without Gadolinium, the DI in the main branch (the output line back to the XENON tank) is free to remove the majority of the ions present, preserving the transparency of the water.

The first connection of the GdPlant to the XENON tank was made on July 13th; after that, the optical properties of the Neutron Veto have been checked with the Reflectivity Monitor as explained in Chapter 3. In addition to the weekly runs, more frequent runs have been acquired in critical periods in order to have a faster response. The results of the Reflectivity Monitor relative to those periods and to the whole 2022 will be reported in Section 4.2.4.

After the first connection, the plant alternated periods of connections to the water tank and periods of bypass mode, depending on the various operations carried out at different times until the end of the year. Every time the plant was running in bypass mode, the XENON tank was purified with the WLP to maintain good optical performances. At the end of 2022 the system was ready for the first insertion of Gadolinium salt.

4.2.1 Effects of the resins on resistivities

While operating with pure water, resistivity was the main parameter to express the purification performances of the GdWPS. The higher the resistivity, the purer is the water in that point. The behaviour of the four resistivity sensors when the plant is turned on is shown in Figure 4.13.

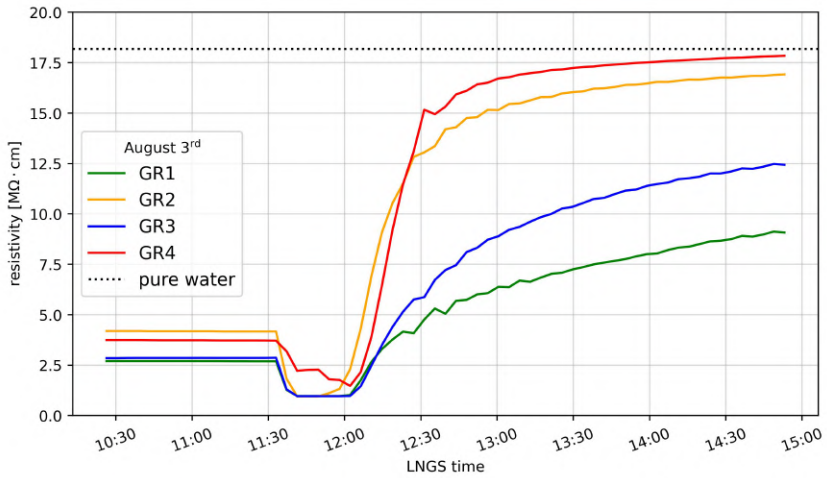

Figure 4.13: Effect,on the resistivities, of starting the GdWPS. The plant was off due to some maintenance until August 3rd at around 11:30. All the resistivities were lower than 5 MΩ · cm; after switching on (∼11:30 - 12:00) and running for few hours, the resistivities rapidly increased. GR4, in particular, reached values close to the pure water level.

Before August 3rd, the system was off for a few days due to some maintenance. The quality of water was constantly degrading, reaching values of resistivity lower than

$5\,\mathrm{M}\Omega \cdot \mathrm{cm}$ in each part of the plant. When switching on the plant (in bypass mode), the effect of the purification is clearly visible and in a few hours the resistivities reached plateau values. GR4, in particular, showed the highest values of resistivity, close to the maximum possible for pure water. The configuration of the resins was the same as before the summer: the ORT was not present and the DI was placed in the output of the mixing tank. The latter, in this way, was providing a global de-ionization; then, thanks to the separation made by the nanofilters, GR4 had a lower content of ions and GR1 the largest one, being placed in the reject of NF1. The plateau values will be shown in Table 4.1. When connecting the plant to the XENON tank, the purification was slower due to the larger amount of water circulating. In that case, the plateau values were lower (see Table 4.1) but still indicating an efficient water purification.

The ORT was inserted in the GdWPS on September 8^{th}. At the beginning a 'washing' period was needed: it was positioned right before the DI. This prevented the possible loss of impurities by the ORT to contaminate the system, since they would be trapped by the DI resin. After a few weeks in this configuration, the DI was finally moved in its nominal position: the product line of NF2. This repositioning had a visible effect on the resistivities: while when placed in the main branch the DI purified the total circulation flow of the system, in the new position only a fraction of the water passes through it at each loop. The result was a decrease of the resistivity measured by GR1, GR2 and GR3; GR4 is placed right after the DI and so did not experience any drop, remaining close to the pure water level. These behaviours are reported in Figure 4.14.

The new plateau values are reported in Table 4.1 compared to the ones in the previous conditions.

The effects of the ORT and the DI on the resistivities has been further inspected with a dedicated test. On October 12^{th} and 13^{th}, different configurations of ORT and DI have been set. First, the plant has been switched on with the nominal configuration, i.e. DI and ORT in the positions described by the P&ID of Figure 4.2. Then, the ORT has been bypassed and, after few hours of operation of the plant, the DI has been bypassed as well. The GdWPS has been kept running in this condition and at the end, both resins have been reconnected in the nominal positions. The test has been performed with the system in bypass mode. The behaviours of the resistivities during these tests are shown in Figure 4.15.

As soon as the GdWPS was switched ON, the resistivities increased approaching the equilibrium values. Bypassing the ORT, no visible effect is observed in any resistivity sensor. On the contrary, when the DI was bypassed the resistivity measured by GR4 dropped below $7\,\mathrm{M}\Omega \cdot \mathrm{cm}$, returning to $\simeq 18\,\mathrm{M}\Omega \cdot \mathrm{cm}$ right after reconnecting the DI. From this test it is clear that, while the DI has a strong impact on the resistivities, the ORT does not significantly affect them, as expected.

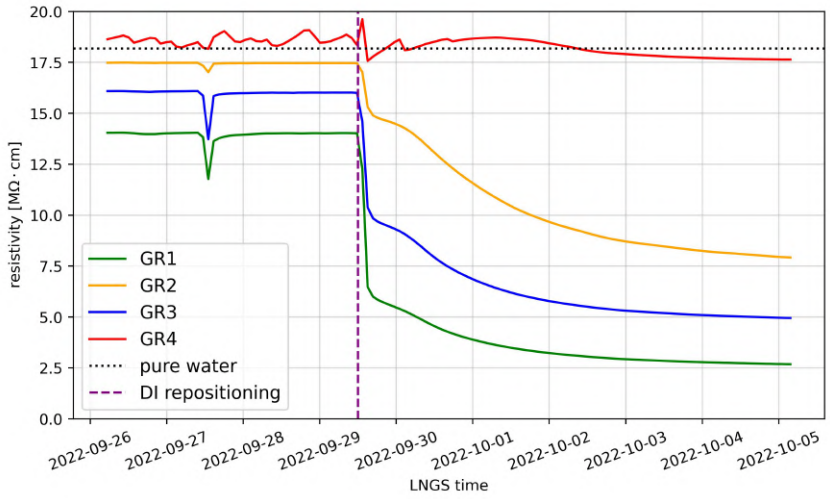

Figure 4.14: Resistivities before and after the change of DI position, happened on September 29$^{\text{th}}$. A drop is observed in GR1, GR2 and GR3 but not in GR4, placed after the DI. The values of GR4 are in some periods oscillating and higher than the pure water level: this is an indication of a noise effect, since the real value of GR4 can not be larger than 18.18 MΩ · cm.

	bypass mode, DI after UF2	**connected to XENON tank, DI after UF2**	**bypass mode, DI after NF2**
GR1 resistivity	14 MΩ · cm	9 MΩ · cm	2.5 MΩ · cm
GR2 resistivity	17.5 MΩ · cm	16.5 MΩ · cm	7.5 MΩ · cm
GR3 resistivity	16.5 MΩ · cm	12.5 MΩ · cm	5 MΩ · cm
GR4 resistivity	18 MΩ · cm	17.5 MΩ · cm	17.5 MΩ · cm

Table 4.1: Resistivities measured by the four sensors in different operation conditions of the GdWPS.

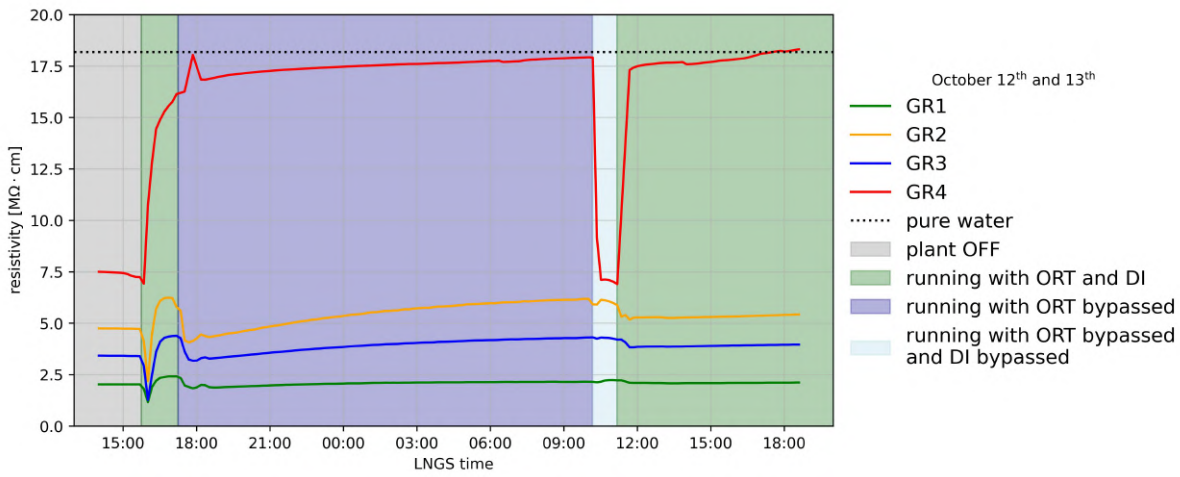

Figure 4.15: Tests on the effects of ORT and DI on the resistivities. After switching the plant ON, the ORT has been bypassed. After that, the DI has been bypassed as well and at the end the normal conditions with both ORT and DI connected has been restored. The plot suggests that the ORT does not have effects on the resistivities, while DI has a strong impact.

4.2.2 Flow rates adjustments

In preparation of the first insertion of Gd salt in the GdWPS, on November 29$^{\text{th}}$ some adjustments on the flow rates have been performed. In order to let the nanofilters perform the separation properly, the ratios between the product flow (ϕ_{prod}) and the reject flow (ϕ_{rej}) of each nanofiltration stage has to be adjusted to particular values. The ratios can be optimized only after the insertion of the Gadolinium and observing the concentrations in the different branches (maximizing the separation efficiency); however, before the insertion specific ratios have been chosen as starting points, from the EGADS experience: $\phi_{rej,1}/\phi_{prod,1} = 1$ for NF1 and $\phi_{rej,2}/\phi_{prod,2} = 1/3$ for NF2. The adjustments have been made by acting on the rejects of each nanofilter membrane; they are instrumented with separate flow meters and needle valves, as shown in Figure 4.16.

The effects of these adjustments recorded by the involved flow meters (GD3, GF4, GF5 and GF6) are shown in Figure 4.17.

After the adjustments, GD3 and GF4 were both set to $\simeq$ 13 l/min; GF5 and GF6 were instead set to $\simeq$ 3.3 l/min and $\simeq$ 10 l/min respectively.

4.2.3 Sensors calibrations

Conductivity and density are quantities of central importance in view of the addition of Gadolinium salt. For this reason, while operating the GdWPS with pure water, dedicated

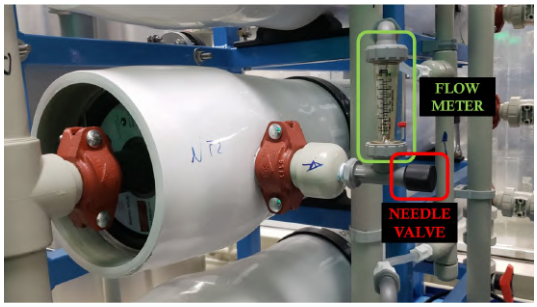

Figure 4.16: Picture of the reject line of one of the NF membranes. Each of them has a flow meter (green) and a needle valve (red) from which it is possible to adjust the flow rate.

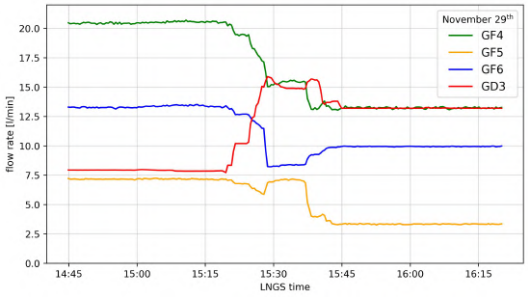

Figure 4.17: Flow rates in the products and rejects of NF1 and NF2 before and after the flow rates adjustments.

calibrations have been made for the relative sensors, in order to prepare them to the Gd insertion.

The METTLER TOLEDO conductivity meters have been calibrated on November 9^{th} and 10^{th}. A calibrated sensor brought by METTLER TOLEDO experts has been used as reference. The reference sensor has been inserted in the plant and each sensor, in turn, has been placed in series to it; both conductivity and temperature measurements have been calibrated in this way.

The density meters have been calibrated by Emerson Electric company experts at LNGS. They had to be removed by the plant and placed in a dedicated setup in series with reference sensors, brought by the experts. In this way density, flow rate and temperature measurements have been calibrated for the GdWPS sensors.

After these calibrations, the plant was ready for the first insertion of Gd salt.

4.2.4 Reflectivity Monitor during operation of the GdWPS

During all the operations carried out on the GdWPS during 2022, the Reflectivity Monitor has been used to supervise the NV performances. The analysis has been made as explained in Chapter 3.

A run for each optical fibre channel has been acquired almost weekly for the whole period; in addition, during critical steps (as the first connection to the XENON tank and the flow adjustments) Reflectivity Monitor has been used more frequently.

After the first connection, happened in July, three runs per day (per each channel) during the first three days and one run per day in the following days have been acquired. The results coming from the four channels are shown in Figure 4.18. No decrease of the time constant has been observed during this period. This suggests that connecting the GdWPS did not lead to a degradation of the NV performances.

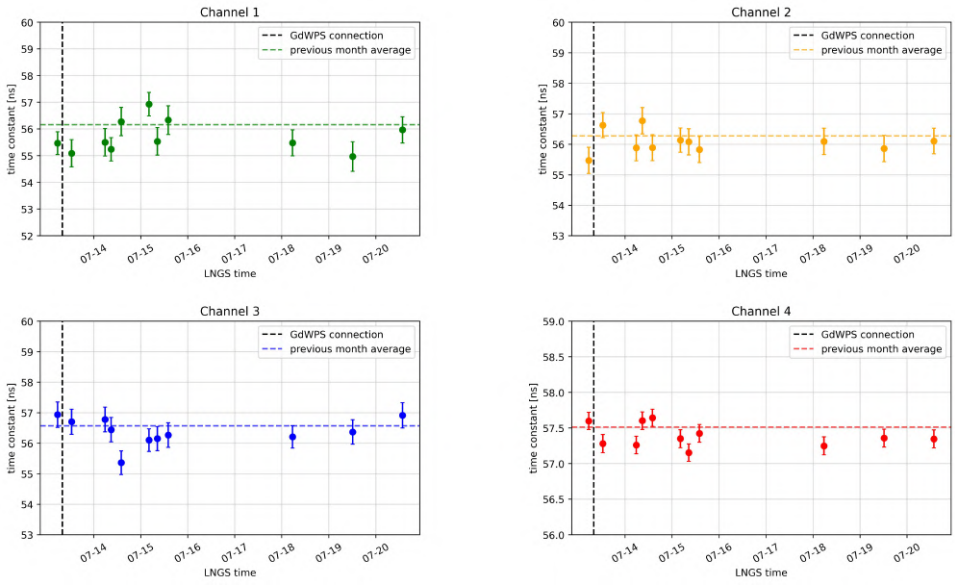

Figure 4.18: Reflectivity Monitor time constant results after the first connection of the GdWPS to the XENON tank. After days, no significant decrease is observed for any channel. In each plot, the horizontal dashed line corresponds to the average time constant measured by that channel in the previous month.

On October 27$^{\text{th}}$, after changing the positions of ORT and DI resins and performing related tests as reported in Section 4.2.1, the plant was connected to the water tank in its final configuration. The different positioning of the resins might have a strong effect on water transparency; moreover, the conditions of the GdWPS changed at the end of November when the adjustments described in Section 4.2.2 have been made. For this reason, almost a Reflectivity Monitor run per day have been taken for a long period. The runs have been taken for channel 4 only, since it was the one with smaller uncertainties and would be sensitive to a potential drop in shorter time. On December 19$^{\text{th}}$ the plant has been disconnected from the XENON tank in preparation of the Gadolinium insertion test. After that, the XENON tank has been purified by the WLP. The runs with reflectivity monitor have been taken until January 2023 The results of these runs are displayed in Figure 4.19.

No significant decrease is observed in this period.

Considering the weekly Reflectivity Monitor results of the whole year, a slight decreasing trend in the time constant is instead visible. They are reported in Figure 4.20.

In Figure 4.21 the weighted averages of the four channels are reported.

The time constant seems decreasing over time. The change is $\simeq 0.3$ ns, not dangerous for the Neutron Veto performances. We cannot see a clear correlation with any of the operations on the GdWPS.

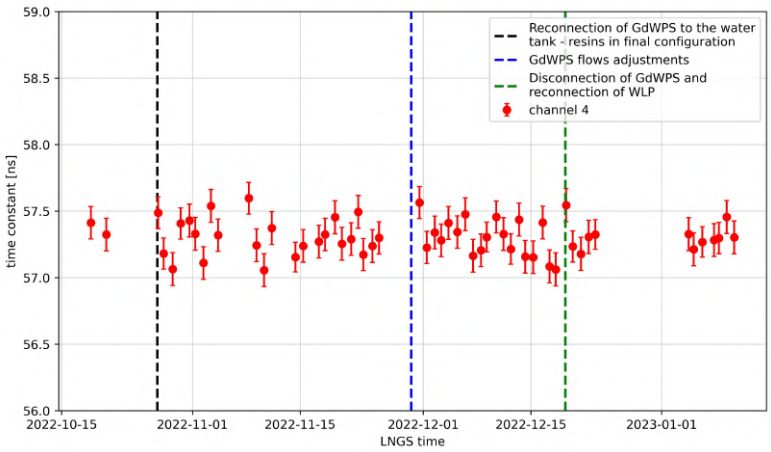

Figure 4.19: Reflectivity Monitor results, from channel 4 only, in the period between October 2022 and January 2023. The time of the connection to the XENON tank is highlighted by the black line; the flow adjustments correspond to the blue line; in correspondence to the green line, the GdWPS was disconnected from the water tank. The trend is constant over time, denoting the absence of degradation on this time scale.

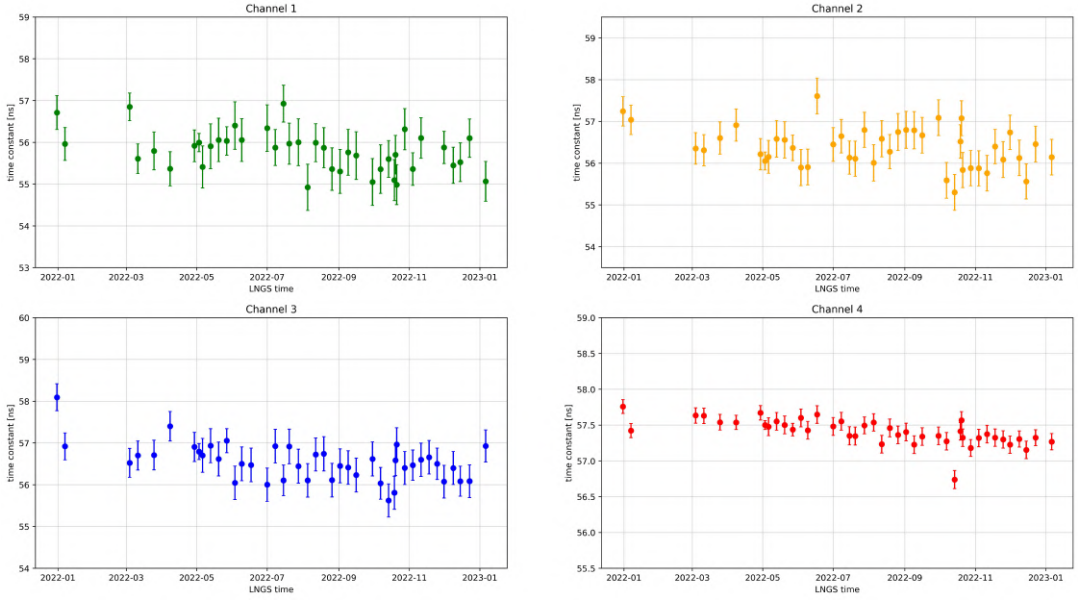

Figure 4.20: Reflectivity Monitor results of the whole 2022 for the four channels. A decreasing trend is visible mostly in channel 4, the one with the lowest errors.

A run acquired in October expresses a particularly low value of τ; this might be related operations that were ongoing in that period above the XENON tank. The drop

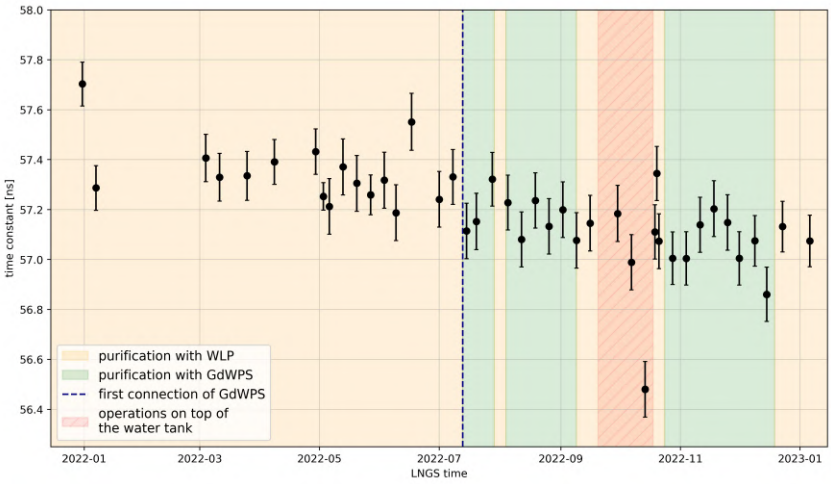

Figure 4.21: Weighted averages of the four channels results. Periods of purification with WLP and GdWPS are represented with different colours. During September and October, some operations were ongoing above the XENON tank; the corresponding period is highlighed in red. The overall trend shows a decreasing time constant.

is not confirmed by the following runs.

4.3 Transparency measurements

The Reflectivity Monitor allows to check the optical properties of the Neutron Veto over time but does not distinguish the contributions of reflectivity and transparency. Since modifications to the water purification system (as switching from WLP to GdWPS) more likely affect this latter, transparency measurements with a dedicated instrument have been carried out. A *spectrophotometer* has been utilized to measure the absorption length of different samples as a function of the photon wavelength. Samples have been collected by different points of the GdWPS and from the Neutron Veto and compared to pure water samples.

4.3.1 Experimental setup

The instrument used for the transparency measurements is a Shimadzu UV-2600i spectrophotometer integrated with a Shimadzu MPC-2600A large sample box and the LabSolutions UV-Vis software. The setup consists in two parts; in one of them, a UV lamp emits two rays with a single wavelength, one of them used as *sample ray* and the other as *reference ray*. They are directed to a sample box, where the sample ray passes through the sample to be measured while the reference one takes a different path. Both of them

are then detected by a photosensor: by comparing the two signals the instrument provides the *transmittance* of the sample. The sample is contained in a cylindrical acrylic cuvette with two quartz windows as the entrance and exit point of light. The setup is shown in Figure 4.22.

Figure 4.22: Experimental setup for the transparency measurements. Left: spectrometer (left part) connected to the large sample box (right part) where the sample is placed; top-right: interior of the large sample box, with a V-stage holding the cuvette; bottom-right: cylindrical cuvette containing the sample.

Each sample has been measured in the wavelength range 250 nm - 650 nm with 1 nm steps. The instrument automatically repeats the measurement three times for each sample; average and standard deviation of them have been calculated. The standard procedure to perform transparency measurements is the following:

1. after turning on the instrument, a baseline correction is applied (by an automatic procedure of the instrument). The baseline correction is repeated every $\sim$ 1 hour;

2. an 'air measurement' is acquired: a standard measurement but without the cuvette in the optical path; it is repeated in between each sample measurement to check the stability of the instrument and estimate its systematic uncertainty;

3. pure water measurements are acquired: pure water is taken by the LNGS Chemistry Laboratory and used as reference; it is poured in the cuvette and placed inside the large sample box. Pure water measurements are usually taken before and after each sample measurement;

4. the samples are poured in turn into the cuvette and their transparency is measured.

Since this measurement aims at achieving the highest accuracy, each step must be done with particular caution. The presence of bubbles inside the cuvette must be avoided and it has to be washed with de-mineralized water before and after each sample measurement.

4.3.2 Transmittance model

The raw results provided by the instrument, for each measurement and wavelength, is a transmittance: the % of the emitted light detected by the PMT. This quantity is related to the absorption of each sample; anyway, obtaining the absorption length from the transmittance is not straightforward, since there are several factors to take into account.

First of all, when a photon encounters a surface between different materials, it has a given probability to be reflected back. The reflection and transmission probabilities are described by the Fresnel equations; during these transparency measurements, photons are directed perpendicularly to each surface, so the incident angle is always (approximately) 0°. In this case, when a photon traveling in a medium with refractive index n_1 strikes the interface with another medium with refractive index n_2, the probability to be reflected is

$$R = \frac{(n_1 - n_2)^2}{(n_1 + n_2)^2}\,. \tag{4.4}$$

In the transparency measurements setup, photons travel five different media before reaching the PMT where they are detected. At each surface, they can be reflected back with the probability expressed in (4.4). A schematic representation of the light behaviour is given in Figure 4.23.

In addition to the surface effects, while traveling inside the quartz windows or through the sample photons can be absorbed (absorption in air is negligible). When photons travel a distance x in a medium with absorption length ℓ_{abs}, the probability to be absorbed is $1 - e^{-x/\ell_{abs}}$. Photons can also elastically scatter (Rayleigh scattering) and be deflected out of their path; in this case, even if they are not absorbed, they cannot be detected by the PMT. A corresponding scattering length ℓ_{scatt} can be associated to each medium. In total, the probability for a photon to be absorbed or scattered while traveling a distance x is $1 - e^{-x/\ell_{abs} - x/\ell_{scatt}}$. The transparency measurements aim to find ℓ_{abs}, since in the Neutron Veto scattered photons are not lost and can be detected. However, the scattering component is unavoidable: the final absorption length result will be interpreted as a lower bound.

A sample under measurement is characterized by an attenuation length ℓ_s, which accounts for both absorption and scattering ($1/\ell_s = 1/\ell_{abs} + 1/\ell_{scatt}$). It is assumed that its refractive index is approximately equal to the water refractive index (n_w). Quartz, in turn, will have a total attenuation length ℓ_q and a refractive index n_q. Air absorption and scattering can be neglected; the refractive index of air is labeled as $n_a (\simeq 1)$. The

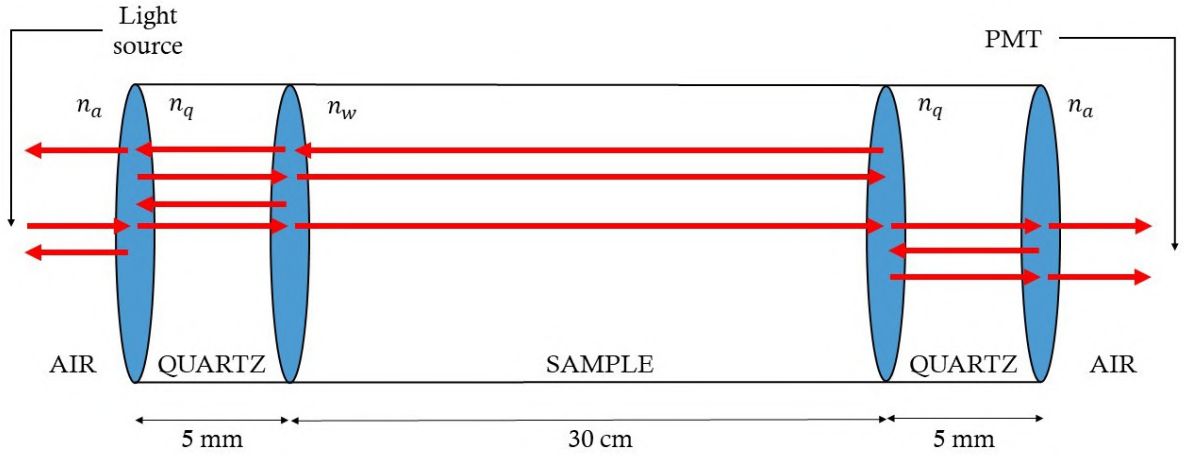

Figure 4.23: Schematic representation of the cuvette holding a sample during a measurement. The photons, arriving from the light source on the left, encounter five different media: air, quartz, sample, quartz, air. At each interface they can be reflected with a probability that depends on the refractive indices of the two involved media. Refractive indices of air and quartz are denoted as n_a and n_q; the sample refractive index can be approximated as the one of pure water, n_w.

fraction of light emitted at one side of the cuvette that reaches the other side is the sum of infinite contributions: each photon can be repeatedly reflected by the surfaces and reach the other end in different ways (see Figure 4.23)[3]. Every time a photon hits an air-quartz surface it has a probability to be reflected (R) and one to be transmitted (T), given by

$$R_{aq} = \frac{(n_a - n_q)^2}{(n_a + n_q)^2} \quad , \quad T_{aq} = 1 - R_{aq} \tag{4.5}$$

and independent of the photon direction. The same happens for all the quartz-sample interfaces, where

$$R_{qs} = \frac{(n_q - n_w)^2}{(n_q + n_w)^2} \quad , \quad T_{qs} = 1 - R_{qs}\,. \tag{4.6}$$

Moreover, every time a photon crosses a quartz window of length ℓ, the probability to be absorbed or scattered is $1 - e^{\ell/\ell_q}$; in analogy, each time it crosses the sample contained in the cuvette which has length L, the probability to be lost is $1 - e^{L/\ell_s}$. As shown in Figure 4.23, $\ell = 5\,\text{mm}$ and $L = 30\,\text{cm}$.

Using these conventions, it can be proved that the probability for a photon to cross

[3]Higher orders contributions, where the photon is reflected more and more times by the surfaces, are less important. Hence, an approximation is possible.

a single quartz window is [160]

$$T_0 = \frac{T_{aq} T_{qw} e^{-\ell/\ell_q}}{1 - R_{aq} R_{qw} e^{-2\ell/\ell_q}} \,. \tag{4.7}$$

The probability to cross the whole cuvette (with whatever combination of reflections and transmissions), i.e. the transmittance, is given by:

$$T_s = \frac{T_0^2 e^{-L/\ell_s}}{1 - (1 - T_0)^2 \, e^{-2L/\ell_s}} \,. \tag{4.8}$$

The parameter of interest ℓ_s can be derived by the transmittance noticing that T_1 is independent of ℓ_s and taking the ratio between the transmittance of the sample and the transmittance of a pure water sample. This latter will be characterized by the absorption (plus scattering) length ℓ_w.

When the refractive indices involved do not strongly differ by each other (as in the case of air, water and quartz), the reflection probability R written in (4.4) is close to zero (for $n_1 = 1$ and $n_2 = 1.5$ one gets $R = 0.04$). In the approximation $R \ll 1$, the ratio between the transmittances of a generic sample and a pure water one is given by:

$$\frac{T_s}{T_w} \simeq \frac{e^{-L/\ell_s}}{e^{-L/\ell_w}} \,. \tag{4.9}$$

The parameter of interest ℓ_s can be then estimated as

$$\ell_s = \left[\frac{\log\left(T_w/T_s\right)}{L} + \frac{1}{\ell_w} \right]^{-1} \,. \tag{4.10}$$

In this way, measuring the transmittances of pure water T_w and of a sample T_s and knowing L and ℓ_w, it is possible to simply derive ℓ_s. The approximation that have been applied is very useful, since it allows to ignore the effects of internal reflections making them cancel out.

4.3.3 GdWPS samples measurements

On October 25$^{\text{th}}$ and 26$^{\text{th}}$ transparency measurements of different samples taken from the GdWPS have been performed. Eight different types of measurements have been carried out:

- air measurements: performed between each measurement in order to check the stability of the instrument and estimate the error;
- pure water measurements: taken from LNGS Chemistry Laboratory, it has been used as reference for the other samples;

- measurement of a sample from UF1 product line;
- measurement of a sample from UF2 product line;
- measurement of a sample from NF1 product line;
- measurement of a sample from NF2 product line;
- measurement of a sample from the DI output;
- measurement of a sample from the Neutron Veto (collected through a dedicated sampling pipe reaching the inner part of the detector).

It is worth mentioning that, while from ultrafilters and nanofilters product lines and the Neutron Veto there are dedicated sampling points, the sample from the output of the DI has been taken after stopping the GdWPS. This might lead to some systematic difference.

Air measurements

All the air measurements acquired during the two days are represented in Figure 4.24.

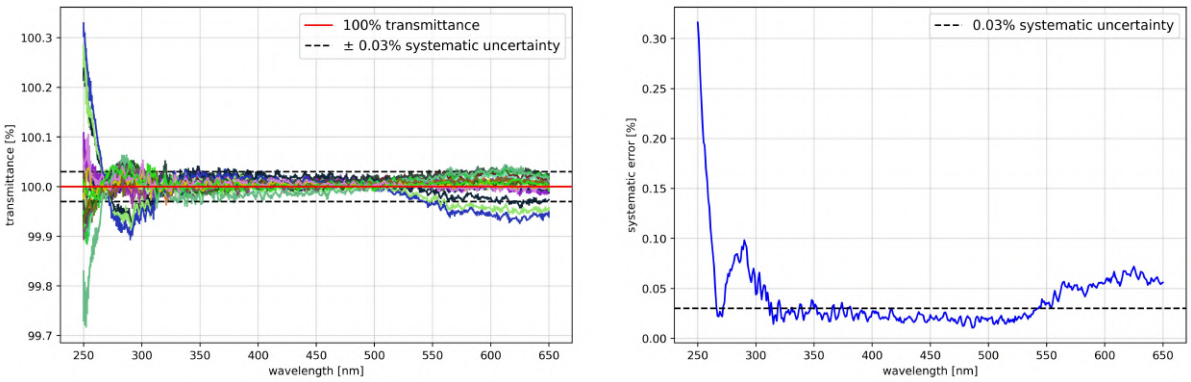

Figure 4.24: Left: transmittance as a function of photon wavelength from the air measurements of October 25th and 26th. All the measurement are close to the expected 100%, except for some fluctuations at low and high wavelengths. Right: maximum deviation from 100% as a function of the wavelength.

A total of 20 measurements of this kind have been acquired. The expected result is 100% transmittance at every wavelength and deviations from such result provide estimates of the repeatability of the measurement. From the plot, it is visible that all the measurements are close to what expected, with no clear bias; moreover, the dispersion is mostly lower than the nominal systematic error of the instrument (0.03 %). On the left

in Figure 4.24 are shown the maximum deviations from 100% transmittance as a function of the wavelength. In the region of interest, from 300 nm to 500 nm, the systematic deviations are compatible with 0.03 % which can be so considered a good estimate of the systematic uncertainty.

Pure water measurements

A total of 5 measurements of pure water samples have been acquired during the two days. The results are reported in Figure 4.25.

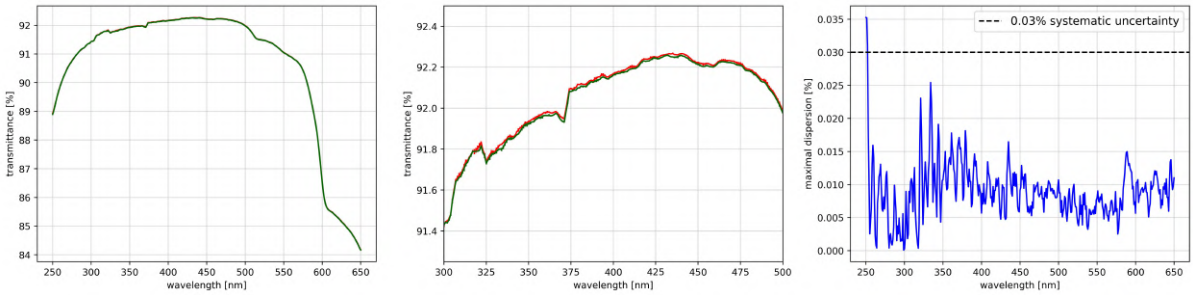

Figure 4.25: Left: transmittance as a function of photon wavelength in the whole spectrum for pure water measurements. Center: zoom in the region of interest. Right: maximum dispersion within different runs for each wavelength. The dispersions are below the systematic error.

The different runs express high repeatability, resulting in a solid result for the transmittance of pure water. The average between them has been used in the following for the analysis of the samples.

Samples measurements

In Figure 4.26 are shown the results, in terms of transmittance, of the six samples collected from the GdWPS and the Neutron Veto. The average result of the pure water measurements is also shown for comparison.

Absorption length estimations

For each sample, it is possible to estimate the relative absorption length by (4.10). T_w and T_s directly come from the measurements; L is considered as 30 cm; for ℓ_w, some assumptions have to be made. A recent study [148] measured the absorption length of pure water in the visible and near UV range: in the region of interest between 300 nm and 500 nm the absorption length is $\gtrsim$ 100 m, reaching a maximum of $\simeq$ 1 km around 350 nm (see Figure 4.27).

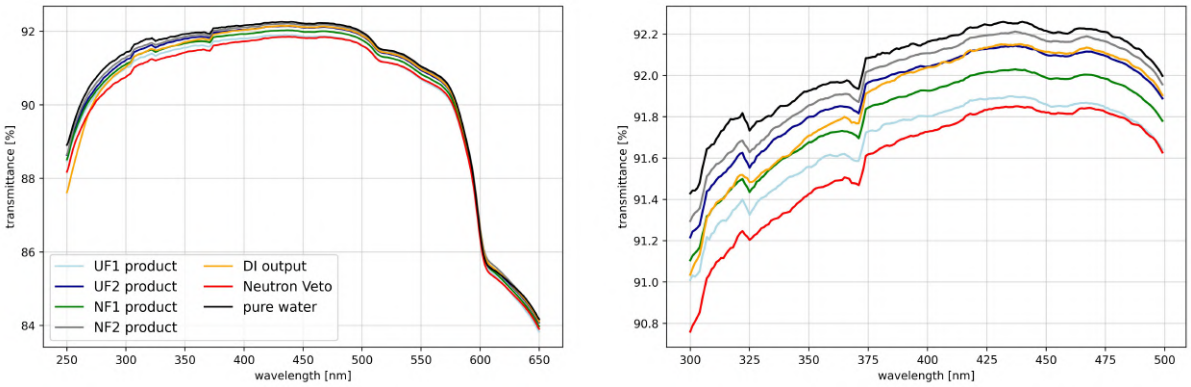

Figure 4.26: Left: transmittance of the different samples as a function of photon wavelength in the whole spectrum, for the different samples and pure water. Right: zoom in the region of interest.

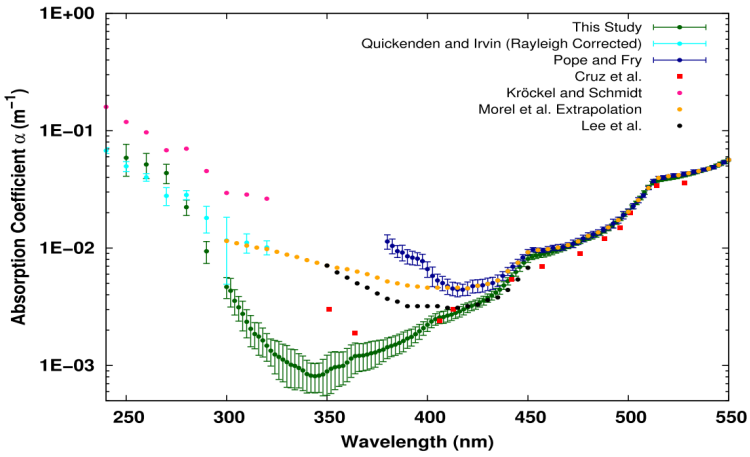

Figure 4.27: Absorption coefficient (the inverse of the absorption length) of pure water, from [148]. In the region between 300 nm and 500 nm the coefficient is $< 10^{-2}\,\mathrm{m}^{-1}$, corresponding to an absorption length > 100 m.

It is not guaranteed that the pure water taken as reference in the transparency measurements has the same absorption length of the one used in [148]. To infer the absorption lengths of the GdWPS samples with (4.10) a constant ℓ_w equal to 100 m for every wavelength has been assumed. In this way, the absorption lengths of all the samples have lower limits (considering the Rayleigh scattering) of tens of meters, as shown in Figure 4.28. All the samples have an absorption length larger than 70 m in the region of interest.

From the plot it can be seen that the Neutron Veto sample has the lowest transparency: all the samples taken from the GdWPS have a larger absorption length. Among

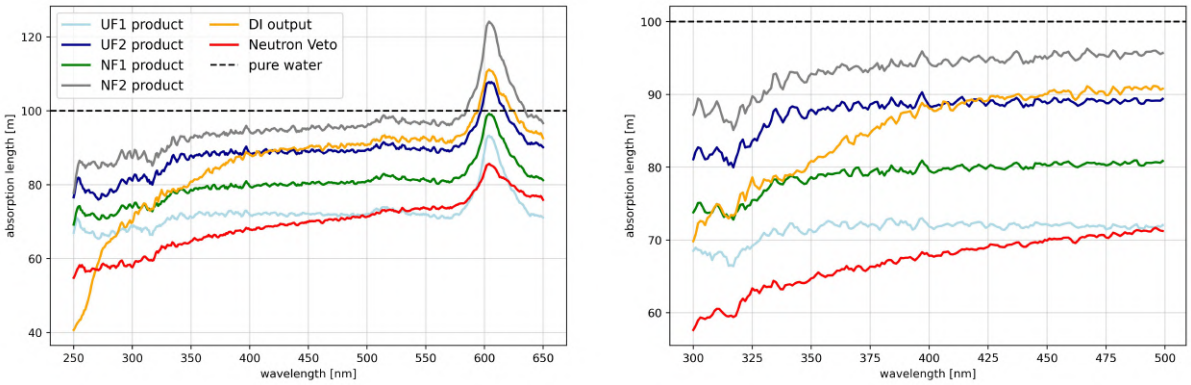

Figure 4.28: Absorption lengths estimates of the different samples. On the right, a zoom on the region of interest. The absorption length of pure water is assumed to be 100 m. The peak near 600 nm is not physical and due to the high slope of the transmittance curves (see Figure 4.26 (left)) which is source of uncertainty.

them, the one taken from the product of NF2 is the most transparent. The sample taken after the DI resins has an anomalous behaviour with respect to the others; moreover, it was expected to be more transparent than the product of NF2 since it is further purified by the DI resin. These differences might be due to the different sampling mode: as already said, to collect the DI sample the plant had to be turned off.

When the samples were taken, the GdWPS was in bypass mode; in this configuration, the sample which best represents the system is the one in the product of UF1: it is in the main branch and after the ORT resin. It is the one with the lowest absorption length among the samples measured, but still higher than the Neutron Veto one at the time.

Comparing the results of the samples from UF1 and UF2, the latter provides a better result. The ORT, placed in between the two ultrafilters, does not show an improvement of water transparency.

Chapter 5

Gadolinium first insertion test

After operating the GdWPS with pure water and testing its different components, in January 2023 the first insertion of Gadolinium sulfate has been performed. The plant operated in bypass mode and the salt has been added in steps. Preliminary measurements have been done before the insertion to quantify the expected response of the system.

The purposes of this test were multiple. First, the Gadolinium insertion system described in Section 4.1.2 needed to be tested: the time required by the transfer system to insert the salt in the mixing tank and the one taken by the stirrer to dissolve it are particularly relevant during regular operation; moreover, the ability to prevent the salt from sticking in the hopper, in the flexible tube or in the pneumatic system needed to be verified. Once the Gadolinium salt is dissolved, it is also important that the plant allow monitoring its concentration; it can be done 'offline' by taking samples, but the possibility to do it 'online' is a relevant feature to be tested. Finally, the test aimed to estimate the separation efficiencies of the nanofilters, crucial parameters during standard operations.

5.1 Preliminary measurements

The offline measurement of Gadolinium concentration can be performed with the *Inductively Coupled Plasma-Mass Spectrometry (ICP-MS)* [161] at the LNGS Chemistry Laboratory, applied on samples previously collected on the GdWPS. This constitutes the most precise tool for this purpose; however, the collection of the samples and the measurement procedure requires time and cannot be done continuously. Finding a way to estimate it online, even if with lower accuracy, can help in understanding in real time the behaviour of the plant.

For this reason, prior to the Gadolinium insertion, two calibrations have been made at the LNGS Chemistry Laboratory. Electrical conductivity and density are the two quantities measured online in the GdWPS that are mostly affected by the presence of

Gadolinium. Hence, their dependencies on Gd salt concentration have been investigated.

In what follows, Gadolinium concentration will always refer to the concentration in mass of Gadolinium sulfate octahydrate, $Gd_2(SO_4)_3 \cdot 8H_2O$. The nominal concentration in these terms is so 0.5 %.

5.1.1 Conductivity calibration

The presence of Gadolinium salt dissolved in water, which dissociates in Gd^{3+} and SO_4^{2-} ions, produces an increase of conductivity. In general, the dependency of conductivity on the concentration of a given ion species is not simple to derive; at low concentrations, it is almost linear, but reaching higher concentrations the effect of the reduced ion mobility becomes relevant, resulting in a lower increase of conductivity for the same concentration increase.

A calibration has been made to characterize the behaviour of Gd-water conductivity as a function of its concentration. A Gadolinium-water solution has been prepared at LNGS Chemistry Laboratory and diluted several times in order to obtain ten solutions with different concentrations, ranging from 5 to 5000 parts per million (ppm). For each of them, the conductivity has been measured by a METTLER TOLEDO instrument (see Figure 5.1). A calibration curve has been built, fitting the results with a power law of the form:

$$\sigma = A \cdot c^B \tag{5.1}$$

where σ is the conductivity, c the concentration and A and B two free parameters. The results of the fit are shown in Figure 5.2.

Data fit well with a power law. The parameters A and B have been found to be $A = 2.255 \pm 0.005\,\mu\mathrm{S\,cm^{-1}\,ppm^{-1}}$ and $B = 0.743 \pm 0.004$. Inverting (5.1), one can derive the Gadolinium concentration once measured the conductivity. Applying this method in the GdWPS, one should take into account that other ions dissolved in water, if present, would contribute to the conductivity. However, the amount of ions present in the GdWPS while running with pure water was very low, providing a maximum conductivity of $\simeq 600\,\mathrm{nS/cm}$, while the solution prepared at the nominal concentration of 5000 ppm showed a much larger conductivity of more than $1200\,\mu\mathrm{S/cm}$.

5.1.2 Density calibration

Differently from conductivity, the density increase caused by Gadolinium insertion is small and almost linear. A similar procedure to the one explained in the last Section has been made for density; however, density measurements are much harder and less precise than conductivity measurements.

The instrument used at the Chemistry Laboratory was a pycnometer (see Figure 5.3). Its functioning relies on precise mass measurements: its volume is provided with high

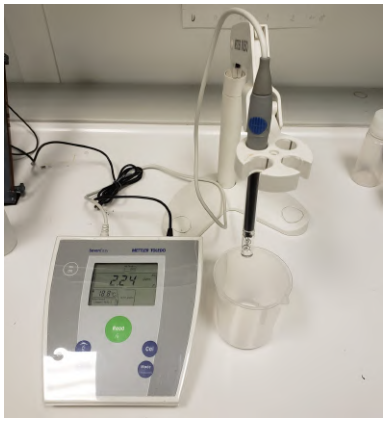

Figure 5.1: Picture of the METTLER TOLEDO conductivity sensor used, at LNGS Chemistry Laboratory, to measure conductivities of the Gd-water solutions prepared at different concentrations.

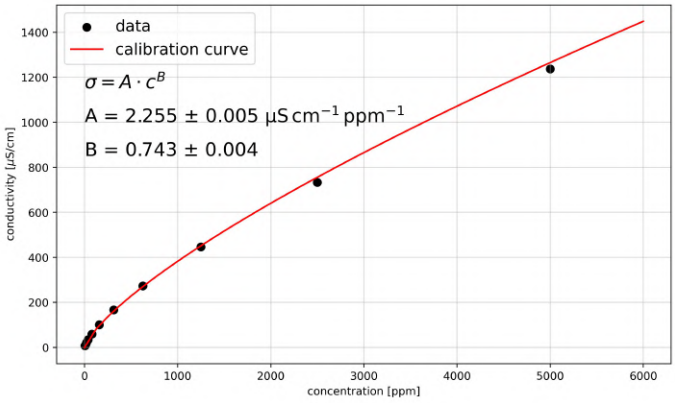

Figure 5.2: Results of the conductivity calibration. Data have been fitted with the power law in (5.1). The parameters obtained are $A = 2.255 \pm 0.005\,\mu\mathrm{S\,cm^{-1}\,ppm^{-1}}$ and $B = 0.743 \pm 0.004$.

precision by the factory and, after filling it with the solution under measurement and weighting it, density is directly calculated dividing the mass by the volume.

Four solutions have been prepared for this calibration; for each of them repeated measurements have been taken to reduce the uncertainties. The four concentrations were 0 % (pure water), 0.25 %, 0.5 % (nominal concentration) and 1 % (double of nominal concentration). The results are shown in Figure 5.4. The data have been fitted with the linear curve:

$$\rho = \rho_w + k_\rho \cdot c \tag{5.2}$$

where ρ_w is the pure water density and k_ρ a parameter expressing the amount of density increase.

The absolute value of density is, as well as conductivity, temperature dependent. The density meters used by the GdWPS do not perform a temperature compensation; however, the important observable during the addition of Gadolinium is more properly the density variation. For this latter, the contribution of temperature can be neglected (considering that temperature is almost constant while the GdWPS is running).

Looking at the results reported in Figure 5.4, it can be seen that going from pure water to 0.5 % the density of Gd-water solution is expected to become $\simeq 0.0038$ kg/l higher, an increase of less than 4 per mil. Conductivity, on the contrary, changes by three orders of magnitude (going from $\sim$ µS/cm to $\sim$ mS/cm). For this reason, the

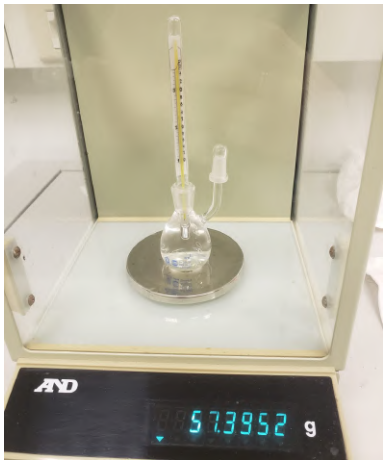

Figure 5.3: Picture of the pycnometer placed on a high precision scales at the LNGS Chemistry Laboratory, used to measure the density of solutions at different concentrations.

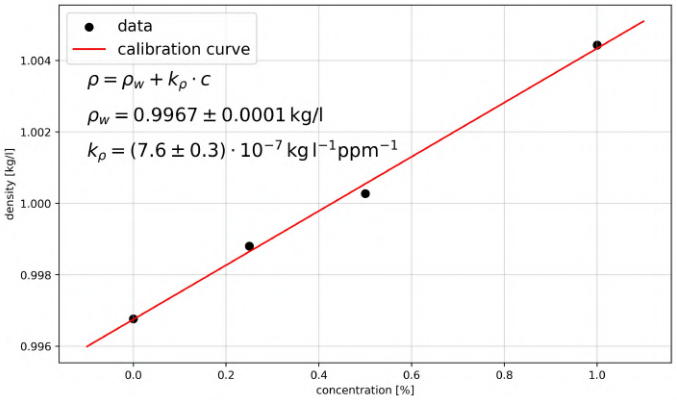

Figure 5.4: Results of the density calibration. The dependency on the concentration is linear. The offset (pure water density) is measured to be $\rho_w = 0.9967 \pm 0.0001$ and the slope is $k_\rho = (7.6 \pm 0.3) \cdot 10^{-7}\,\mathrm{kg\,l^{-1}ppm^{-1}}$.

latter is expected to provide more precise estimations of the Gadolinium concentration.

5.2 Insertion of Gadolinium salt

Before inserting Gadolinium sulfate in the system for the first time, the DI was bypassed; this was crucial in order to make Gadolinium circulate in the GdWPS without being captured by the resin. The plant was left in bypass mode in order to stay isolated from the XENONnT water tank and make the Gd-water circulate in a closed loop. The insertion was planned to be carried out in three steps:

1. the first insertion of 1 kg of salt;
2. a second insertion of other 4 kg of salt, reaching a total of 5 kg;
3. the last insertion of 5 kg, reaching a total of 10 kg of salt.

In this way, 10 kg of Gd salt would be present in the system; considering that the mixing tank contains 2 tons of water and neglecting the mass of water contained in the rest of the plant (in the pipes, filter and resin holders), that would correspond to 0.5 % concentration in mass, the nominal one. The exact amount of this additional water content was unknown before the test. However, as will be shown, after these three steps

this contribution turned out to be relevant: the total water mass contained in the system has been estimated to be around 3 tons. For this reason, other 5 kg of salt has been added in order to reach the 0.5 % concentration.

All the insertions have been made following the procedure described in Section 4.1.2. The transport and transfer systems worked well and no problem was encountered. After turning on the pneumatic system, the great majority of salt contained in the hopper has been moved to the mixing tank in less than 5 minutes. After dropping the salt in the mixing tank (Figure 5.5 (left)), the stirrer was turned on (Figure 5.5 (right)) and able to dissolve the salt in 30 minutes, when the transparency of the mixing tank water was re-established.

Figure 5.5: Left: drop of the first kilogram of Gadolinium salt inside the mixing tank. Right: activation of the stirrer which mixes the solution. Pictures taken from a lateral window placed on the mixing tank.

The plant has been kept off during the insertion and dissolution, with the mixing tank isolated from the rest of the system. As soon as the salt was dissolved, the input and output lines of the mixing tank have been opened and the GdWPS switched on again. In a few minutes, the conductivities measured by the four sensors started increasing. In Figure 5.6 (left) is reported this increase after the first insertion. In Figure 5.6 (right)

are reported the corresponding Gd concentrations, estimated with the calibration curve introduced in Section 5.1.1. Among the four sensors, GR1 is the one showing the greatest increase, as expected: placed in the reject line of NF1 it contains a larger Gadolinium concentration than the average solution. All the others are placed after at least one nanofiltration stage; GR4, being placed in the product of NF2, was expected to show a relatively low conductivity increase. GR3 reached the full scale of the analog readout that was set to 50 μS/cm (the real value provided by the instrument was not much higher, $\simeq$ 52 μS/cm); its readout range has been enlarged afterward.

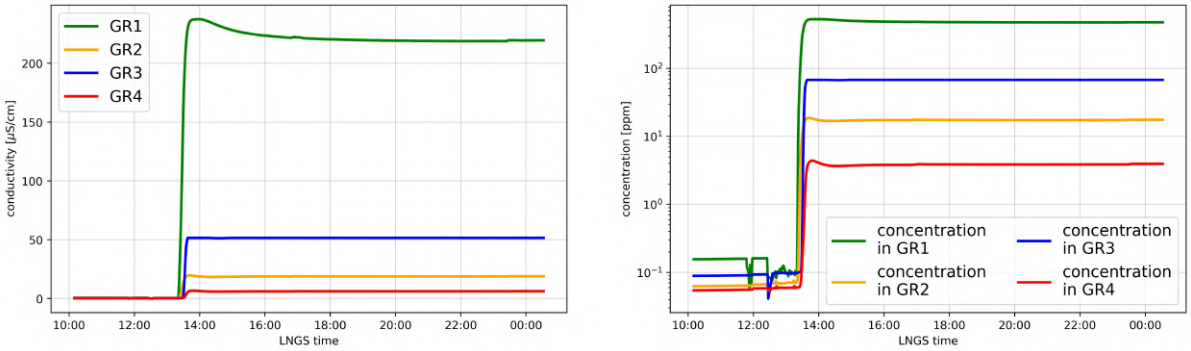

Figure 5.6: Left: conductivities increase in the four sensors of the GdWPS after the first insertion of Gd salt. Right: corresponding estimations of the concentrations increase in the four points of the plant. As expected, in the product line of NF2, where GR4 is placed, the concentration is the lowest.

Concerning the densities, only two sensors were available during the test since GD2 is placed outside the loop when the plant runs in bypass mode (see Figure 4.2). GD1, placed in the main branch, feels the average concentration of Gd salt; GD3 is instead placed in the reject line of NF1, in the same branch of GR1. After the addition of the first kg of salt, only this latter experienced an increase, as shown in Figure 5.7.

Before the insertion, the two sensors measured different values of density even if working with pure water. This systematic shift was however not dangerous since in the GdWPS we are not interested in an absolute measure of density, but rather to be sensitive to density variations. After the first insertion, the value of GD3 passed from $\simeq$ 998 g/l to $\simeq$ 998.5 g/l. GD1, on the contrary, did not show a clear increase: the concentration in the main branch was not high enough to make the sensor sensitive to the difference.

5.2.1 Concentration monitoring with ICP-MS

After each step of the insertion procedure, the plant has been run for enough time to reach equilibrium. During those periods, the values of density and conductivity in the

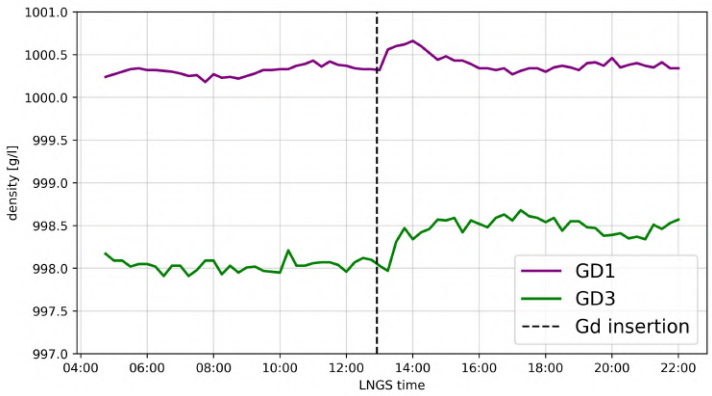

Figure 5.7: Density increase after the insertion of the first kilogram of Gadolinium salt. While GD1 is not sensitive to this concentration, GD3 already shows a small increase.

various branches always showed good stability, suggesting a uniform dissolution of the salt in water. Samples have been taken each time, from different positions across the GdWPS, and the ICP-MS technology has been used to measure with high precision the concentrations. On the same samples independent conductivity measurements have also been performed.

It is useful to refer to the P&ID of the GdWPS on the point of view of the nanofiltration stages and of the different branches with different Gadolinium concentrations, as shown in Figure 5.8.

The conductivity in the main branch (purple in Figure 5.8) is not measured directly on the plant. It has been labeled as 'GRtot' and can be measured only on the samples or indirectly by averaging GR1 and GR2. However, as discovered by the calibration exposed in Figure 5.2, conductivity does not grow linearly with the number of ions. To average GR1 and GR2 it is necessary to first convert them to concentrations, using the calibration curve. Then, the concentration can be averaged using the flow rates as weights. Once obtained the concentration in the main branch, GRtot is obtained by converting it to a conductivity, again with the calibration curve.

After the first insertion, three samples has been taken from the plant: one from the product of UF1 (main branch), one from the reject of NF1 (where GR1 is placed) and one from the product of NF2 (where GR4 is placed). Except for the first one, the plant had to be stopped right before the sampling.

After the second insertion, with a total of 5 kg of salt in the system, the same samples have been taken and, in addition, another one directly from the mixing tank.

After the third insertion, in addition to the three usual samples, two samples have been collected from the output line of each nanofiltration membrane that constitute NF2 (NF2a and NF2b). For them, there was no need to stop the GdWPS.

The results relative to the three conditions are reported in Figure 5.9.

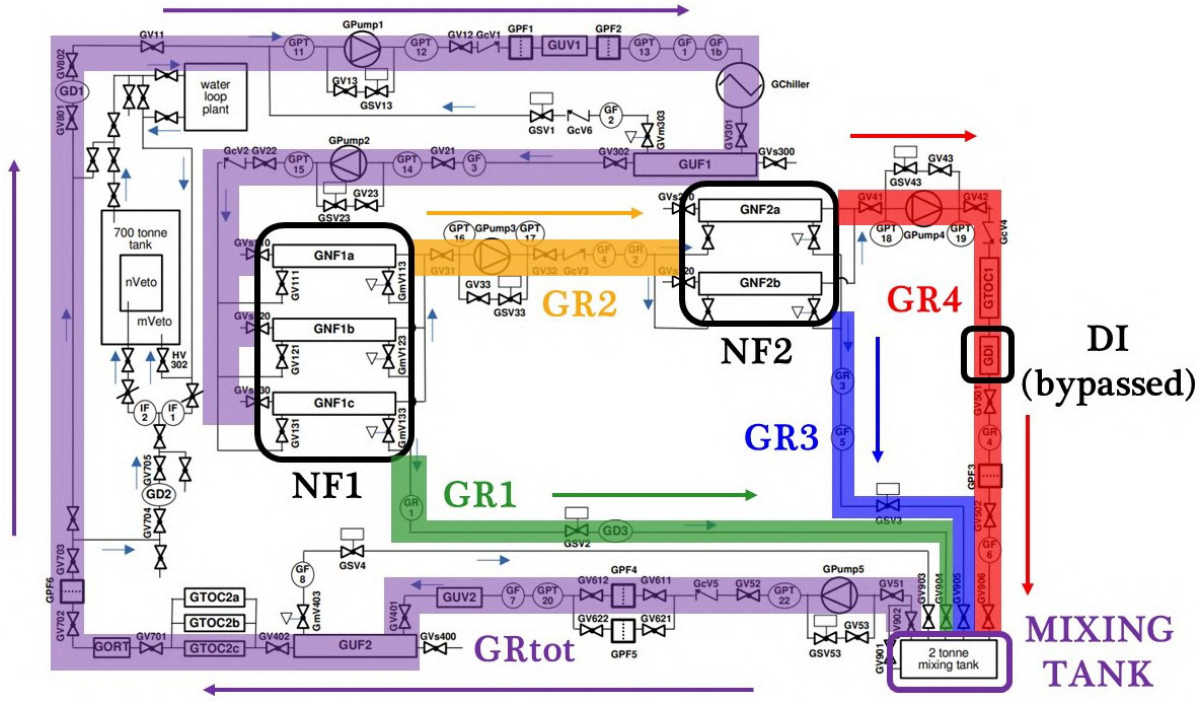

Figure 5.8: P&ID of the GdWPS where components relevant during the Gd insertion and relative measurements have been highlighted. With different colours are represented the main branch of the plant (purple), the high concentration branch where GR1 and GD3 are placed (green), the branch hosting GR2 (orange), the one hosting GR3 (blue) and the one with the lowest concentration, where the DI is bypassed and the conductivity is measured by GR4 (red).

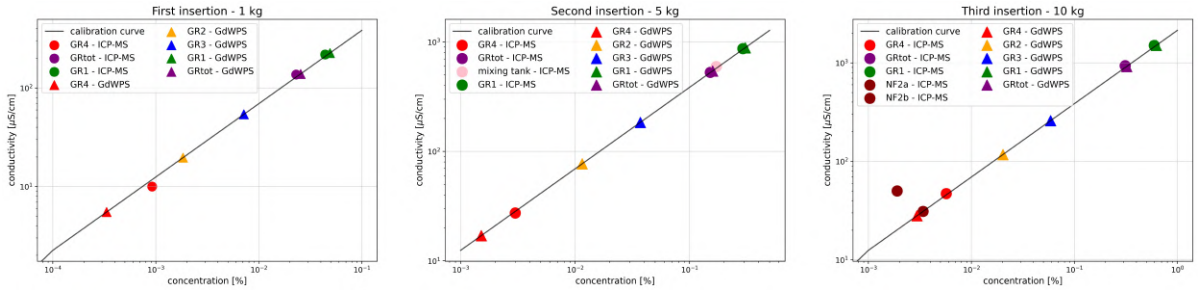

Figure 5.9: Conductivities and concentrations after different insertion steps. The black line represents the calibration curve. The triangles report the conductivities measured on the GdWPS on the calibration curve. The circles represent the two independent measurements of conductivity and concentration made on the samples.

In the plots, the black line is the calibration curve found before the Gd insertion. The triangles represent the conductivities measured on the plant in the different configurations; they have been reported on the calibration curve, but it should be remembered that the concentration is not measured directly. The circles are instead the measurements coming from the samples; they consist of two independent measurements of concentration (through ICP-MS) and conductivity (with the conductivity meter at the Chemistry Laboratory) and the fact that most of them lie on the calibration curve is a good confirmation that the calibration curve is a reliable tool to monitor the GdWPS.

The ICP-MS provides the concentrations of the single isotopes. The values from different Gd isotopes have been averaged and using its stoichiometric fraction in the Gadolinium sulfate octahydrate the concentration of the salt has been calculated. In this way, all the concentrations refer to the molecular one.

The samples at high concentration, the ones taken in the main branch (purple) and in the NF1 reject line (green), show good agreement between measurements on the plant and offline. The directly comparable value is the conductivity, which has negligible differences. The concentrations are only measured by ICP-MS and provide results consistent with the expectations derived from the calibration curve. The sample taken from the mixing tank is similar to the UF1 product, as they are both on the main branch with the average concentration.

The samples taken from the NF2 product line show instead some discrepancy. The conductivities measured on the samples are, after the first two insertions, larger than the one measured online on the GdWPS (almost twice as much). A possible explanation for this disagreement is the sampling procedure: stopping the system the filters do not work properly and it is possible that the amount of ions in the branch with GR4 is enhanced. For this reason, after the third insertion, it has been decided to collect the additional samples from the product of each individual membrane, without switching off the plant. As can be seen from the right panel in Figure 5.9, this new sampling procedure provides more consistent results. There is still a difference between the concentrations in GR4 indirectly calculated by the plant ($\simeq$ 30 ppm) and directly measured by ICP-MS on the sample taken after stopping the plant ($\simeq$ 57 ppm). The average between the concentrations in the two NF membranes ($\simeq$ 26.5 ppm), found on the samples collected without stopping the plant, is instead similar to the one obtained by GR4, even if the conductivity of one of the two samples is larger than expected and deviating from the calibration curve.

The concentrations measured by the plant and by ICP-MS after each insertion step are summarized in Table 5.1.

Looking at the concentrations reached with 10 kg of Gd salt inside the GdWPS ($\simeq$ 3000 ppm in the main branch), it is clear that the total mass of water contained by the plant is larger than 2 tons. The real amount can be estimated by looking at the concentrations as a function of the mass of Gadolinium salt dissolved in the system, as in Figure 5.10.

		GR1	GR2	GR3	GR4	GRtot
1 kg	**GdWPS**	503 ppm	18 ppm	72 ppm	4.5 ppm	260.5 ppm
	ICP-MS	440 ppm	N.A.	N.A.	9.2 ppm	230 ppm
5 kg	**GdWPS**	3062 ppm	116 ppm	370 ppm	15 ppm	1589 ppm
	ICP-MS	2919 ppm	N.A.	N.A.	30 ppm	1514 ppm
10 kg	**GdWPS**	6300 ppm	230 ppm	713 ppm	30 ppm	3265 ppm
	ICP-MS	5957 ppm	N.A.	N.A.	57 ppm	3109 ppm

Table 5.1: Comparison between concentrations in the different branches of the GdWPS after different steps of Gadolinium insertion, obtained from the GdWPS conductivities and ICP-MS. For consistency, the ICP-MS concentration of GR4 after 10 kg is reported by the sample collected after stopping the plant and not from NF2a and NF2b.

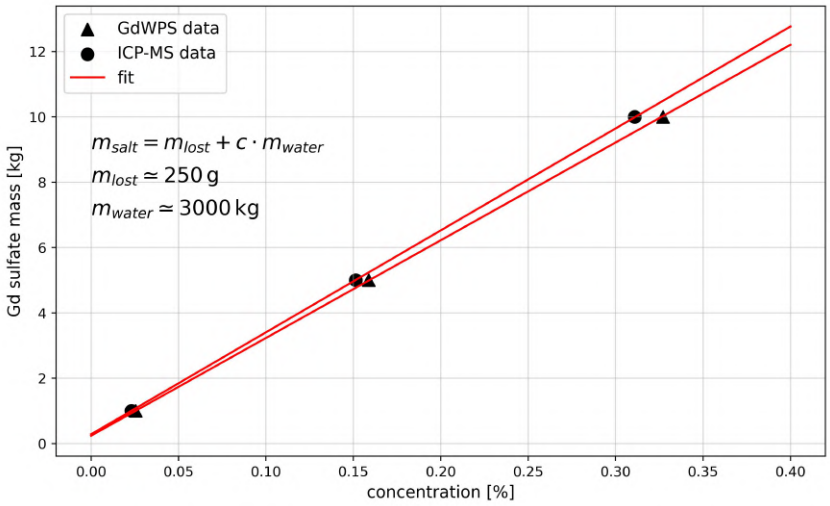

Figure 5.10: Concentrations estimated by the GdWPS through the calibration curve (triangles) and directly measured by ICP-MS (circles) in relation to the mass of salt in the system. The red curves fit the data; the estimated total mass of water in the GdWPS is $\simeq 3$ tons.

The linear fits have the following meaning. If a total mass of salt m_{salt} has been inserted in the plant and, among it, a certain mass m_{lost} has been lost during the transfer

(or stucked somewhere), the concentration in the main branch will be given by

$$c = \frac{m_{salt} - m_{lost}}{m_{water}} \tag{5.3}$$

where m_{water} is the total mass of water contained in the GdWPS. The fit has been then performed with the function

$$m_{salt} = m_{lost} + c \cdot m_{water} \, . \tag{5.4}$$

The results are slightly different if one considers the concentrations estimated online in the GdWPS or the ones measured by ICP-MS. The smaller concentration systematically found by this latter might be caused by the humidity of the Gadolinium salt: while during the construction of the conductivity-concentration curve it contributed to the salt mass, in the ICP-MS only the single isotopes are detected and humidity does not affect the measurement. Nevertheless, the difference is small and the two measurements provide similar estimations for the salt loss and total mass of the water: $m_{lost} \simeq 250\,\mathrm{g}$, $m_{water} \simeq 3\,\mathrm{tons}$.

For this reason, other 5 kg of Gd salt have been successively inserted, reaching a total mass of 15 kg of salt inside the GdWPS in order to obtain the nominal 0.5 % concentration (see Figure 5.11 (left)). After the new insertion other samples have been taken: one from the UF1 product and one from each nanofilter membrane output: NF1a, NF1b, NF1c, NF2a, NF2b. The results of conductivity and ICP-MS concentration compared to the conductivities measured by the GdWPS are shown in Figure 5.11 (right).

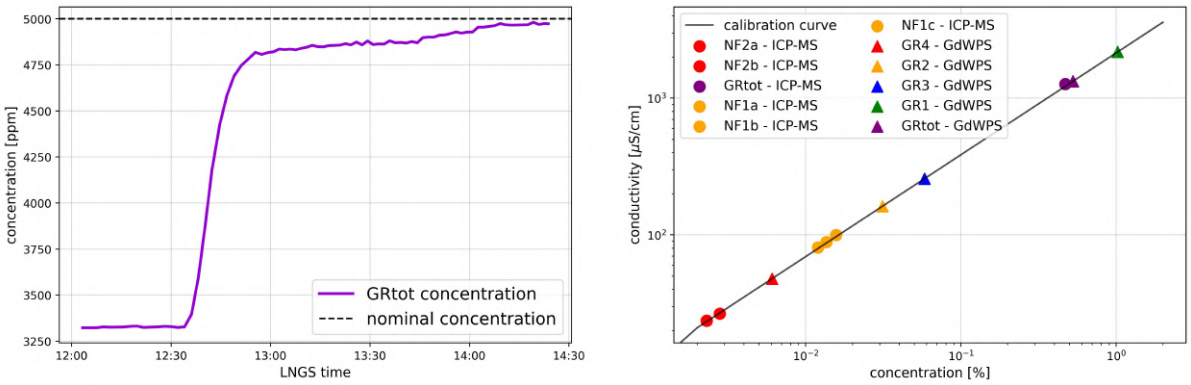

Figure 5.11: Left: concentration in the main branch of the GdWPS, estimated by the conductivities with the calibration curve and averaged between GR1 and GR2. After the addition of other 5 kg, reaching a total of 15 kg, the concentration reached $\simeq$ 5000 ppm, the nominal one. Right: conductivity and concentration results by GdWPS conductivities and ICP-MS.

While the sample taken in the main branch and representing GRtot shows, as in the previous cases, agreement between the two measurements, this is not true for the low-concentration samples. For both the nanofilters ICP-MS provides a lower concentration than the GdWPS result.

In general, all the measurements on the samples respect the relation between concentration and conductivity stated by the calibration curve.

5.2.2 Density increase

In Figure 5.7 it has been shown that the density increase after the first insertion was not visible by GD1, and only slightly by GD3. The following insertions had instead notable effects on both the sensors. In Figure 5.12 are shown the responses of GD1 and GD3 during the whole period where the insertions happened.

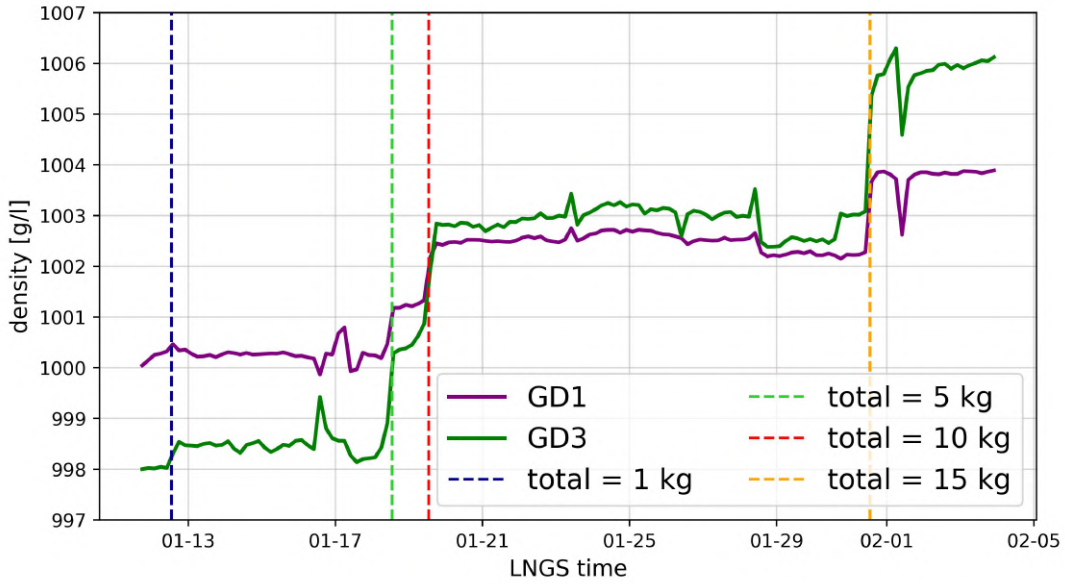

Figure 5.12: Behaviours of GD1 and GD3 during the different steps of the insertion of a total of 15 kg of Gd sulfate. A steep increase is visible in both the sensors in correspondence of every insertion.

GD1 and GD3 started respectively from values of $\simeq$ 1000.3 g/l and $\simeq$ 998 g/l. After the insertion of 10 kg in the GdWPS, they passed to $\simeq$ 1002.5 g/l and $\simeq$ 1003 g/l, with respective increases of $\simeq$ 2.2 g/l and $\simeq$ 5 g/l. From the calibration curve build before the insertion and reported in Figure 5.4, the expected increase going to 0.5 % concentration was $\simeq$ 3.8 g/l; in GD3 the concentration is approximately twice the average one, so its expected increase was $\simeq$ 7.6 g/l. Thus, the observed increases were about 30 % lower than the expectations. This also pointed to the fact that a significant amount of water

is present in the plant in addition to the 2 tons held by the mixing tank. With the extra addition of 5 kg of salt, the density in GD1 reached $\simeq 1003.8$ g/l and GD3 $\simeq 1006$ g/l. The total increases, after 15 kg, were respectively $\simeq 3.5$ g/l and $\simeq 8$ g/l, this time consistent with the expectations.

5.2.3 Separation efficiencies estimations

The Gadolinium separation efficiency, defined in Section 4.1.3, is one of the crucial parameters for the proper operation of the GdWPS. After the insertions of Gadolinium salt in the plant, they have been evaluated on the basis of the concentrations estimated both by the plant and by ICP-MS, using (4.2) and (4.3). Labeling the efficiencies of NF1 and NF2 as ϵ_1 and ϵ_2, a total separation efficiency can be also defined as

$$\epsilon_{tot} = 1 - (1 - \epsilon_1)(1 - \epsilon_2) \ . \tag{5.5}$$

The obtained values are reported in Table 5.2.

		ϵ_1	ϵ_2	ϵ_{tot}
1 kg	**GdWPS**	96.4 %	83 – 87 %	99.3 – 99.5 %
	ICP-MS	94.4 %	72.4 %	98.5 %
5 kg	**GdWPS**	96.2 %	90 %	99.6 %
	ICP-MS	93.5 %	89 %	99.25 %
10 kg	**GdWPS**	96.5 %	90 – 91 %	99.7 %
	ICP-MS	94.1 %	88.6 %	99.3 %
15 kg	**GdWPS**	96.7 %	89.6 %	99.6 %
	ICP-MS	98.5 %	90 %	99.85 %

Table 5.2: Separation efficiencies of the two nanofilters and total separation efficiency of the GdWPS for different amounts of salt in the plant. The results are weakly dependent on the concentrations. The estimations from ICP-MS are in general lower than the ones from the GdWPS conductivities.

In the Table, the separation efficiencies calculated by ICP-MS are reported, except for the case with 15 kg, referred to the sample taken after stopping the plant.

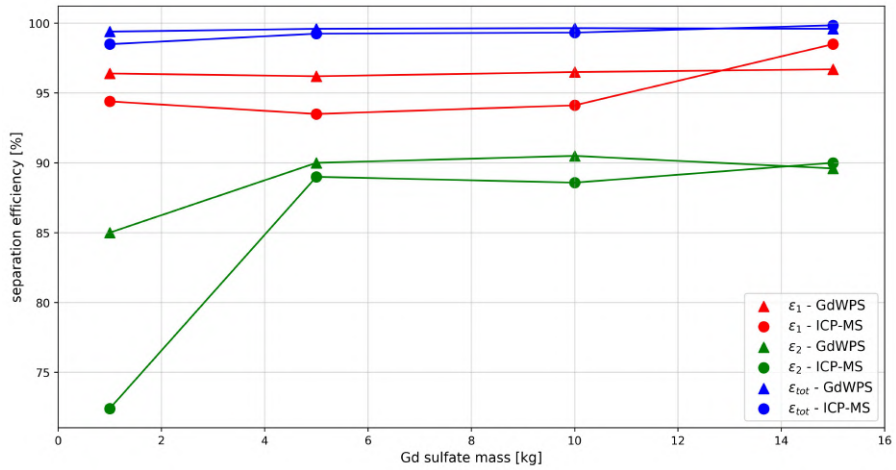

Figure 5.13: Separation efficiencies ϵ_1, ϵ_2 and ϵ_{tot} as a function of Gd salt mass in the GdWPS. There are no relevant differences, except for NF2 which shows a lower efficiency in the 1 kg condition.

The relation between mass of Gadolinium salt in the system and separation efficiencies of the two nanofilters is shown in Figure 5.13.

The efficiencies are not strongly dependent on the amount of Gd salt present in the plant. In general, NF1 has a greater separation power than NF2; the results from ICP-MS on the samples show worse results than the ones coming from GdWPS conductivities. An increase is observed for the ICP-MS results with 15 kg of Gd salt: this is due to the different sampling mode, since for this latter the result is reported referred to the average of the single membranes output (samples collected without stopping the GdWPS).

Flow rates ratio test

After the second insertion, with a total of 5 kg of salt dissolved in the GdWPS, the flow rates of the nanofilter outputs have been changed as a test. The values were previously the same as set in November (see Section 4.2.2): $\phi_{rej,1}/\phi_{prod,1} = 1$ and $\phi_{rej,2}/\phi_{prod,2} = 1/3$. Temporarily, the ratio for the second nanofilter has been changed to $\phi_{rej,2}/\phi_{prod,2} = 1$.

After this modification, the separation efficiency of NF2 improved. As shown in Figure 5.14, during the duration of the test its values stayed constant at $\simeq 96\,\%$, while it was close to $90\,\%$ previously. ϵ_{tot} increased until $\simeq 99.85\,\%$ during the test, to be compared to $\simeq 99.6\,\%$ before and after it. ϵ_1 was not affected by the modification, as the flow rate ratios at its outputs did not change.

This test demonstrated that acting on the flow rates at the outputs of the two nanofilters it is possible to enhance the separation efficiencies. However, acting as has been done for this test, the fraction of water passing through the DI and thus being purified from

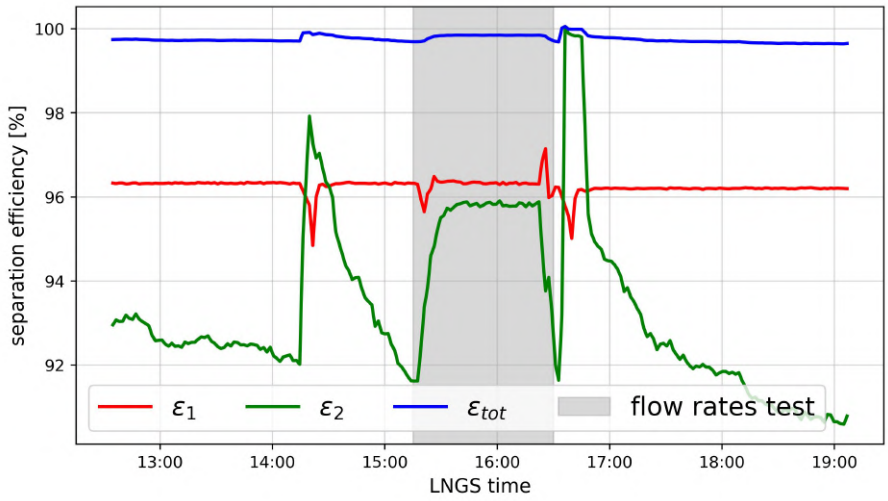

Figure 5.14: Separation efficiencies of NF1 (red), NF2 (green) and total (blue). Before the modification, ϵ_2 was decreasing; after the flow rates change, its values rapidly increased and remained constant at $\simeq 96\,\%$. After switching to the previous flow ratios, it came back to $\simeq 91\,\%$, reaching afterward a plateau value of $\simeq 90\,\%$.

ions is lower (from $\simeq$ 10 l/min to $\simeq$ 6.5 l/min). When maximising the separation efficiency, a compromise has to be done in order to not decrease too much the contribution of the DI to the purification.

After the test, the previous flow rates have been re-established.

5.3 Gd-water transparency measurements

Transparency measurements have been performed after the insertions to observe the effects of Gadolinium salt to the absorption length of water. In particular, four samples have been measured:

- a 0.5 % Gd-water solution prepared at the Chemistry Laboratory before starting the insertions of Gd salt;
- a sample taken from UF1 output (main branch) after the first insertion of 1 kg;
- a sample taken from UF1 output after the third insertion, with 10 kg of salt in the GdWPS;
- a sample taken from UF1 after the last insertion, with 15 kg of salt in the plant and the nominal 0.5 % concentration.

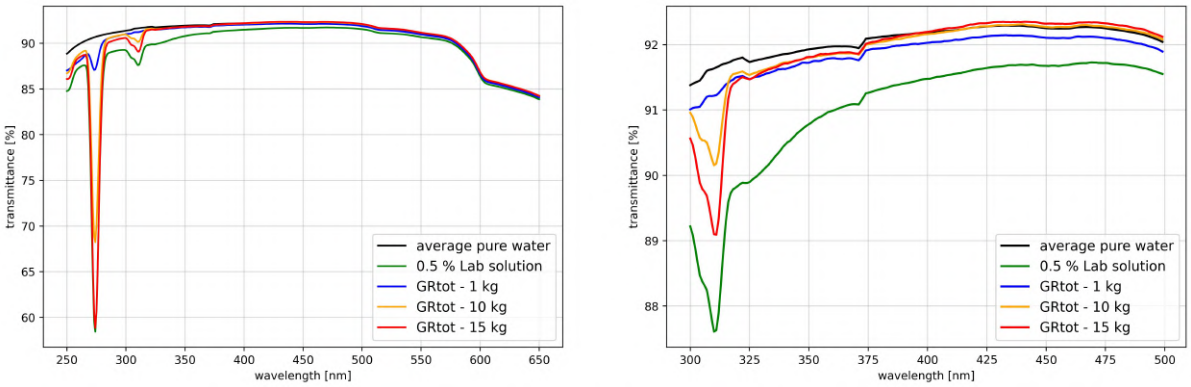

Figure 5.15: Left: transmittance results for the four samples compared to pure water. Right: zoom in the region of interest.

The results are shown in Figure 5.15.

Pure water measurements have been taken in correspondence of each sample measurement. Some discrepancy has been reported between them; in Figure 5.15 is drawn their average. The transmittances are close to the pure water level in most of the spectrum except for two visible absorption peaks. The stronger one is at around 275 nm and thus not particularly dangerous for the Neutron Veto. A second peak in correspondence to $\simeq$ 310 nm is instead in the region of interest, but weaker. These peaks have been studied in [162].

The absorption length of each sample has been calculated, starting from the transmittance results, with (4.10). The pure water sample used to get T_w is the one measured in the same day of each sample, with the closest conditions. The results are shown in Figure 5.16.

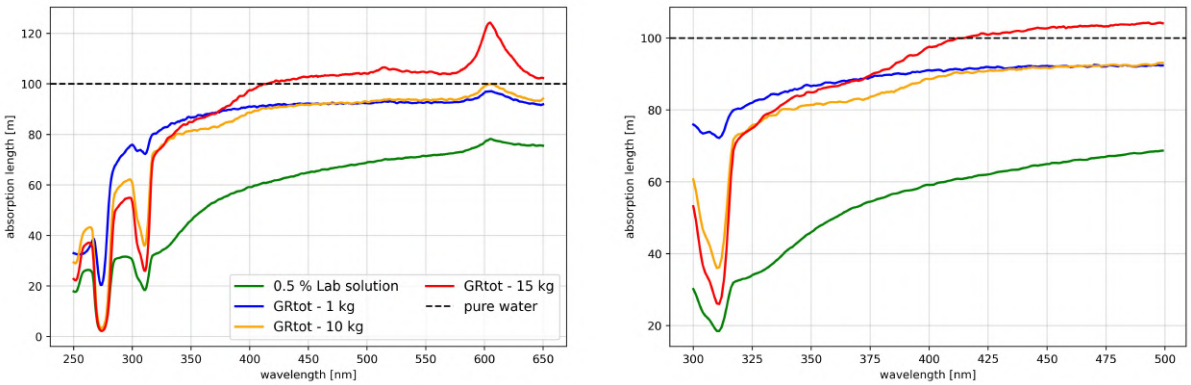

Figure 5.16: Left: absorption lengths of the Gd-water samples. Right: zoom in the region of interest.

The three samples collected by the GdWPS at different concentrations are characterized by absorption lengths similar to the one of pure water. If one assumes this latter to be 100 m as in this case, the absorption lengths in most of the spectrum are above 80 m. The absorption peak in the region of interest reduces this value to around 30 m. The solution prepared in the lab shows the lowest transparency (even if the absorption length is still tens of meters). This demonstrates the effect of the purification provided by the GdWPS.

5.4 Effect of the DI resin on Gd concentration

After the last Gd-salt insertion, the GdWPS worked stably for days, showing constant conductivities over time. On February 9th the DI resin has been finally reconnected in order to estimate the Gadolinium loss rate with the current configuration. The conductivities estimated right after the DI (GR4) and in the main branch (GRtot) are shown in Figure 5.17.

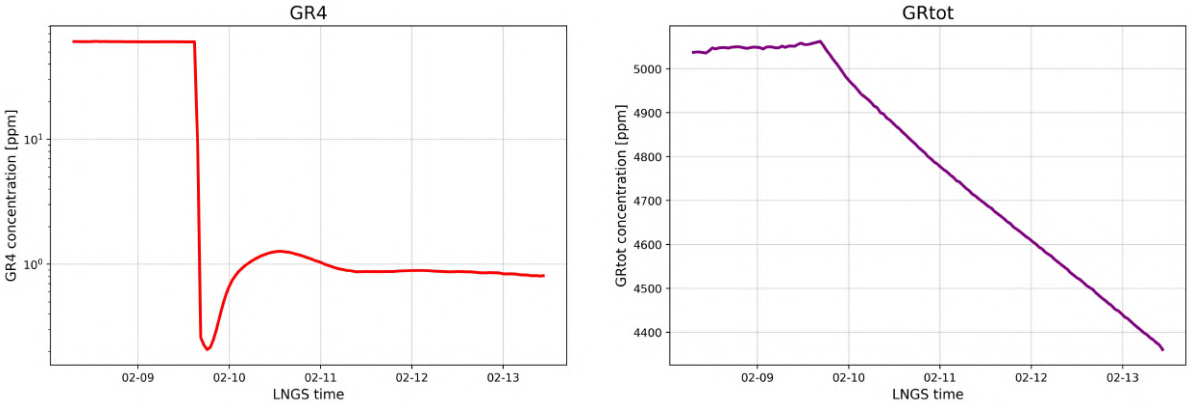

Figure 5.17: Left: Gd concentration in GR4 before and after the DI reconnection. Since GR4 is placed after the DI, the concentration measured after the reconnection of the resin is close to zero. Right: Gd concentration in the main branch of the plant before and after the DI reconnection.

Since GR4 is in the output of the DI, it does not measure anymore the product of NF2 but the very low-concentration solution remaining after the de-ionization process. This can be seen in Figure 5.17 (left): with the DI bypassed the concentration was stable at around 60 ppm; inserting the DI, after two days it stabilized to values lower than 1 ppm.

The concentration in the main branch, stable over time while the DI was bypassed, started visibly decreasing after the insertion of the resin. The decrease is proportional to the concentration, giving rise to an exponential decrease. Assuming that all the Gd

salt passing through the DI is lost, the mass of Gadolinium salt lost per unit time can be expressed as:

$$\frac{dm_{salt}}{dt} = -\left(1 - \epsilon_{tot}\right) \rho_w \, \phi_{main} \, c_{main} \tag{5.6}$$

where ρ_w is the water density and ϕ_{main} and c_{main} are respectively the flow rate and Gd concentration in the main branch (GRtot). The approximation $dm_{salt}/dt \sim$ const holds for short time scales and, by Figure 5.17, the observed decrease is around 200 ppm per day in the first period. Considering that $c_{main} \simeq 5000$ ppm and $\phi_{main} \simeq 25.8$ l/min, using (5.6) the total separation efficiency derived from the Gd loss rate is $\simeq 99.68\,\%$, compatible with what found by the GdWPS conductivities as shown in Table 5.2. The Gadolinium salt loss rate can be found to be $\simeq 600$ g/day, equivalent to $\simeq 220$ kg per year. Considering that, if Gadolinium is added to the XENONnT water tank at the nominal concentration, the total amount of salt in the system would be 3.4 tons, such loss rate would not represent a show-stopper for the GdWPS operation. Further tests are currently under development to optimize the system and make the Gadolinium loss rate even lower.

Conclusions

XENONnT is currently one of the experiments with the highest sensitivity in the direct search of Dark Matter, in particular of WIMPs. Its Neutron Veto (NV) system is specifically designed to reduce the neutron background and relies on the doping of water with Gadolinium-sulfate-octahydrate salt. In this thesis the results of two important aspects related to the Neutron Veto are presented: the Reflectivity Monitor, used to measure the optical properties of the detector, and the commissioning of the Gadolinium-water purification system (GdWPS).

The Reflectivity Monitor is a crucial tool to continuously inspect the optical properties of the Neutron Veto in terms of water transparency and wall reflectivity. It is particularly important when the GdWPS is used to purify the NV water, and even more when the Gadolinium will be dissolved in the NV. In Chapter 3, after an introduction to the hardware setup used for the Reflectivity Monitor, the data analysis has been described. With specific choices of the selection cuts, binning and fitting range, optimized using goodness-of-fit tests, the exponential time distribution of photons detected by the NV PMTs has been correctly fitted; the characteristic time constant τ of photons, which is the parameter of interest of the Reflectivity Monitor, is extracted in four different channels. They provide results with small statistical uncertainty (< 0.5 ns) and an additional systematic uncertainty (1 ns), due to the different results obtained in the four channels. The time constant related to the pure water operation of the NV is $\tau = (57 \pm 1)$ ns, constant over time, corresponding to an average path length of photons in water of 11.5 m. This time constant is the effect of three main sources: water transparency, walls reflectivity, and a geometric component. The latter has been estimated via Monte Carlo simulations to be $\tau_{geom} = (70.69 \pm 0.05)$ ns. The Reflectivity Monitor results have been also validated with Neutron Veto background data, which differently from Reflectivity Monitor ones include a broad range of wavelengths. After appropriate selection cuts, a time constant has been estimated by background data as well, obtaining values affected by larger uncertainties but compatible with the Reflectivity Monitor results.

The GdWPS has been described in Chapter 4. The methods used to insert Gadolinium salt in the plant and purify water minimizing the impact on the Gadolinium concentration have been shown. The main operations and tests made during the second part of

2022 have been reported, focusing on the performances estimated by conductivity sensors and on the effects of different purification elements, such as DI and ORT resins. During that period, the plant was working with demineralized water and, in its cleanest part, reached purity levels close to those of demi-water (resistivity $\simeq 18\,\mathrm{M\Omega \cdot cm}$). GdWPS has been connected repeatedly to the Neutron Veto and the Reflectivity Monitor showed that no degradation occurred; in a longer time scale of many months, it showed a negligible decrease of the time constant of about 0.3 ns. At the same time, the direct effect of the GdWPS on water transparency has been measured with a dedicated instrument: a spectrophotometer able to measure transparency over a large range of photon wavelengths. The samples collected from the GdWPS showed absorption lengths greater than 70 m in the region of interest, and all of them had larger transparency than the samples taken from the Neutron Veto.

Finally, in Chapter 5, the outcome of the first insertion of Gadolinium-sulfate in the GdWPS has been presented. Adding Gadolinium salt in the system, isolated from the Neutron Veto, was necessary to test the insertion procedure, the stability of the plant, the tools to estimate the Gd concentration, and the separation efficiency, a crucial parameter for future operations with Gd in the NV. The insertion happened in four steps, and a total of 15 kg of Gd-salt has been added to the system in January 2023; no relevant issue has been reported during the insertions, and the time needed to fully dissolve the salt in the GdWPS was about 30 minutes. After the insertions, the concentrations in different branches of the system have been monitored: both applying ICP-MS technique on samples collected from the plant, and indirectly estimating it through conductivity measurements. This latter method was possible thanks to a preliminary calibration where the relation between Gadolinium concentration and electrical conductivity has been investigated: a power law relation has been found and it proved to be valid also during GdWPS operation. The same procedure for density turned out to be harder to apply but good as an additional check. With 15 kg of salt in the system, the concentration reached the nominal value of 0.5 %. The separation efficiency has also been estimated with three different methods: by the indirect measurement of concentrations through conductivities, by the direct measures of concentrations through ICP-MS, and by the Gadolinium loss rate after reconnecting the DI resin. The first method provided $\epsilon_{tot} = 99.6$ %, the second one 99.85 %. The Gd-salt loss rate was estimated to be $\simeq 600\,\mathrm{g/day}$, providing $\epsilon_{tot} = 99.68$ %. Transparency measurements on Gd-water samples show that the GdWPS provides a significant increase in transparency with respect to the raw solution prepared at the Chemistry Laboratory, leading to photon absorption lengths close to the one of demi-water (difference in transmittance < 0.5 %).

In conclusion, in the work described in this thesis important steps for the GdWPS commissioning have been carried out, testing various components and verifying the response of the main sensors. At the same time, the Reflectivity Monitor tool has been optimized, getting it ready to stably check the Neutron Veto performances over a long time scale. The first Gadolinium insertion test showed that the plant satisfies the re-

quirements for the Gd-salt insertion in the Neutron Veto: the concentration can be maintained at the needed level, with a tolerable loss rate of Gd-salt during operations; at the same time, the level of transparency is preserved.

References

[1] Nabila Aghanim et al. "Planck 2018 results-VI. Cosmological parameters". In: *Astronomy & Astrophysics* 641 (2020), A6.

[2] Neta A Bahcall et al. "The cosmic triangle: Revealing the state of the universe". In: *science* 284.5419 (1999), pp. 1481–1488.

[3] Sean M Carroll. "The cosmological constant". In: *Living reviews in relativity* 4.1 (2001), pp. 1–56.

[4] Saul Perlmutter et al. "Measurements of Ω and Λ from 42 high-redshift supernovae". In: *The Astrophysical Journal* 517.2 (1999), p. 565.

[5] Md Ishaque Khan and Rajib Saha. "Isotropy statistics of CMB hot and cold spots". In: *Journal of Cosmology and Astroparticle Physics* 2022.06 (2022), p. 006.

[6] Nandita Khetan et al. "A new measurement of the Hubble constant using Type Ia supernovae calibrated with surface brightness fluctuations". In: *Astronomy & Astrophysics* 647 (2021), A72.

[7] Gong-Bo Zhao et al. "Probing for dynamics of dark energy and curvature of universe with latest cosmological observations". In: *Physics Letters B* 648.1 (2007), pp. 8–13.

[8] TMC Abbott et al. "First cosmology results using type Ia supernovae from the dark energy survey: constraints on cosmological parameters". In: *The Astrophysical Journal Letters* 872.2 (2019), p. L30.

[9] Gianfranco Bertone, Dan Hooper, and Joseph Silk. "Particle dark matter: Evidence, candidates and constraints". In: *Physics reports* 405.5-6 (2005), pp. 279–390.

[10] Information@eso.org. *Spiral galaxy NGC 1376*. URL: https://esahubble.org/images/opo1000a/.

[11] Jonathan R Pritchard and Abraham Loeb. "21 cm cosmology in the 21st century". In: *Reports on Progress in Physics* 75.8 (2012), p. 086901.

[12] Maurizio Spurio, Spurio, and Bellantone. *Probes of Multimessenger Astrophysics*. Springer, 2018.

[13] KG Begeman, AH Broeils, and RH Sanders. "Extended rotation curves of spiral galaxies: Dark haloes and modified dynamics". In: *Monthly Notices of the Royal Astronomical Society* 249.3 (1991), pp. 523–537.

[14] Julio F Navarro, Carlos S Frenk, and Simon DM White. "A universal density profile from hierarchical clustering". In: *The Astrophysical Journal* 490.2 (1997), p. 493.

[15] G Bertin et al. "A search for dark matter in elliptical galaxies: radially extended spectroscopic observations for six objects". In: *Astronomy and Astrophysics* 292 (1994), pp. 381–391.

[16] M Carollo et al. "Dark matter in elliptical galaxies". In: *arXiv preprint astro-ph/9501046* (1995).

[17] Fritz Zwicky. "On the Masses of Nebulae and of Clusters of Nebulae". In: *The Astrophysical Journal* 86 (1937), p. 217.

[18] Donald J Horner, Richard F Mushotzky, and Caleb A Scharf. "Observational tests of the mass-temperature relation for galaxy clusters". In: *The Astrophysical Journal* 520.1 (1999), p. 78.

[19] Joachim Trümper. "The ROSAT mission". In: *Advances in Space Research* 2.4 (1982), pp. 241–249.

[20] Martin C Weisskopf et al. "Chandra X-ray Observatory (CXO): overview". In: *X-Ray Optics, Instruments, and Missions III* 4012 (2000), pp. 2–16.

[21] F Govoni et al. "Chandra temperature maps for galaxy clusters with radio halos". In: *The Astrophysical Journal* 605.2 (2004), p. 695.

[22] R Demarco et al. "A study of dark matter halos and gas properties in clusters of galaxies from ROSAT data". In: *Astronomy & Astrophysics* 407.2 (2003), pp. 437–451.

[23] Joachim Wambsganss. "Gravitational lensing in astronomy". In: *Living Reviews in Relativity* 1.1 (1998), pp. 1–74.

[24] Frank Watson Dyson, Arthur Stanley Eddington, and Charles Davidson. "IX. A determination of the deflection of light by the Sun's gravitational field, from observations made at the total eclipse of May 29, 1919". In: *Philosophical Transactions of the Royal Society of London. Series A, Containing Papers of a Mathematical or Physical Character* 220.571-581 (1920), pp. 291–333.

[25] Henk Hoekstra, Howard KC Yee, and Michael D Gladders. "Properties of galaxy dark matter halos from weak lensing". In: *The Astrophysical Journal* 606.1 (2004), p. 67.

[26] Richard Massey, Thomas Kitching, and Johan Richard. "The dark matter of gravitational lensing". In: *Reports on Progress in Physics* 73.8 (2010), p. 086901.

[27] Joachim Wambsganss. "Gravitational microlensing". In: *Gravitational Lensing: Strong, Weak and Micro*. Springer, 2006, pp. 453–540.

[28] Douglas Clowe, Anthony Gonzalez, and Maxim Markevitch. "Weak-lensing mass reconstruction of the interacting cluster 1e 0657–558: Direct evidence for the existence of dark matter". In: *The Astrophysical Journal* 604.2 (2004), p. 596.

[29] *The bullet cluster*. URL: https://www.esa.int/ESA_Multimedia/Images/2016/04/The_Bullet_Cluster.

[30] Maxim Markevitch et al. "Direct constraints on the dark matter self-interaction cross section from the merging galaxy cluster 1e 0657–56". In: *The Astrophysical Journal* 606.2 (2004), p. 819.

[31] Mordehai Milgrom. "The MOND paradigm". In: *arXiv preprint arXiv:0801.3133* (2008).

[32] Wayne Hu and Scott Dodelson. "Cosmic microwave background anisotropies". In: *Annual Review of Astronomy and Astrophysics* 40.1 (2002), pp. 171–216.

[33] JA Tauber, ESA, the Planck Scientific Collaboration, et al. "The planck mission". In: *Advances in Space Research* 34.3 (2004), pp. 491–496.

[34] *Planck's view of the Cosmic Microwave Background*. URL: https://sci.esa.int/web/planck/-/60500-plancks-view-of-the-cosmic-microwave-background.

[35] Bernard Carr. "Baryonic dark matter". In: *Annual Review of Astronomy and Astrophysics* 32 (1994), pp. 531–590.

[36] Peter J Kernan and Lawrence M Krauss. "Refined big bang nucleosynthesis constraints on Ω B and N ν". In: *Physical Review Letters* 72.21 (1994), p. 3309.

[37] EK Park. *DMSAG Report on the Direct Detection and Study of Dark Matter*. 2007.

[38] Lars Bergström. "Dark matter candidates". In: *New Journal of Physics* 11.10 (2009), p. 105006.

[39] W Hampel et al. "Final results of the 51Cr neutrino source experiments in GALLEX". In: *Physics Letters B* 420.1-2 (1998), pp. 114–126.

[40] Kamiokande Collaboration et al. "Determination of Solar Neutrino Oscillation Parameters using 1496 Days of Super-Kamiokande-I Data". In: *arXiv preprint hep-ex/0205075* (2002).

[41] N Barros, SNO Collaboration, et al. "Final results from SNO". In: *Nuclear Physics B-Proceedings Supplements* 237 (2013), pp. 107–110.

[42] Nabila Aghanim et al. "Planck 2018 results-I. Overview and the cosmological legacy of Planck". In: *Astronomy & Astrophysics* 641 (2020), A1.

[43] Alexey Boyarsky et al. “Sterile neutrino dark matter”. In: *Progress in Particle and Nuclear Physics* 104 (2019), pp. 1–45.

[44] Takehiko Asaka, Steve Blanchet, and Mikhail Shaposhnikov. “The νMSM, dark matter and neutrino masses”. In: *Physics Letters B* 631.4 (2005), pp. 151–156.

[45] Hai-Yang Cheng. “The strong CP problem revisited”. In: *Physics Reports* 158.1 (1988), pp. 1–89.

[46] R. L. Workman et al. “Review of Particle Physics”. In: *PTEP* 2022 (2022), p. 083C01. DOI: 10.1093/ptep/ptac097.

[47] Frank Daniel Steffen. “Dark-matter candidates”. In: *The European Physical Journal C* 59.2 (2009), pp. 557–588.

[48] CA Baker et al. “Improved experimental limit on the electric dipole moment of the neutron”. In: *Physical Review Letters* 97.13 (2006), p. 131801.

[49] Roberto D Peccei and Helen R Quinn. “Constraints imposed by CP conservation in the presence of pseudoparticles”. In: *Physical Review D* 16.6 (1977), p. 1791.

[50] Steven Weinberg. “A new light boson?” In: *Physical Review Letters* 40.4 (1978), p. 223.

[51] Tong Li and Rui-Jia Zhang. “Axion-like particle from primordial black hole evaporation and its detection in neutrino experiments”. In: *arXiv preprint arXiv:2208.02696* (2022).

[52] Elena Aprile et al. “Excess electronic recoil events in XENON1T”. In: *Physical Review D* 102.7 (2020), p. 072004.

[53] E Aprile et al. “Search for new physics in electronic recoil data from XENONnT”. In: *Physical Review Letters* 129.16 (2022), p. 161805.

[54] Stephen P Martin. “A supersymmetry primer”. In: *Perspectives on supersymmetry II*. World Scientific, 2010, pp. 1–153.

[55] Anadi Canepa. “Searches for supersymmetry at the Large Hadron Collider”. In: *Reviews in Physics* 4 (2019), p. 100033.

[56] Daniel E López-Fogliani, Andres D Perez, and Roberto Ruiz de Austri. “Dark matter candidates in the NMSSM with RH neutrino superfields”. In: *Journal of Cosmology and Astroparticle Physics* 2021.04 (2021), p. 067.

[57] Leszek Roszkowski, Enrico Maria Sessolo, and Sebastian Trojanowski. “WIMP dark matter candidates and searches—current status and future prospects”. In: *Reports on Progress in Physics* 81.6 (2018), p. 066201.

[58] Benjamin Audren et al. “Strongest model-independent bound on the lifetime of Dark Matter”. In: *Journal of Cosmology and Astroparticle Physics* 2014.12 (2014), p. 028.

[59] Paolo Gondolo and Graciela Gelmini. "Cosmic abundances of stable particles: Improved analysis". In: *Nuclear Physics B* 360.1 (1991), pp. 145–179.

[60] Gary Steigman, Basudeb Dasgupta, and John F Beacom. "Precise relic WIMP abundance and its impact on searches for dark matter annihilation". In: *Physical Review D* 86.2 (2012), p. 023506.

[61] Takeshi Nihei, Leszek Roszkowski, and Roberto Ruiz de Austri. "Towards an accurate calculation of the neutralino relic density". In: *Journal of High Energy Physics* 2001.05 (2001), p. 063.

[62] Gerard Jungman, Marc Kamionkowski, and Kim Griest. "Supersymmetric dark matter". In: *Physics Reports* 267.5-6 (1996), pp. 195–373.

[63] Kim Griest. "Cross sections, relic abundance, and detection rates for neutralino dark matter". In: *Physical Review D* 38.8 (1988), p. 2357.

[64] Paolo Gondolo. "Phenomenological introduction to direct dark matter detection". In: *arXiv preprint hep-ph/9605290* (1996).

[65] Jan Conrad. "Indirect Detection of WIMP Dark Matter: a compact review". In: *arXiv preprint arXiv:1411.1925* (2014).

[66] G Kanbach et al. "The project EGRET (energetic gamma-ray experiment telescope) on NASA's Gamma-Ray Observatory GRO". In: *Space Science Reviews* 49.1 (1989), pp. 69–84.

[67] RC Hartman et al. "The third EGRET catalog of high-energy gamma-ray sources". In: *The Astrophysical Journal Supplement Series* 123.1 (1999), p. 79.

[68] WB Atwood et al. "The large area telescope on the Fermi gamma-ray space telescope mission". In: *The Astrophysical Journal* 697.2 (2009), p. 1071.

[69] Germán A Gómez-Vargas et al. "Constraints on WIMP annihilation for contracted dark matter in the inner Galaxy with the Fermi-LAT". In: *Journal of Cosmology and Astroparticle Physics* 2013.10 (2013), p. 029.

[70] Werner Hofmann and Hess Collaboration. "The high energy stereoscopic system (HESS) project". In: *AIP Conference Proceedings*. Vol. 515. 1. American Institute of Physics. 2000, pp. 500–509.

[71] E Lorenz and Magic collaboration. "The MAGIC telescope project". In: *AIP Conference Proceedings*. Vol. 515. 1. American Institute of Physics. 2000, pp. 510–514.

[72] Jamie Holder et al. "The first VERITAS telescope". In: *Astroparticle Physics* 25.6 (2006), pp. 391–401.

[73] M Actis et al. "Design concepts for the Cherenkov Telescope Array CTA: an advanced facility for ground-based high-energy gamma-ray astronomy". In: *Experimental Astronomy* 32.3 (2011), pp. 193–316.

[74] T Montaruli, ANTARES collaboration, et al. "Status report of the ANTARES project". In: *Nuclear Physics B-Proceedings Supplements* 110 (2002), pp. 513–515.

[75] P Berghaus, IceCube Collaboration, et al. "IceCube: Status and first results". In: *Nuclear Physics B-Proceedings Supplements* 190 (2009), pp. 127–132.

[76] Annarita Margiotta, KM3NeT Collaboration, et al. "The KM3NeT deep-sea neutrino telescope". In: *Nuclear Instruments and Methods in Physics Research Section A: Accelerators, Spectrometers, Detectors and Associated Equipment* 766 (2014), pp. 83–87.

[77] S Fukuda et al. "The super-kamiokande detector". In: *Nuclear Instruments and Methods in Physics Research Section A: Accelerators, Spectrometers, Detectors and Associated Equipment* 501.2-3 (2003), pp. 418–462.

[78] S Fukuda et al. "Determination of solar neutrino oscillation parameters using 1496 days of Super-Kamiokande-I data". In: *Physics Letters B* 539.3-4 (2002), pp. 179–187.

[79] Y Ashie et al. "Measurement of atmospheric neutrino oscillation parameters by Super-Kamiokande I". In: *Physical Review D* 71.11 (2005), p. 112005.

[80] MG Aartsen et al. "Search for dark matter annihilation in the Galactic Center with IceCube-79". In: *The European Physical Journal C* 75.10 (2015), pp. 1–12.

[81] Mark G Aartsen et al. "The IceCube Neutrino Observatory: instrumentation and online systems". In: *Journal of Instrumentation* 12.03 (2017), P03012.

[82] Christopher W Walter and Super-Kamiokande collaboration. "The super-kamiokande experiment". In: *Neutrino Oscillations: Present Status and Future Plans*. World Scientific, 2008, pp. 19–43.

[83] S Aiello et al. "Deep-sea deployment of the KM3NeT neutrino telescope detection units by self-unrolling". In: *Journal of Instrumentation* 15.11 (2020), P11027.

[84] V Bonvicini et al. "The PAMELA experiment in space". In: *Nuclear Instruments and Methods in Physics Research Section A: Accelerators, Spectrometers, Detectors and Associated Equipment* 461.1-3 (2001), pp. 262–268.

[85] Jorge Casaus. "The AMS-02 experiment on the ISS". In: *Journal of Physics: Conference Series*. Vol. 171. 1. IOP Publishing. 2009, p. 012045.

[86] Dan Hooper et al. "HAWC observations strongly favor pulsar interpretations of the cosmic-ray positron excess". In: *Physical Review D* 96.10 (2017), p. 103013.

[87] ATLAS Collaboration et al. *The ATLAS experiment at the CERN large hadron collider*. 2008.

[88] CMS Collaboration et al. "The CMS experiment at the CERN LHC". In: *JInst* 3 (2008), S08004.

[89] CMS collaboration et al. "Search for dark matter and unparticles in events with a Z boson and missing transverse momentum in proton-proton collisions at sqrt (s)= 13 TeV". In: *arXiv preprint arXiv:1701.02042* (2017).

[90] A Bettini. "The world deep underground laboratories". In: *The European Physical Journal Plus* 127.9 (2012), pp. 1–11.

[91] Jochen Schieck et al. "Direct dark matter search with the CRESST II experiment". In: *arXiv preprint arXiv:1611.02113* (2016).

[92] M Sisti et al. "The CRESST dark matter experiment: status and perspectives". In: *Nuclear Instruments and Methods in Physics Research Section A: Accelerators, Spectrometers, Detectors and Associated Equipment* 444.1-2 (2000), pp. 312–314.

[93] R Agnese et al. "Results from the super cryogenic dark matter search experiment at Soudan". In: *Physical review letters* 120.6 (2018), p. 061802.

[94] Wolfgang Rau et al. "CDMS and SuperCDMS". In: *Journal of Physics: Conference Series*. Vol. 375. 1. IOP Publishing. 2012, p. 012005.

[95] D Drain et al. "Status of the EDELWEISS experiment". In: *Physics reports* 307.1-4 (1998), pp. 297–300.

[96] R Bernabei et al. "First results from DAMA/LIBRA and the combined results with DAMA/NaI". In: *The European Physical Journal C* 56.3 (2008), pp. 333–355.

[97] Rita Bernabei et al. "First model independent results from DAMA/LIBRA–phase2". In: *Universe* 4.11 (2018), p. 116.

[98] G Adhikari et al. "Initial performance of the COSINE-100 experiment". In: *The European Physical Journal C* 78.2 (2018), pp. 1–19.

[99] Govinda Adhikari et al. "Strong constraints from COSINE-100 on the DAMA dark matter results using the same sodium iodide target". In: *Science advances* 7.46 (2021), eabk2699.

[100] G Adhikari et al. "An induced annual modulation signature in COSINE-100 data by DAMA/LIBRA's analysis method". In: *arXiv preprint arXiv:2208.05158* (2022).

[101] G Angloher et al. "The COSINUS project: perspectives of a NaI scintillating calorimeter for dark matter search". In: *The European Physical Journal C* 76.8 (2016), pp. 1–7.

[102] C Tomei. "SABRE: Dark matter annual modulation detection in the northern and southern hemispheres". In: *Nuclear Instruments and Methods in Physics Research Section A: Accelerators, Spectrometers, Detectors and Associated Equipment* 845 (2017), pp. 418–420.

[103] Vitaly Chepel and Henrique Araújo. "Liquid noble gas detectors for low energy particle physics". In: *Journal of Instrumentation* 8.04 (2013), R04001.

[104] E Aprile et al. "Projected WIMP sensitivity of the XENONnT dark matter experiment". In: *Journal of Cosmology and Astroparticle Physics* 2020.11 (2020), p. 031.

[105] DN McKinsey, LZ Collaboration, et al. "The LZ dark matter experiment". In: *Journal of Physics: Conference Series*. Vol. 718. 4. IOP Publishing. 2016, p. 042039.

[106] Hongguang Zhang et al. "Dark matter direct search sensitivity of the PandaX-4T experiment". In: *Science China Physics, Mechanics & Astronomy* 62.3 (2019), pp. 1–9.

[107] J Aalbers et al. "DARWIN: towards the ultimate dark matter detector". In: *Journal of Cosmology and Astroparticle Physics* 2016.11 (2016), p. 017.

[108] Paolo Agnes et al. "First results from the DarkSide-50 dark matter experiment at Laboratori Nazionali del Gran Sasso". In: *Physics Letters B* 743 (2015), pp. 456–466.

[109] Craig E Aalseth et al. "DarkSide-20k: A 20 tonne two-phase LAr TPC for direct dark matter detection at LNGS". In: *The European Physical Journal Plus* 133.3 (2018), pp. 1–129.

[110] Julien Billard et al. "Direct detection of dark matter—APPEC committee report". In: *Reports on Progress in Physics* 85.5 (2022), p. 056201.

[111] E Aprile et al. "Design and performance of the XENON10 dark matter experiment". In: *Astroparticle Physics* 34.9 (2011), pp. 679–698.

[112] E Aprile et al. "First axion results from the XENON100 experiment". In: *Physical Review D* 90.6 (2014), p. 062009.

[113] DS Akerib et al. "First searches for axions and axionlike particles with the LUX experiment". In: *Physical review letters* 118.26 (2017), p. 261301.

[114] E Aprile et al. "Double-weak decays of Xe 124 and Xe 136 in the XENON1T and XENONnT experiments". In: *Physical Review C* 106.2 (2022), p. 024328.

[115] Francisco Neves et al. "Measurement of the absolute reflectance of polytetrafluoroethylene (PTFE) immersed in liquid xenon". In: *Journal of Instrumentation* 12.01 (2017), P01017.

[116] Pietro Di Gangi. "The Xenon Road to Direct Detection of Dark Matter at LNGS: The XENON Project". In: *Universe* 7.8 (2021), p. 313.

[117] J Angle et al. "First results from the XENON10 dark matter experiment at the Gran Sasso National Laboratory". In: *Physical Review Letters* 100.2 (2008), p. 021303.

[118] D Akimov et al. “Observation of coherent elastic neutrino-nucleus scattering”. In: *Science* 357.6356 (2017), pp. 1123–1126.

[119] Ciaran AJ O’Hare. “New definition of the neutrino floor for direct dark matter searches”. In: *Physical Review Letters* 127.25 (2021), p. 251802.

[120] J Angle et al. “Limits on spin-dependent WIMP-nucleon cross sections from the XENON10 experiment”. In: *Physical review letters* 101.9 (2008), p. 091301.

[121] J Angle et al. “Constraints on inelastic dark matter from XENON10”. In: *Physical Review D* 80.11 (2009), p. 115005.

[122] Elena Aprile et al. “The XENON100 dark matter experiment”. In: *Astroparticle Physics* 35.9 (2012), pp. 573–590.

[123] E Aprile et al. “First dark matter results from the XENON100 experiment”. In: *Physical Review Letters* 105.13 (2010), p. 131302.

[124] Elena Aprile et al. “Dark matter results from 100 live days of XENON100 data”. In: *Physical Review Letters* 107.13 (2011), p. 131302.

[125] Elena Aprile et al. “Dark matter results from 225 live days of XENON100 data”. In: *Physical review letters* 109.18 (2012), p. 181301.

[126] E Aprile et al. “XENON100 dark matter results from a combination of 477 live days”. In: *Physical Review D* 94.12 (2016), p. 122001.

[127] E Aprile et al. “Limits on spin-dependent WIMP-nucleon cross sections from 225 live days of XENON100 data”. In: *Physical review letters* 111.2 (2013), p. 021301.

[128] E Aprile et al. “Implications on inelastic dark matter from 100 live days of XENON100 data”. In: *Physical Review D* 84.6 (2011), p. 061101.

[129] Elena Aprile et al. “Search for WIMP inelastic scattering off xenon nuclei with XENON100”. In: *Physical Review D* 96.2 (2017), p. 022008.

[130] E Aprile et al. “Study of the electromagnetic background in the XENON100 experiment”. In: *Physical Review D* 83.8 (2011), p. 082001.

[131] Elena Aprile et al. “The neutron background of the XENON100 dark matter search experiment”. In: *Journal of Physics G: Nuclear and Particle Physics* 40.11 (2013), p. 115201.

[132] Elena Aprile et al. “Intrinsic backgrounds from Rn and Kr in the XENON100 experiment”. In: *The European Physical Journal C* 78 (2018), pp. 1–12.

[133] Elena Aprile et al. “The XENON1T dark matter experiment”. In: *The European Physical Journal C* 77.12 (2017), pp. 1–23.

[134] XENON Collaboration et al. “Dark matter search results from a one ton-year exposure of xenon1t”. In: *Physical review letters* 121.11 (2018), p. 111302.

[135] Elena Aprile et al. “Removing krypton from xenon by cryogenic distillation to the ppq level”. In: *The European Physical Journal C* 77 (2017), pp. 1–12.

[136] Ch Geis et al. “Optical response of highly reflective film used in the water Cherenkov muon veto of the XENON1T dark matter experiment”. In: *Journal of Instrumentation* 12.06 (2017), P06017.

[137] E Aprile et al. “Conceptual design and simulation of a water Cherenkov muon veto for the XENON1T experiment”. In: *Journal of instrumentation* 9.11 (2014), P11006.

[138] XENON Collaboration xe-editorial@ lngs. infn. it et al. “Lowering the radioactivity of the photomultiplier tubes for the XENON1T dark matter experiment”. In: *The European Physical Journal C* 75 (2015), pp. 1–10.

[139] XENON Collaboration et al. “XENON1T dark matter data analysis: Signal and background models and statistical inference”. In: *Physical Review D* 99.11 (2019), p. 112009.

[140] Pietro Di Gangi. “Dark Matter Search with the XENON1T Experiment: Background Predictions, Data Analysis and Final Results”. In: (2019).

[141] XENON Collaboration et al. “Constraining the spin-dependent WIMP-nucleon cross sections with XENON1T”. In: *Physical review letters* 122.14 (2019), p. 141301.

[142] Elena Aprile et al. “Search for inelastic scattering of WIMP dark matter in XENON1T”. In: *Physical Review D* 103.6 (2021), p. 063028.

[143] Elena Aprile et al. “Search for coherent elastic scattering of solar b 8 neutrinos in the xenon1t dark matter experiment”. In: *Physical review letters* 126.9 (2021), p. 091301.

[144] “Observation of two-neutrino double electron capture in 124Xe with XENON1T”. In: *Nature* 568.7753 (2019), pp. 532–535.

[145] Andrea Mancuso. “Neutron Veto of XENONnT: final construction design of the system and extensive study and calibration of the PMTs.” In: ().

[146] William R Leo. “Techniques for nuclear and particle physics experiments”. In: *Nucl Instrum Methods Phys Res* 834 (1988), p. 290.

[147] Boris M Bolotovskii. “Vavilov–Cherenkov radiation: its discovery and application”. In: *Physics-Uspekhi* 52.11 (2009), p. 1099.

[148] John D Mason, Michael T Cone, and Edward S Fry. “Ultraviolet (250–550 nm) absorption spectrum of pure water”. In: *Applied optics* 55.25 (2016), pp. 7163–7172.

[149] Truman S Light et al. “The fundamental conductivity and resistivity of water”. In: *Electrochemical and solid-state letters* 8.1 (2004), E16.

[150] B Hamermesh, GR Ringo, and S Wexler. "The thermal neutron capture cross section of hydrogen". In: *Physical Review* 90.4 (1953), p. 603.

[151] Kohei Wada et al. "What is a breakdown of continuous component hidden under 4.4-MeV gamma-ray peak from the AmBe source?" In: *Journal of Physics: Conference Series*. Vol. 2156. 1. IOP Publishing. 2021, p. 012209.

[152] KJR Rosman and PDP Taylor. "Isotopic compositions of the elements 1997 (Technical Report)". In: *Pure and Applied Chemistry* 70.1 (1998), pp. 217–235.

[153] Kaito Hagiwara et al. "Gamma-ray spectrum from thermal neutron capture on gadolinium-157". In: *Progress of Theoretical and Experimental Physics* 2019.2 (2019), p. 023D01.

[154] K Abe et al. "First gadolinium loading to Super-Kamiokande". In: *Nuclear Instruments and Methods in Physics Research Section A: Accelerators, Spectrometers, Detectors and Associated Equipment* 1027 (2022), p. 166248.

[155] Ll Marti et al. "Evaluation of gadolinium's action on water Cherenkov detector systems with EGADS". In: *Nuclear Instruments and Methods in Physics Research Section A: Accelerators, Spectrometers, Detectors and Associated Equipment* 959 (2020), p. 163549.

[156] Hans Dembinski and Piti Ongmongkolkul et al. "scikit-hep/iminuit". In: (Dec. 2020). DOI: 10.5281/zenodo.3949207. URL: https://doi.org/10.5281/zenodo.3949207.

[157] Glen Cowan. *Statistical data analysis*. Oxford university press, 1998.

[158] GEANT Collaboration, S Agostinelli, et al. "GEANT4–a simulation toolkit". In: *Nucl. Instrum. Meth. A* 506.25 (2003).

[159] Martin Anklin, Wolfgang Drahm, and Alfred Rieder. "Coriolis mass flowmeters: Overview of the current state of the art and latest research". In: *Flow Measurement and Instrumentation* 17.6 (2006), pp. 317–323.

[160] Rei Kitamura, Laurent Pilon, and Miroslaw Jonasz. "Optical constants of silica glass from extreme ultraviolet to far infrared at near room temperature". In: *Applied optics* 46.33 (2007), pp. 8118–8133.

[161] Robert Thomas. *Practical guide to ICP-MS: a tutorial for beginners*. CRC press, 2008.

[162] Khushbu Sharma, Renuka Nafdey, and SV Moharil. "Luminescence studies of thermally induced transformations in gadolinium sulfate". In: *Optik* 264 (2022), p. 169401.